Differences of Ca^{2+} Handling Properties and Differential Processing of Olfactory Information in Identified Central Olfactory Neurons

I n a u g u r a l – D i s s e r t a t i o n

zur Erlangung des Doktorgrades

der Mathematisch-Naturwissenschaftlichen Fakultät

der Universität zu Köln

vorgelegt von

Andreas Pippow

aus Essen

Köln 2008

Berichterstatter:	Prof. Dr. P. Kloppenburg
	Prof. Dr. A. Baumann
Tag der mündlichen Prüfung:	14. Juli 2008

Contents

Abbreviations **6**

Zusammenfassung **7**

Abstract **9**

1 Introduction **11**

1.1 Determining parameters that control calcium dynamics with the added buffer approach 13

1.2 Calcium imaging of odor evoked responses 16

2 Materials & Methods **21**

2.1 Animals and materials 21

2.2 Cell culture 22

2.3 Intact brain preparation 23

2.4 Whole cell recordings 24

2.5 Fluorimetric calcium measurements 25

2.5.1 Imaging setup 25

2.5.2 Imaging with fura-2 26

2.5.3 Imaging with OGB-1 30

2.6 Single compartment model of calcium buffering 31

2.6.1 Calcium influx 32

2.6.2 Buffering 32

2.6.3 Extrusion 33

2.6.4 Dynamics of calcium transients 33

2.7 Analysis of calcium buffering 34

2.7.1 Fitting the loading curve 35

2.7.2 Fitting the transients....36
2.7.3 Fitting the linearized Model....37
2.8 Analysis of odor evoked calcium signals....37
2.9 Odor stimulation....38
2.10 Histology....39
2.10.1 Single cell labelling....39
2.10.2 Confocal microscopy....40
2.11 Tools for data analysis....40

3 Results....41

3.1 Identification of neuron types....41
3.1.1 Identification of neurons for the analysis of Ca^{2+} buffering....43
3.1.2 Identification of neurons for the analysis of odor evoked Ca^{2+} signals 44
3.2 Calcium buffering....47
3.2.1 Calcium influx and calcium resting level....47
3.2.2 Dye concentration from loading curves....51
3.2.3 Buffering....53
3.2.4 Comparison of neuron types....58
3.2.5 Outlook – differential buffering in small neuronal compartments of single cells....61
3.3 Imaging of odor evoked calcium signals....63
3.3.1 LNs with glomerulus specific odor responses....65
3.3.2 LNs with uniform glomerular odor responses....72
3.3.3 Uniglomerular projection neurons....74

4 Discussion....77

4.1 Identification of neuron types 77
4.2 Calcium Buffering....78

4.2.1 Individual parameters....82
4.2.2 Methodical Implications....84
4.2.3 Calcium buffering in small neuronal compartments....86
4.3 Imaging of odor evoked calcium signals....87
4.3.1 Implications for olfactory coding....87
4.3.2 Significance of calcium buffering....90
4.3.3 Measuring calcium activity with CCD cameras....91
4.3.4 Outlook and experimental plan....92

List of Figures....93

References....95

Danksagung....105

Erklärung....107

Teilpuplikationen....108

Abbreviations

(u)PN(s)	(uniglomerular) projection neuron(s)
[BCa]	concentration of calcium-bound exogenous buffer B
$[B_T]$	total concentration of exogenous buffer B
$[Ca^{2+}]_i$	intracellular calcium ion concentration
$[Ca^{2+}]_{i,\infty}$	steady-state (resting) calcium level
[SCa]	concentration of calcium-bound endogenous buffer S
$[S_T]$	total concentration of endogenous buffer S
4-AP	4-aminopyridine
AL(s)	antennal lobe(s)
AP(s)	action potential(s)
EGTA	ethylene diamine tetraacetic acid
GABA	γ-aminobutyric acid
iACT	inner antenno-cerebral tract
$j_{in,pipette}$	calcium influx from the pipette in molar
$j_{in,stim}$	calcium influx from a stimulus in molar
$K_{d,Fura}$	dissociation constant of fura-2
$K_{d,S}$	dissociation constant of endogenous buffer S
LN(s)	local interneuron(s)
nCa	absolute calcium influx in mol
OBP(s)	olfactory binding protein(s)
ORC(s)	olfactory receptor cell(s)
v	accessible cell volume
γ	calcium extrusion rate
$\Delta[Ca^{2+}]_i$	change of intracellular calcium concentration, $[Ca^{2+}]_i$ - $[Ca^{2+}]_{i,\infty}$
κ_B	calcium binding capacity of exogenous buffer B
κ_S	calcium binding capacity of endogenous buffer S
$\tau_{loading}$	fura-2 loading time constant
$\tau_{transient}$	decay constant of monoexponential transient

Zusammenfassung

Informationsverarbeitung in Neuronen ist von hoch lokalisierten Kalziumsignalen abhängig. Die räumliche und zeitliche Dynamik solcher Signale wird von mehreren zellulären Parametern bestimmt, u.a. vom Kalzium-Einstrom, der Kalzium-Pufferung und der Pumprate von Kalzium aus der Zelle. Das langfristige Ziel dieser Arbeit gilt dem besseren Verständnis darüber, wie intrazelluläre Kalzium-Dynamiken kontrolliert werden und zur Informationsverarbeitung in Interneuronen des olfaktorischen Systems von Insekten, welches als hervorragendes Modellsystem für allgemeine Mechanismen der Olfaktorik dient, beitragen. Ich habe die *patch-clamp* Technik und schnelle optische *imaging* Methoden mit dem *added buffer approach* kombiniert, um die zellulären Parameter zu analysieren, welche die Dynamik intrazellulärer Kalziumsignale bestimmen. Dafür erforderliche Messungen wurden in adulten *Periplaneta americana* in zwei physiologisch unterschiedlichen lokalen Interneurontypen sowie in uniglomerulären Projektionsneuronen durchgeführt. In uniglomerulären Projektionsneuronen wurde durch 50 ms lange Spannungsschritte von -60 bis + 5 mV ein absoluter Kalzium Einstrom (n_{Ca}) von 0.3 fmol generiert. Die endogene Kalzium-Binderate (κ_S) war 418 und die Pumprate (γ) 221 s^{-1}, was in einer Zeitkonstante (τ_{endo}) des endogenen Signals von 1.8 s resultierte. In lokalen Interneuronen waren diese Werte signifikant unterschiedlich. Lokale Interneurone

vom Typ I, die keine Na^+ getragenen Aktionspotentiale generieren, hatten einen n_{Ca} von 0.12 fmol, κ_S von 154 und γ von 141 s^{-1}, was in einem τ_{endo} von 1.1 s resultierte. In lokalen Interneuronen vom Typ II war n_{Ca} bei 0.5 fmol, κ_S bei 672, γ bei 305 s^{-1} und τ_{endo} bei 2.2 s.

Die Daten zeigen, dass die Kalziumdynamik mit zellulären Funktionen der verschiedenen Neuronentypen korreliert. Interessanterweise haben lokale Interneurone vom Typ II, die keine spannungsaktivierten Na^+ Kanäle besitzen und in denen Kalzium das einzige Kation ist, welches zur Membrandepolarisation beiträgt, die höchste endogene Kalzium-Bindekapazität und -Pumprate.

In einem zweiten Teil wurden lokale Aktivitäten in lokalen Interneuronen vom Typ I+II mit physiologischen Duftstimulationen untersucht. Glomeruläre duftspezifische Tuning-Kurven wurden für individuelle Interneurone aufgenommen. Diese zeigten, dass bei bestimmten Düften einige multiglomeruläre Neurone bevorzugt in nur einem Teil der innervierten Glomeruli aktiv sind, während andere lokale Interneurone unspezifisch in allen innervierten Glomeruli und bei allen Düften aktiv werden. Diese Daten legen nahe, dass einzelne Neurone durch ihre intrinsischen Eigenschaften entweder Netzwerke mit glomerulus-spezifischen oder mit unspezifischen, gleichförmigen Duftantworten bilden können.

Abstract

Information processing in neurons is dependent of highly localized calcium signals. The spatial and temporal dynamics of these signals are determined by a variety of cellular parameters including calcium influx, calcium buffering and calcium extrusion. A long-term goal is to better understand how intracellular calcium dynamics are controlled and contribute to information processing in interneurons of the insect olfactory system, an excellent model to study general mechanisms of olfaction. We used patch-clamp recordings and fast optical imaging in combination with the 'added buffer approach' to analyze cellular parameters that determine the dynamics of internal calcium signaling. Recordings were performed in adult *Periplaneta americana* from 2 types of physiologically different local interneurons and from uniglomerular projection neurons. In uniglomerular projection neurons 50 ms voltage steps from -60 to +5 mV generated an absolute Ca^{2+} influx (n_{Ca}) of 0.3 fmol. The endogenous Ca^{2+} binding ratio (κ_S) was 418, with an extrusion rate (γ) of 221 s^{-1} resulting in a decay constant of the endogenous signal (τ_{endo}) of 1.8 s. In local interneurons these values were significantly different. In type I local interneurons, which generate Na^+ driven action potentials, the absolute Ca^{2+} influx upon a voltage steps from -60 to +5 mV (50 ms) was 0.12 fmol. The endogenous Ca^{2+} binding ratio was 154, the extrusion rate 141 s^{-1}, resulting in a decay constant of 1.1 s. In type II local interneurons the

absolute Ca^{2+} influx was 0.5 fmol, the Ca^{2+} binding ratio was 672, the rate of Ca^{2+} removal was 305 s^{-1} and the endogenous signal decayed with a time constant of 2.2 s.

These data show a clear correlation between Ca^{2+} handling properties and cellular function in different neuron types. Interestingly, type II local interneurons, which do not express voltage activated sodium channels and where Ca^{2+} is the only cation that enters the cell to contribute to membrane depolarization, has the highest endogenous Ca^{2+} binding ratio and Ca^{2+} extrusion rate.

In a second part physiological odor stimulations were applied to reveal general principles of olfactory information processing in type I and type II local interneurons. Odor specific glomerular tuning curves were obtained from individual interneurons demonstrating that some multiglomerular neurons are preferentially active in a subset of the glomeruli for certain odors. Other local interneurons unspecifically react to odors. The results suggest that glomerulus specific and unspecific networks are formed by the intrinsic properties of individual LNs.

1 Introduction

The insect olfactory system serves as an extremely successful model for olfactory information processing (reviewed by Davis, 2004; Fiala, 2007; Hildebrand and Shepherd, 1997; Laurent, 1999; Strausfeld and Hildebrand, 1999; Wilson and Mainen, 2006). Due to the many striking similarities in structural organization and physiological function between vertebrate and invertebrate olfactory systems, data from the insect olfactory system have contributed significantly to the construction of a reasonable general model for olfactory systems on the network level (Davis, 2004; Distler and Boeckh, 1997b; Laurent and Davidowitz, 1994; Wilson and Laurent, 2005). This study is intended to further analyze the cellular parameters that determine intracellular calcium dynamics in central olfactory interneurons to better understand the mechanisms that are mediating olfactory information processing on the cellular and sub-cellular level.

In neurons, calcium regulates a multitude of cellular functions and many aspects of information processing are dependent on highly localized calcium domains. Besides being a charge carrier, which contributes directly to the membrane potential, calcium serves as a second messenger that controls a variety of cellular processes including synaptic release, membrane excitability, enzyme activation and activity dependent gene activation. Selective activation of these functions is achieved through the spatial and temporal distribution of calcium signals (Augustine et al., 2003). The spatial-temporal Ca^{2+} dynamics are determined by

several cellular parameters including calcium influx, geometry of the cell, location of the calcium source, calcium buffering, calcium extrusion, and locally changing diffusion coefficients. Voltage activated Ca^{2+} currents, an important Ca^{2+} entry pathway, have been studied in many insect neuron types (Benquet et al., 1999; Grolleau and Lapied, 1996; Heidel and Pfluger, 2006; Husch et al., 2008; Mills and Pitman, 1997; Wicher and Penzlin, 1997). Other factors that influence calcium dynamics, however, are not as well studied and understood.

Here we used patch-clamp recordings and fast optical imaging in combination with the 'added buffer approach' (Neher and Augustine, 1992) to characterize the calcium buffering and calcium extrusion in interneurons of the first synaptic relay (antennal lobe, AL) in the *Periplaneta americana* olfactory system. The voltage activated Ca^{2+} currents have been described in these neurons previously (Husch et al., 2008).

A long term goal is to better understand how intracellular calcium dynamics contribute to information processing in olfactory interneurons of the insect AL. Specifically, we are interested how far the different electrophysiological characteristics are correlated with differences in Ca^{2+} handling properties. This is of special interest in the AL, because we have recently identified 2 types of LNs with fundamental differences in intrinsic firing properties: type I LNs generate 'normal' Na^{+} driven action potentials, whereas type II LNs do not express voltage activated sodium channels. In type II LNs Ca^{2+} is the only cation that enters the cell to contribute to membrane depolarization. I consider the characterization of cellular parameters that determine cytosolic Ca^{2+} dynamics as an important step towards a detailed understanding of the cellular basis of olfactory information processing on the single cell level.

Besides being essential to better understand the mechanisms of neuronal Ca^{2+} handling and its role in information processing, these data are also important to

help interpret time constants of Ca^{2+} signals from experiments in which Ca^{2+} measurements are performed to monitor global neuronal activity.

This was done in a second part of this thesis, where Ca^{2+} imaging was used to determine odor evoked activity on the subcellular level in the same identified neuron types. Odor stimulations were applied to reveal general principles of olfactory information processing. These data complement the results on Ca^{2+} handling properties and help to better understand the interactions of interneurons in the AL of insects. Subsequently, the two parts of this thesis are introduced in more detail.

1.1 Determining parameters that control calcium dynamics with the added buffer approach

Calcium buffers are important for the control of intracellular Ca^{2+} dynamics. Some calcium-buffering proteins that have been described in detail are calbindin-D28K (Hackney et al., 2005; Jackson and Redman 2003), calretinin (Edmonds et al., 2000; Hackney et al., 2005) and parvalbumin (Muller et al, 2007; Lee et al., 2000; Collin et al., 2005). In this study the 'added buffer approach' was used to determine endogenous buffering proteins, which were however not precisely defined. This study therefore does not go into detail about their nature and regards them as abstract general proteins.

The dynamics of an intracellular calcium signal are mainly determined by the Ca^{2+} source (influx or release from intracellular stores), the intracellular Ca^{2+} buffering and the Ca^{2+} extrusion from the cell. The signal itself is characterized by its resting level, the rise, the amplitude and the decay time constant. These characteristics of the signal are changed when one of the three parameters that shape the signal is altered. A double Ca^{2+} influx (compared to a putative control) would double the

amplitude of the signal. Increasing the calcium binding ratio by a factor of 2 would reduce the amplitude by 50% and double the decay time constant. Reducing the extrusion rate by 50% would double the decay time constant (see Fig. 1). In this study these parameters of intracellular calcium dynamics were quantified in somata of a) isolated olfactory interneurons from the antennal lobe of *Periplaneta americana* (in vitro) and b) on somata of identified uniglomerular projection neurons and two types of local interneurons in an intact brain preparation (in situ) from adult male *P. americana*.

Experimentally, these values could be investigated by patch-clamp recordings combined with simultaneous optical imaging techniques. Electrophysiological data were used to measure absolute voltage induced Ca^{2+} movements across the cell membrane. Imaging combined with patch-clamp techniques were used to reveal the following characteristics of the intracellular calcium signal: Ca^{2+} influx, endogenous Ca^{2+} binding ratio and Ca^{2+} extrusion. However, the indicator represented an exogenous (added) buffer, which competed with the endogenous buffers, increasing the actual calcium binding ratio while it diffused into the cell. Thereby it reduced the amplitude and increased the decay time constant, as obvious in Fig. 1C. The resting level was supposably not affected.

To reveal the values of the endogenous calcium binding ratio (and therefore the amplitude and decay constant of the intracellular signal), the 'added buffer approach' was applied (Neher and Augustine, 1992). This method uses a single compartment model with the following assumptions: a big patch-pipette is connected to a tiny cell, the endogenous buffer is immobile, the exogenous buffer diffuses exponentially into the cell and is always in a “well mixed state”, Ca^{2+} goes into the cell via voltage activated Ca^{2+} channels, leak currents and the patch-pipette, Ca^{2+} clearance is linear and non-saturable, the exogenous and endogenous buffers are always at equilibrium with Ca^{2+} (Helmchen et al., 1997; Neher and

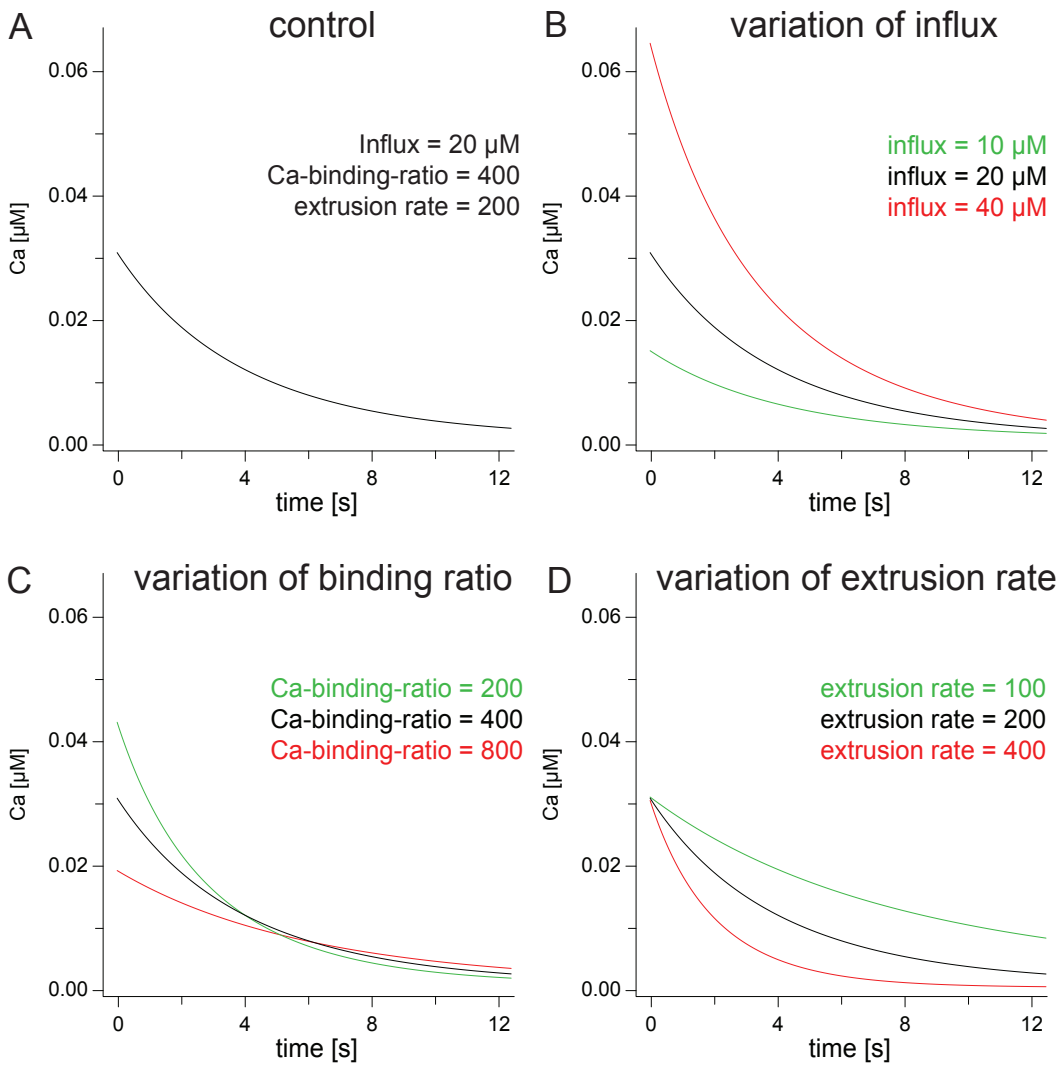

Figure 1: Single compartment model of calcium buffering
*(**A**) Computer simulations of the decay of Ca^{2+} in a single compartment model. Transients were numerically computed by integration of the differential equation (Eq. 12) describing the Ca^{2+} dynamics in a homogeneous compartment. Initial values for the simulations were chosen to be in the range of values determined throughout this study, roughly simulating the decay kinetics of a projection neuron (total dye concentration [BT] = 100 µM, total dye concentration in the pipette [BCa_p] = 200 µM, loading time constant of the dye τloading = 1000 s, Ca^{2+}-binding-ratio of the endogenous buffer $\kappa_S \approx [ST] \cdot (K_{d,S})^{-1} = 400$, dissociation constant of the dye $K_{d,Fura} = 0.191$ µM, Ca^{2+}-extrusion-rate $\gamma = 200\ s^{-1}$, resting Ca^{2+} concentration $[Ca^{2+}]_{i,\infty} = 0$ µM, Ca^{2+} influx (see eq. 8) = 20 µM). (**B**) Computer simulations as in (A), with the same initial values (black), half the Ca^{2+} influx (green) and double the Ca^{2+} influx (red). (**C**) Simulations as in (A), with the same initial values (black), half the Ca^{2+}-binding-ratio (green) and double the Ca^{2+}-binding-ratio (red). (**D**) Simulations as in (A), with the same initial values (black), half the Ca^{2+}-extrusion rate (green) and double the Ca^{2+}-extrusion rate (red).*

Augustine, 1992). In other words: 1) Changes in the indicator concentration have a linear effect on the amplitude and the decay constant. 2) When the actual calcium

binding ratio is plotted over the decay constant of the signal, the data can be fitted by a linear function.

By measuring voltage evoked Ca^{2+} fluxes in combination with intracellular Ca^{2+} kinetics, it was possible to determine the decay constants for different, defined dye concentrations. Having determined these dye concentrations, the actual calcium binding ratio (which is computed by the sum of endogenous and exogenous buffers) could be computed. Setting the actual calcium binding ratio for every data point in dependence of the decay constant, the endogenous calcium binding ratio, the amplitude and the decay constant with no exogenous buffer and the extrusion rate could be extrapolated. The total Ca^{2+} influx was measured with patch-clamp recordings and the mean resting Ca^{2+} level was collected from Ca^{2+} kinetic measurements. Thus, all attributes of an intracellular Ca^{2+} signal had been determined.

1.2 Calcium imaging of odor evoked responses

Odor discrimination is crucial for the survival of most animals. One experimental system that has very successfully served as a model to understand olfactory information processing is the first synaptic relay (antennal lobe) of the olfactory system of insects (Davis, 2004; Distler and Boeckh, 1998; Fiala, 2007; Hildebrand and Shepherd, 1997; Laurent, 1999; Sakura et al., 2002; Strausfeld and Hildebrand, 1999; Watanabe et al., 2003 ; Wilson and Mainen, 2006).

Olfaction begins with transduction of chemical information into electrical signals in the olfactory receptor cells (ORCs). Specialized olfactory binding proteins (OBPs) transport odor molecules through the antennal lymph to receptors in the membrane of the ORCs. The receptors belong to the G-Protein coupled receptor family each of which expresses one receptor type of a multigene family. Upon

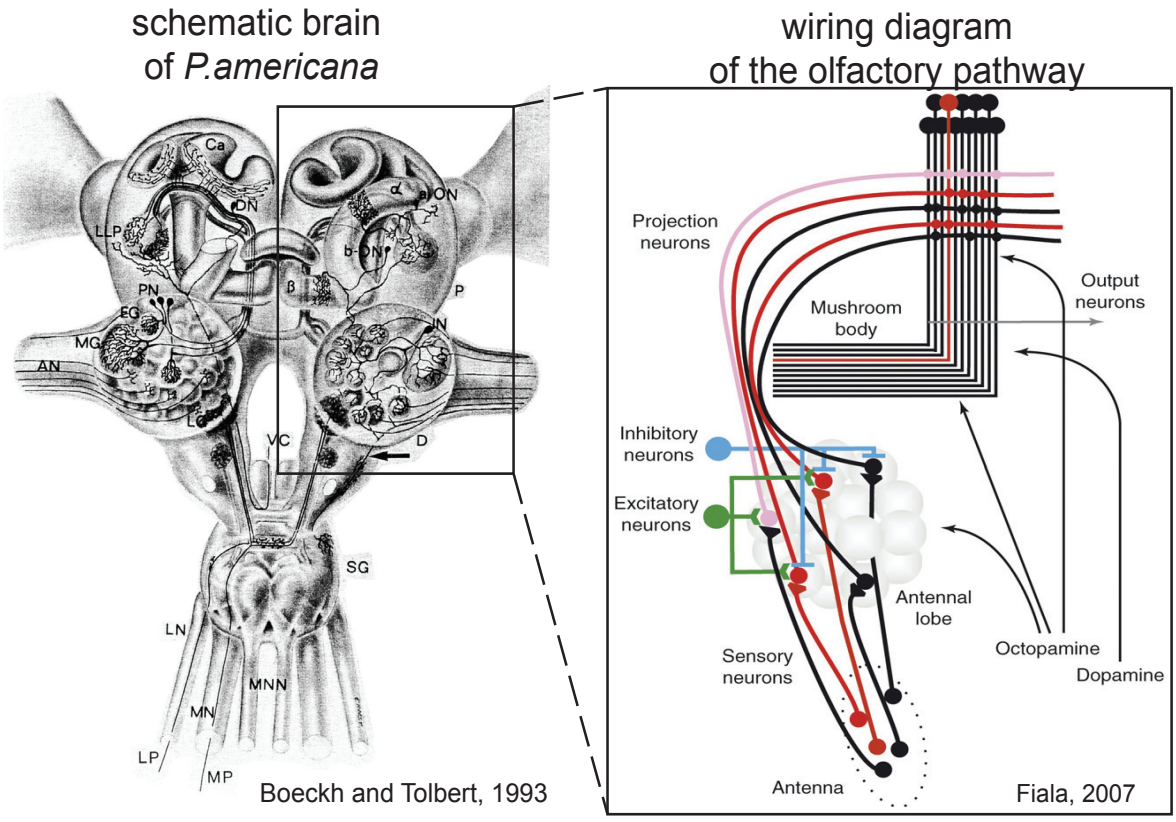

Figure 2: Olfactory pathways in the insect olfactory system
*(**left side**) Chemosensory pathways in the brain and the suboesophageal ganglion of Periplaneta americana taken from (Boeckh and Tolbert, 1993). AN: antennal nerve, D: deutocerebrum, DN: descending neuron, EG: glomerulus with cineole-sensitive projection neuron, IN: local interneuron LG: lobus glorneratus, LLP: lobus lateralis protocerebralis, LN: labial nerve, MG: macroglomerulus, MN: maxillary nerve; MNN: mandibular nerve, P: protocerebrum, SG: suboesophageal ganglion, T: tritocerebrum, VC: ventral nerve cord, α: α-lobe of corpus pedunculatum, β: β-lobe of corpus pedunculaturn. (**right side**) Schematic wiring diagram of the olfactory pathway (using the example of Drosophila). Odors are perceived by sensory neurons on the antenna, which project to invariant glomeruli in the antennal lobe. Activated neurons are depicted in red. The antennal lobe network includes local inhibitory and excitatory neurons, which transform olfactroy information so that PNs respond to a broader range of odorants compared to sensory neurons (i.e. the pink PN). Taken from (Fiala, 2007).*

binding of the ligand the receptor then transduces the chemical into an electrical signal. The electrical information is projected along the axons of the ORCs into glomeruli in the antennal lobe (AL), areas of high density of synaptic connections. ORCs expressing the same receptor gene precisely project to the same glomerulus (Buck and Axel, 1991; Gao et al., 2000; Ressler et al., 1994; Wang et al., 2003). The glomeruli are the first synaptic relay in the olfactory pathway and serve as the

primary olfactory information processing center (Reviewed in (Hildebrand and Shepherd, 1997)). In *Periplaneta americana*, there are 100,000 olfactory receptor cells (Boeckh, 1974) whose axons innervate the antennal lobe. This information is processed by about 500 local interneurons (LNs) in the 125 olfactory glomeruli (Boeckh and Ernst, 1987). Arborizations of the local interneurons are confined to the antennal lobe, interconnecting glomeruli (Christensen et al., 1993). The sensory information is then relayed to higher order brain centers by about 150 projection neurons (PNs) projecting through the inner antenno-cerebral-tract (iACT) (Boeckh and Ernst, 1987). Most of these projection neurons have arborizations in individual glomeruli of the antennal lobe and send axons to the mushroom body and the lateral lobe of the protocerebrum (Malun et al., 1993). Fig. 2 illustrates these chemosensory pathways in general and the wiring of the main neuron types in detail.

How is olfactory information processed in the antennal lobe? Several authors propose that a certain odor evokes a topographic map in the antennal lobe and in higher brain centers, meaning that the recognition of an odor was coded in spatial patterns (Galizia et al., 1999; Wong et al., 2002; Wang et al., 2003). According to this view a certain odor elicits activity in specific ORCs, each of which converges to one specific glomerulus. A topographic map of receptor activity in the periphery is therefore represented in the antennal lobe (Wang et al., 2003) and is passed on to higher brain centers (*labeled-line*) (Wong et al., 2002), with little interactions between glomeruli (Ng et al., 2002; Root et al., 2007).

Recent physiological studies show that the LNs significantly contribute to information processing by forming a complex network of inhibitory (Distler et al., 1998; Wilson and Laurent, 2005; Silbering and Galizia, 2007) and excitatory (Olsen et al., 2007; Shang et al., 2007; Wilson et al., 2004) interactions on the glomerular level. More and more authors suggest that intereactions between glomeruli are

essential in olfactory processing. Recent studies in honey bees and fruit flies propose two independent inhibitory networks: one is PTX-sensitive (and therefore GABAergic) and modulates overall AL activity, the other is PTX-insensitive and glomerulus-specific (Sachse and Galizia, 2002; Silbering and Galizia, 2007). Inhibitory connections of the latter network selectively inhibit glomeruli with overlapping response profiles. These selectively inhibited glomeruli don't have to be spatial neighbors. The net result is a globally modulated, contrast enhanced and predictable representation of odors in the olfactory output neurons (Sachse and Galizia, 2002; Silbering and Galizia, 2007). Other authors propose that LNs form more heterogeneous interactions by releasing various peptides, biogenic amines or acetylcholine and can also be excitatory (Wilson et al., 2004; Shang et al., 2007; Olsen et al., 2007). Excitatory interneurons have been found to broaden the response spectra of individual PNs. According to this view, the input to PNs does not come from olfactory sensory neurons alone. Excitatory LNs significantly contribute to broaden PN output compared to the direct sensory input. A complex network of lateral interactions redistributes oder-evoked activity over a larger ensemble of PNs to broaden their tuning range (Wilson et al., 2004; Bhandawat et al., 2007).

Silbering and Galizia (2007) propose an interaction of excitatory and inhibitory networks, parts of which must be glomerulus specific (Silbering and Galizia, 2007) (for illustration see also Fig. 2). This means, that there have to be LNs capable of preferentially interconnecting a subset of the glomeruli.

While the important role of the LNs for modulating PN output becomes more and more apparent, still little is known about odor evoked activities in LNs on the glomerular level. However, this could resolve some of the questions about the character of glomerular interactions. Therefore, this study looked at odor evoked activity in individual glomeruli of previously identified LNs of the antennal lobe

of *Periplaneta americana*. Calcium imaging in combination with patch-clamp recordings and physiological odor stimulation were used to monitor glomerular activity in single LNs.

2 Materials & Methods

2.1 Animals and materials

P. americana were reared in crowded colonies at 27°C under a 13:11 h light/dark photoperiod regimen and reared on a diet of dry dog food, oatmeal and water. The in vitro experiments were performed on adult animals of both sexes, the in situ recordings were performed with adult males. Before dissection the animals were anesthetized by CO_2 or cooling (4 °C) for several minutes. For cell culture they where then adhered in a plastic tube with adhesive tape and the heads were immobilized using dental modelling wax (S-U Modellierwachs, Schuler-Dental, Ulm, Germany) with a low solidification point (57 °C). For in situ experiments the animals were placed in a custom built holder, and the head was immobilised with dental wax. The antennae were placed in small tubes on a plastic ring that was later used to transfer the preparation to the recording chamber.

All chemicals, unless stated otherwise, were obtained from Aplichem (Darmstadt, Germany) or Sigma-Aldrich (Taufkirchen, Germany) with a purity grade of 'per analysis'.

2.2 Cell culture

To examine the electrophysiological properties of isolated antennal lobe neurons, cells were dissociated and cultured using modified protocols reported previously (Grolleau and Lapied, 1996; Hayashi and Hildebrand, 1990; Kirchhof and Mercer, 1997). The head capsule of anesthetized animals was opened and the antennal lobes were dissected with fine forceps. Typically, ALs from eight animals were pooled in sterile 'culture' saline (kept on ice) containing (in mM): 185 NaCl, 4 KCl, 6 $CaCl_2$, 2 $MgCl_2$, 35 D-glucose, 10 HEPES and 5% fetal bovine serum (S-10, c.c.pro, Neustadt, Germany), adjusted to pH 7.2 (with NaOH), which resulted in an osmolarity of ~420 mOsm. For dissociation the ALs were transferred for 2 min at 37 °C into 500 µl Hanks Ca^{2+}- and Mg^{2+}-free buffered salt solution (14170, GIBCO, Invitrogen, Karlsruhe, Germany) containing (in mM): 10 HEPES, 130 sucrose, 8 units ml^{-1} collagenase (LS004194, Worthington, Lakewood, New Jersey, USA) and 0.7 units ml^{-1} dispase (LS02100, Worthington), adjusted to pH 7.2 (with NaOH) and to 450 mOsm (with sucrose). Dissociation of neurons was aided by careful titruation with a fire-polished Pasteur pipette for 3 - 5 min. Enzyme treatment was terminated by cooling and centrifuging the cells twice through 6 ml of culture medium (4 °C, 480 g, 5 min). The culture medium consisted of five parts Schneider's *Drosophila* medium (21720, GIBCO) and four parts Minimum Essential Medium (21575, GIBCO) to which was added (in mM): 10 HEPES, 15 glucose, 10 fructose, 60 sucrose, 5% fetal bovine serum adjusted to pH 7.5 (with NaOH) and 430 mOsm (with sucrose). After centrifugation, the cells were resuspended in a small volume of culture medium (100 µl per dish, eight ALs were plated in five to six dishes), and allowed to settle for 2 h to adhere to the surface of the culture dishes coated with concanavalin A (C-2010, Sigma, 0.7 mg ml^{-1} dissolved in H_2O). The cultures were placed in an incubator at 26°C, and then used for

electrophysiological experiments on the same day. For recordings the cells were visualized with an inverted microscope (IX71, Olympus, Hamburg, Germany) using a 40x water objective (UAPO 40x, 1.15 NA, 0.25 mm WD, Olympus) and phase contrast optics.

2.3 Intact brain preparation

The intact brain preparation was based on an approach described previously (Kloppenburg et al., 1999a; Kloppenburg et al., 1999b), in which the entire olfactory network was left intact. The animals were anesthetized by CO_2, placed in a custom build holder and the head with antennae was immobilized with tape (tesa ExtraPower Gewebeband, Tesa , Hamburg, Germany). The head capsule was opened by cutting a window between the two compound eyes and the bases of the antennae. The brain with antennal nerves and antennae attached was dissected from the head capsule in 'normal saline' (see following text) and pinned in a Sylgard-coated (Dow Corning Corp., Midland, Michigan, USA) recording chamber. To gain access to the recording site and facilitate the penetration of pharmacological agents into the tissue, we desheated parts of the AL using fine forceps. Some preparations were also enzyme treated with a mixture of papain (0.3 mg ml^{-1}, P4762, Sigma) and L-cysteine (1 mg ml^{-1}, 30090, Fluka/Sigma,) dissolved in ‘normal' saline (~ 3 min, RT). The AL neurons were visualized with a fixed stage upright microscope (BX51WI, Olympus, Hamburg, Germany) using a 20x water-immersion objective (XLUMPLFL 20x / 0.95 NA / 2 mm WD, Olympus) with a 4x magnification changer (U-TVAC, Olympus) and IR-DIC optics (Dodt and Zieglgansberger, 1994).

2.4 Whole cell recordings

Whole-cell recordings were performed at 24 °C following the methods described by (Hamill et al., 1981). Electrodes with tip resistance between 3-5 MΩ were fashioned from borosilicate glass (0.86 mm ID, 1.5 mm OD, GB150-8P, Science Products, Hofheim, Germany) with a temperature controlled pipette puller (PIP5, HEKA-Elektronik, Lambrecht, Germany). For current clamp recordings and imaging the pipettes were filled with 'normal intracellular saline' containing (in mM): 220 K-aspartate, 10 NaCl, 2 $MgCl_2$, 10 HEPES and 600 µM OGB-1 (O6806, Molecular Probes, Oregon, USA) adjusted to pH 7.2 (with KOH), resulting in an osmolarity of ~ 415 mOsm. For voltage clamp recordings of Ca^{2+} currents the pipettes were filled with 'intracellular calcium saline' containing (in mM): 210 CsCl, 10 NaCl, 2 $MgCl_2$, 10 Hepes and 200 µM fura-2 (F1200, Molecular Probes) adjusted to pH 7.2 (with CsOH), resulting in an osmolarity of ~420 mOsm. During the experiments, if not stated otherwise, the cells were superfused constantly with 'normal' saline solution containing (in mM): 185 NaCl, 4 KCl, 6 $CaCl_2$, 2 $MgCl_2$, 10 HEPES, 35 D-glucose. The solution was adjusted to pH 7.2 (with NaOH) and to 430 mOsm (with glucose).

To isolate the Ca^{2+} currents a combination of pharmacological blockers and ion substitution was used that has been shown to be effective in central olfactory neurons of the cockroach (Husch et al., 2008) and in other insect preparations (Kloppenburg et al., 1999b; Kloppenburg and Hörner, 1998; Schafer et al., 1994). Transient voltage-gated sodium currents were blocked by tetrodotoxin (TTX, 10^{-7} M, T-550, Alomone, Jerusalem, Israel). 4-aminopyridine (4×10^{-3} M, 4-AP, A78403, Sigma) was used to block transient K^+ currents (I_A) and tetraethylammonium (20×10^{-3} M, TEA, T2265, Sigma-Aldrich) blocked sustained K^+ currents ($I_{K(V)}$) as well as

Ca^{2+} activated K^+ currents ($I_{K(Ca)}$). To further reduce outward currents the pipette solution contained cesium instead of potassium.

Whole-cell voltage- and current-clamp recordings were made with an EPC9 patch-clamp amplifier (HEKA-Elektronik) that was controlled by the program Pulse (version 8.63, HEKA-Elektronik) running under Windows. The electrophysiological data were sampled at intervals of 100 μs (10 kHz). The recordings were low pass filtered at 2 kHz with a 4-pole Bessel-Filter. Compensation of the offset potential and capacitive currents was performed using the 'automatic mode' of the EPC9 amplifier. Whole cell capacitance was determined by using the capacitance compensation (C-sow) of the EPC9. The calculated liquid junction potential between intracellular and extracellular solution (see Neher, 1992) of 17 mV for 'normal intracellular saline' and of 4.8 mV for 'intracellular calcium saline' (calculated with Patcher's-Power-Tools plug-in from http://www.mpibpc.gwdg.de/abteilungen/140/software/index.html for Igor Pro (Wavemetrics, Portland, Oregon, USA)) was also compensated. To remove uncompensated leakage and capacitive currents, a p/6 protocol was used (see Armstrong and Bezanilla, 1974). Voltage errors due to series resistance (R_S) were minimized using the RS-compensation of the EPC9. R_S was compensated between 30% and 70% with a time constant (t) of 2 μs. Stimulus protocols used for each set of experiments are provided in the results.

2.5 Fluorimetric calcium measurements

2.5.1 Imaging setup

The imaging setup for fluorimetric measurements consisted of an Imago/SensiCam CCD camera with a 640x480 chip (Till Photonics, Planegg,

Germany) and a Polychromator IV (Till Photonics) that was coupled via an optical fibre into an IX71 inverted microscope or a fixed stage BX51 WI upright microscope (both from Olympus, for details see above). The camera and the polychromator were controlled by the software Vision (version 4.0, Till Photonics) run on a Windows PC.

2.5.2 Imaging with fura-2

For the analysis of Ca^{2+} dynamics (fist part of this study, see chapter 3.2) intracellular Ca^{2+} concentrations were measured using the Ca^{2+} indicator fura-2 which is suitable for calibrated, ratiometric measurements to determine absolute Ca^{2+} concentrations (Grynkiewicz et al., 1985; Poenie, 1990). The neurons were loaded with fura-2 via the patch pipette (200 µM in the pipette) and illuminated during data collection with 340nm, 360nm or 380nm light from the polychromator that was reflected onto cells with a 410 nm dichroic mirror (DCLP410, Chroma, Gräfeling, Germany). Emitted fluorescence was detected through a 440 nm long-pass filter (LP440). Data were acquired as 40x30 frames using 8x8 on-chip binning for fast kinetic measurements and 80x60 frames using 4x4 binning for slow loading measurements. Images were recorded in analog-to-digital units (adu) and stored and analyzed as 12 bit grayscale images. For all calculations of kinetics, the mean value of adu within regions of interest (ROI) from the center of the cell bodies were used.

Calibration

Absolute Ca^{2+} concentrations were determined from the raw fluorescence data according to the approach from (Grynkiewicz et al., 1985), where the intracellular Ca^{2+} concentration is described as:

$$[Ca^{2+}]_i = K_{d,Fura} \cdot \left(\frac{F380_{min}}{F380_{max}}\right) \cdot \frac{(R - R_{min})}{(R_{max} - R)} \quad (1)$$

$[Ca^{2+}]_i$ is the intracellular Ca^{2+} concentration for the fluorescence ratio R measured at 340 nm and 380 nm excitation. R_{min} is the ratio at a Ca^{2+} concentration of virtually

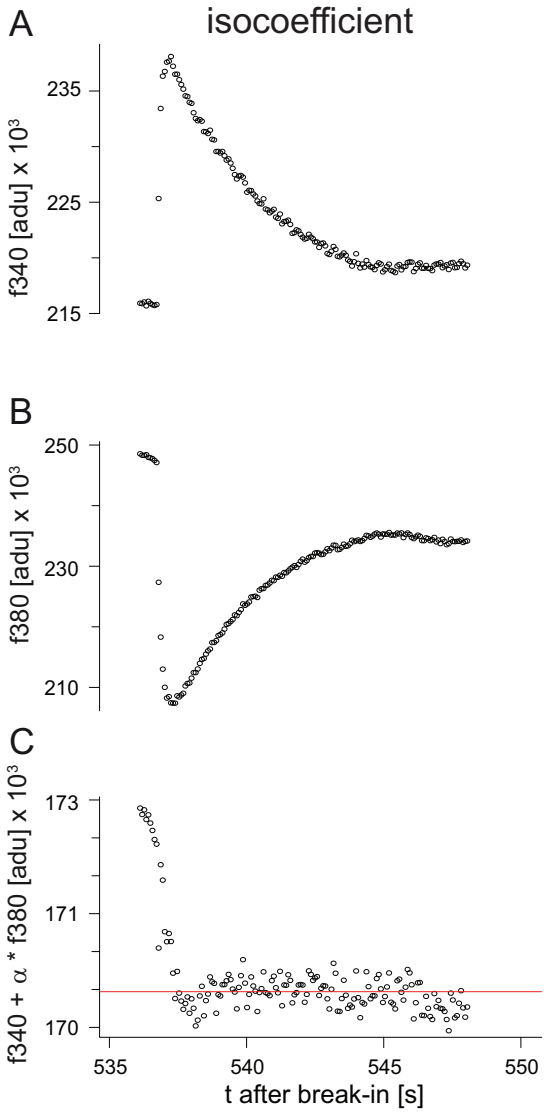

Figure 3: Determination of isocoefficient

*To determine the actual dissociation constant of the Ca^{2+} indicator fura-2, the isocoefficient α needs to be known. The isocoefficient is found by eliciting a Ca^{2+} transient, which is monitored at 340 nm excitation (**A**) (fluorescence rises upon Ca^{2+} influx) and 380 nm excitation (**B**) (fluorescence decreases upon Ca^{2+} influx). The isocoefficient is then the factor that makes the sum F_i = F340 + α F380 independent of Ca^{2+} (**C**). In this study I found that F_i becomes independent of Ca^{2+} (horizontal line in (C)) when the transient is analyzed after the peak.*

0 M (i.e. ideally no fura-2 molecules are bound to Ca^{2+}). R_{max} is the value at saturating Ca^{2+} concentrations (i.e. ideally all fura-2 molecules are saturated with Ca^{2+}). $K_{d,Fura}$ is the dissociation constant of fura-2 for the given experimental conditions. $F380_{min}/F380_{max}$ is the ratio between the emitted fluorescence of Ca^{2+} free dye and the emitted fluorescence of Ca^{2+} saturated dye at 380 nm excitation, reflecting the dynamic range of the indicator.

We used two methods for calibration: a) in vivo (in living cells) and b) in vitro (in solution). For in vivo calibration the effective dissociation constant $K_{d,Fura,eff}$ was introduced (Neher, 1989) :

$$[Ca^{2+}]_i = K_{d,Fura,eff} \cdot \frac{(R - R_{min})}{(R_{max} - R)} \tag{2}$$

and accordingly:

$$K_{d,Fura,eff} = [Ca^{2+}]_i \cdot \frac{(R_{max} - R)}{(R - R_{min})} \tag{3}$$

For in vitro calibration a correction factor (R_d) for R_{max} and R_{min} has been suggested to account for environmental differences between the cytoplasmic milieu and in vitro conditions (Poenie, 1990):

$$K_{d,Fura,eff} = [Ca^{2+}]_i \cdot \frac{(R_{max} \cdot R_d - R)}{(R - R_{min} \cdot R_d)} \tag{4}$$

R_d was determined as described in (Poenie, 1990)

To determine the endogeneous Ca^{2+} binding ratio the actual dissociation constant ($K_{d,Fura}$) has to be known. The relationship between the effective dissociation constant ($K_{d,Fura,eff}$) and $K_{d,Fura}$ is given by (Zhou and Neher, 1993):

$$K_{d,Fura} = K_{d,Fura,eff} \frac{(R_{min} + \alpha)}{(R_{max} + \alpha)} \tag{5}$$

α is the isocoefficient, for which the sum

$$F_i(t) = F_{340}(t) + \alpha F_{380}(t) \quad (6)$$

is independent of calcium. F340 and F380 are the fluorescence traces measured during a brief Ca^{2+} excursion. The correct isocoefficient can be chosen as that value of α which minimizes this excursion (Fig. 3). Once the isocoefficient has been determined, the actual $K_{d,Fura}$ can be calculated from equation 5.

Calibration Solutions

The free Ca^{2+} concentrations of the calibration solutions were adjusted by using appropriate proportions of Ca^{2+} and the Ca^{2+} chelator EGTA. The ability of EGTA to bind calcium is highly dependent on parameters such as ionic strength, temperature, pH and the concentrations of other metals that compete for binding (Harrison and Bers, 1987; Harrison and Bers, 1989). To account for these parameters we calculated the appropriate concentrations by using the program MaxChelator (WinMaxc32 version 2.50, http://www.stanford.edu/~cpatton/maxc.html), which is based on work of (Bers et al., 1994; Brooks and Storey, 1992; Patton et al., 2004; Schoenmakers et al., 1992). The necessary amount of Ca^{2+}, Mg^{2+} and EGTA was computed to set the free Ca^{2+} and Mg^{2+} concentration for the experimental conditions (22 °C; pH 7.2; ionic strength [without divalent ions and Ca^{2+} chelator]: 219 mM for R_{min} and R_{max}, 214 mM for R_{def}). Calibration solutions were prepared as follows (in mM): R_{max}: 205 CsCl, 10 NaCl, 2 $MgCl_2$, 10 HEPES, 10 $CaCl_2$ and 0.2 fura-2; R_{min}: 205 CsCl, 10 NaCl, 2.7 $MgCl_2$, 10 HEPES, 10 EGTA and 0.2 fura-2; R_{def}: 200 CsCl, 10 NaCl, 2.4 $MgCl_2$, 4.1 $CaCl_2$, 10 HEPES, 10 EGTA and 0.2 fura-2, yielding a free Ca^{2+} concentration of 140 nm. All solutions were adjusted to pH 7.2 with CsOH resulting in an osmolarity of ~430 mOsm (R_{max}) and ~440 mOsm (R_{min}, R_{def}), respectively.

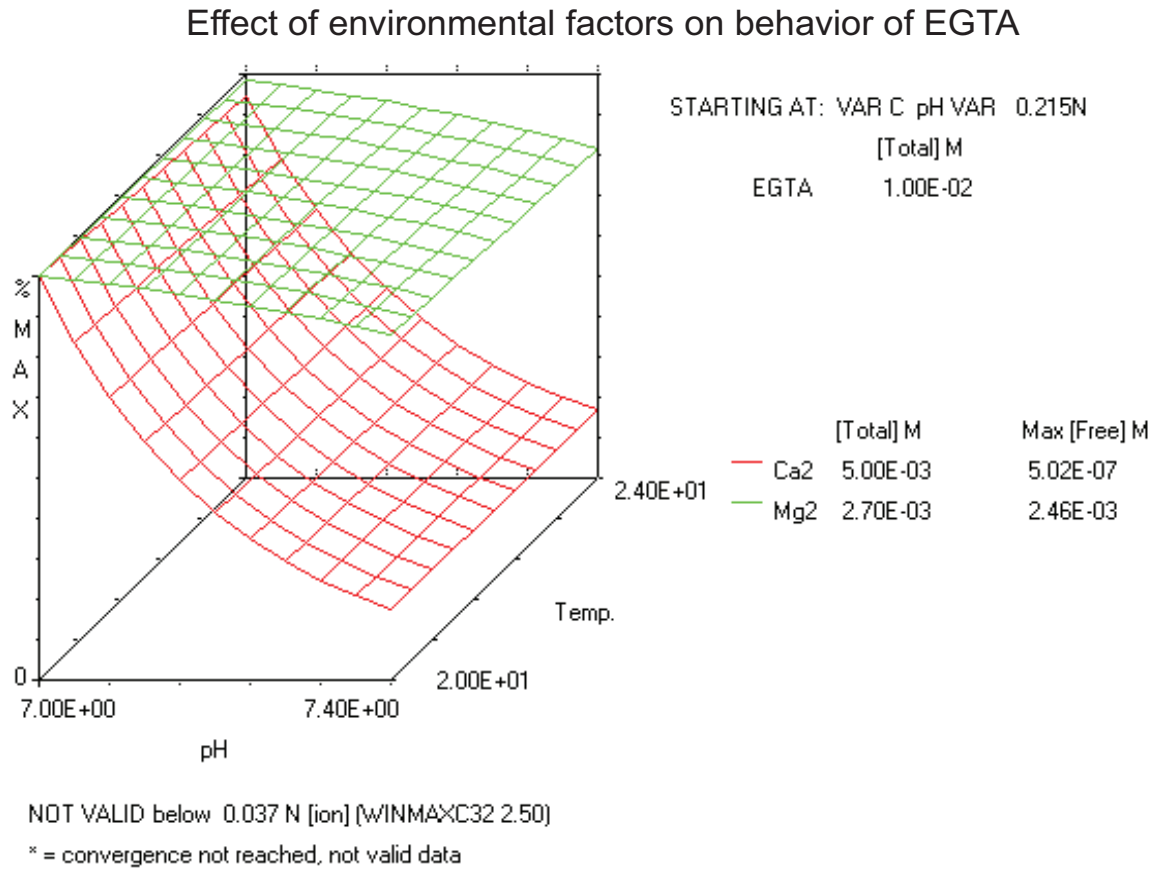

Figure 4: Behavior of EGTA when temperature or pH are changed
The Ca^{2+} chelator EGTA is used to buffer solutions to a given free Ca^{2+} concentration, which then are used to calibrate the Ca^{2+} indicator fura-2. The Ca^{2+} chelator EGTA is strongly dependent of environmental changes like pH, temperature and ionic strenght of the buffered solution. 3D-calculations of free metal concentrations (Mg^{2+} and Ca^{2+}) in dependence of variable temperature and pH, while the amount of EGTA, Ca^{2+}, Mg^{2+} and ionic strength are held constant were done with the MaxChelator program (http://www.stanford.edu/~cpatton/maxc.html). X-axis shows variable pH from 7 to 7.4, z-axis shows variable temperature from 20 °C to 24 °C. Ionic strenght was set to 0.215 N. Added amount of EGTA (10 mM), Ca^{2+} (5 mM) and Mg^{2+} (2.7 mM) have also been set constant. Percent of maximum free metal ion concentration is shown in dependance of variables pH and temperature. Note that small changes in pH lead to dramatic changes in free calcium concentration of the solution. The MaxChelator program has been used to prepare buffered solutions for Ca^{2+} calibration experiments.

2.5.3 Imaging with OGB-1

For the analysis of odor evoked Ca^{2+} signals in glomeruli of individual local interneurons (second part of this thesis, see chapter 3.3) intracellular Ca^{2+} signals were measured using the Ca^{2+} indicator Oregon-Green-Bapta-1 (OGB-1), which is a single wavelength, high affinity indicator suitable to measure Ca^{2+} changes. The

neurons were loaded with OGB-1 via the patch pipette (600 μM in the pipette) and illuminated during data collection with 490nm light from the polychromator that was reflected onto cells with a 505 nm dichroic mirror (Q505lp, Chroma). Emitted fluorescence was detected through a 515-555 nm band-pass filter (HQ 535/40, Chroma). Data were acquired as 160x120 frames using 4x4 on-chip binning with 13.3 – 20 Hz (50 ms exposure time). Images were recorded in analog-to-digital units (adu) and stored and analyzed as 12 bit grayscale images. For all calculations of kinetics, the mean value of adu within regions of interest (ROI) from the center of the cell bodies were used. Kinetics were analyzed off-line using Igor 6.

2.6 Single compartment model of calcium buffering

For measurements of intracellular Ca^{2+} concentrations with Ca^{2+} chelator based indicators the amplitude and time course of the signals are dependent on the concentration of the Ca^{2+} indicator (in this case fura-2) that acts as an exogenous (added) Ca^{2+} buffer and competes with the endogeneous buffer (Helmchen et al., 1997; Helmchen and Tank, 2005; Neher and Augustine, 1992; Tank et al., 1995). The 'added buffer approach' (Neher and Augustine, 1992) uses this principle to analyze the endogenous buffer capacity of a cell by measuring the decay of the Ca^{2+} signal at different concentrations of 'added buffer' and to extrapolate to conditions in which only the endogeneous buffer is present. This approach is based on a single compartment model assuming that a big patch-pipette with a known (clamped) concentration of a Ca^{2+} indicator (fura) is connected (whole-cell configuration) to a spherical cell. The model assumes that the cell contains an immobile endogenous Ca^{2+} buffer (S) whose total concentration, dissociation constant $K_{d,S}$, and its on (k^+) and off (k^-) rates are unknown. When the whole cell configuration is established (break in) fura (in its bound and unbound forms)

starts to diffuse into the cell whereas the cell is considered small enough to be always in a 'well mixed' state (i.e., there are no gradients of chemical species within the cell). In this model 3 cellular parameters determine the cytosolic Ca^{2+} dynamics: 1) influx of Ca^{2+}, 2) Ca^{2+}binding ratio, and 3) Ca^{2+} extrusion.

2.6.1 Calcium influx

In the model two forms of Ca^{2+} influx are assumed, the Ca^{2+} influx from the pipette ($j_{\text{in, pipette}}$) and Ca^{2+} entering the cell via voltage activated channels ($j_{\text{in. Stim}}$) (Helmchen and Tank, 2005; Neher and Augustine, 1992):

$$j_{\text{in, pipette}} = ([\text{BCa}_\text{P}] - [\text{BCa}]) \frac{D_\text{B}\rho}{R_\text{P}} \tag{7}$$

$$j_{\text{in, stim}} = \text{Ca}_\text{inc}\,\delta(t - t_{stim}) = \frac{\text{Q}_\text{Ca}}{2\text{F}\,v}\,\delta(t - t_{stim}) \tag{8}$$

[BCa] is the concentration of the exogenous buffer (fura-2) in its Ca^{2+} bound form (the subscript $_\text{P}$ is for quantities within the pipette), R_P is the pipette resistance, ρ is the specific resistance of the pipette filling solution, D_B is the diffusion coefficient of the exogenous buffer, $\delta(t\text{-}t_{stim})$ is the delta function with t_{stim} as the time of stimulus, Ca_{inc} is the integral Ca^{2+} influx during the short stimulus, Q_{Ca} is the Ca^{2+} charge, F is the Faraday's constant and v the volume of the cell.

2.6.2 Buffering

In the cell Ca^{2+} is bound by the Ca^{2+} buffers fura-2 and the immobile endogenous buffer, which are both nonsaturating and assumed always in equilibrium with free Ca^{2+}. The ability of the experimentally introduced exogenous buffer to bind Ca^{2+} is described by its Ca^{2+}- binding ratio that is defined as the ratio of the change in buffer-bound Ca^{2+} over the change in free Ca^{2+}:

$$\kappa_B = \frac{d[BCa]}{d[Ca^{2+}]} = \frac{[B_T] K_d}{([Ca^{2+}]_i + K_d)^2} \quad (9)$$

$[B_T]$ is the total concentration of the exogenous buffer B and K_d is its dissociation constant for Ca^{2+}. An analogous expression exists for the Ca^{2+}- binding ratio of the endogenous buffer S (κ_S).

2.6.3 Extrusion

The model assumes a linear extrusion mechanism for Ca^{2+} reflecting the combined action of pumps, exchange carriers and membrane conductances:

$$j_{out} = \gamma \Delta[Ca^{2+}]_i = \gamma([Ca^{2+}]_i - [Ca^{2+}]_{i,\infty}) \quad (10)$$

where γ is the clearance rate and $[Ca^{2+}]_{i,\infty}$ is the steady state value for the intracellular Ca^{2+} concentration $[Ca^{2+}]_i$, which is the Ca^{2+} level to which a transient decays.

2.6.4 Dynamics of calcium transients

The mechanisms described in Eq. 7, 8, 9 and 10 are combined to the model that describes the Ca^{2+}- dynamics after a brief Ca^{2+}- influx:

$$\frac{d[Ca^{2+}]_i}{dt} + \frac{d[BCa]}{dt} + \frac{d[SCa]}{dt} = \frac{j_{in,\,pipette} + j_{in,\,stim} - j_{out}}{v} \quad (11)$$

Substituting the time dependent terms for the buffers B and S with their Ca^{2+}-binding capacities, [BCa] with its equilibrium value $[BCa] = [Ca^{2+}]_i [B_T]/(K_d+[Ca^{2+}]_i)$ and $\tau_{loading} = (v \cdot R_P)/(D_B \cdot \rho)$ we get:

$$\frac{d[Ca^{2+}]_i}{dt} = \frac{\tau_{loading}^{-1} \cdot ([BCa_p] - \frac{[Ca^{2+}]_i [B_T]}{K_d + [Ca^{2+}]_i}) + \frac{\gamma}{v} \cdot ([Ca^{2+}]_{i,\infty} - [Ca^{2+}]_i) + \frac{Ca_{inc}\,\delta(t - t_0)}{v}}{(1 + \kappa_B + \kappa_S)} \quad (12)$$

(Neher and Augustine, 1992) linearized Eq. 12 to simplify the solution for this equation in case the baseline for $[Ca^{2+}]_i$ is constant, the exogenous buffer $[B_T]$ is constant and does not influence the baseline Ca^{2+} and when amplitudes of the transients are small. Tank et al. (Tank et al., 1995) define 'small' as smaller than 0.5 $K_{d,Fura}$. Under these conditions the decay of a Ca^{2+}- transient can be described by a monoexponential whose time constant is given by:

$$\tau_{transient} = v\frac{(1+\kappa_B+\kappa_S)}{\gamma - \frac{(1+\kappa_S)v}{\tau_{loading}}} \quad for: \begin{matrix} baseline = const \\ [B_T] = const \\ small\ \Delta[Ca^{2+}]_i \end{matrix} \tag{13}$$

$\tau_{transient}$ is proportinal to κ_B and a linear fit to the data has its negative x-axis intercept at $1 + \kappa_S$, yielding the endogenous Ca^{2+} buffering capacity of the cell. The slope of this fit denotes the Ca^{2+} removal mechanism γ (Eq. 10). The y-axis intercept yields the time constant τ for the decay of the Ca^{2+} transient as it would appear in the cell without exogenous buffer.

2.7 Analysis of calcium buffering

After establishing the whole-cell configuration neurons were voltage clamped at their resting potentials (~ -60 mV) and intracellular dye loading was monitored at 360 nm excitation, the isobestic point of fura-2. Frames were taken in 30 s intervals (7 ms exposure time). We estimated the intracellular fura-2 concentration for different times during the loading curve, assuming that cells were fully loaded when the fluorescence reached a plateau and the fura-2 concentration in the cell and in the pipette is equal (200 μM) (Lee et al., 2000). To control the physiological status of the cell, loading curves were also measured at 380 nm. Divergence between the 360 nm and 380 nm loading curve indicated rising Ca^{2+} concentration, related to beginning cell death.

During fura-2 loading voltage-activated Ca^{2+} influx was induced by stepping the voltage clamped membrane potential for 50 ms to +5 mV, which is in the range where I_{Ca} has its maximum (Husch et al., 2008). To monitor the induced Ca^{2+} transients ratiometrically, pairs of images at 340 nm (15 ms exposure time) and 380 nm (6 ms exposure time) excitation were aquired with a rate of 13.3 Hz for ~12s. Typically 3 Ca^{2+} transients were induced during a loading curve at different intracellular fura-2 concentrations approximately 50 s, 200 s and 500 s after establishing the whole-cell configuration. Before the whole cell configuration was established (break in), a background image was obtained in on cell mode for each wavelength with the same camera settings. Background fluorescence was then subtracted from each image of the series.

2.7.1 Fitting the loading curve

The increase in fluorescence was measured at the 'isobestic' wavelength of fura-2 to monitor loading of fura-2 into somata the neurons (Fig. 8A and C). The loading curves were fit with the exponential function:

$$Y = Y_{max} \cdot \left(1 - e^{(-(time - t_{bi}) \cdot RL)}\right) \tag{14}$$

Y is the fluorescence intensity in adu or, after rescaling, the concentration of fura-2. Y_{max} is the plateau of fluorescence or the maximum concentration of fura-2 (200 μM), RL is the inverse of the loading time constant (in s^{-1}), t_{bi} is the time of break-in.

Initially the data were fit with Eq. 14 using the least square method implemented by the 'R function' nls (Nonlinear Least Squares). Reasonable 'initial guesses' were obtained by the 'R function' 'SSasympOff' (Asymptotic Regression Model with an Offset). To provide the absolute fura concentrations during the time course of the experiment the fluorescence intensity was rescaled to fura-2 concentrations

(Y_{max} = 200 μM) and the rescaled data were fit again with Eq. 14 using 'nls'. This fitting procedure describes the overall loading process very well. On a shorter time scale, however, the data sometimes fluctuated around the fit (Fig. 10 A), probably due to changes in series resistance (Helmchen et al., 1996). Improved estimates of the fura-2 concentration at any time throughout the loading could be obtained from subsequent smoothing splines fits (Fig. 10B), which were computed with the 'R function' 'smooth.spline'. For the analysis of calcium buffering the fura-2 concentrations obtained from the smoothing spline fit were used.

2.7.2 Fitting the transients

Fluorescence ratios (R) measured at 340 and 380 nm (13.3 Hz) after a brief Ca^{2+} influx were used to monitor the time course of these transients. Data for each wavelength were acquired in adu from a rectangular region of interest. These adu counts were used to compute ratios that were then transformed to absolute Ca^{2+} concentrations as described above. The decay of the transient was fitted with the monoexponential function:

$$[Ca^{2+}]_i = S_{drift} \cdot t + [Ca^{2+}]_{i,0} \cdot e^{\frac{-t}{\tau}} \quad (15)$$

$S_{drift} \cdot t$ is a linear drift term taking baseline shifts into account (with S_{drift} for the slope and t for time), $[Ca^{2+}]_{i,0}$ the amplitude of the signal at t = 0 and τ the decay constant. Parameters of Eq. 15 were fit using 'nls'. 'Initial guesses' for S_{drift} were obtained from the baseline, for $[Ca^{2+}]_{i,0}$ from subtracting the baseline of the signal from the amplitude, and for τ from the time point where the amplitude had decreased e-fold.

2.7.3 Fitting the linearized Model

Time constants of transients were plotted over κ_B values and fitted with a linear function $Y = \beta_0 + \beta_1 * x$ using the 'R function' 'lm'. To estimate the variance of the slope (extrusion rate γ), the y-axis intercept (endogenous decay constant τ) and the negative x-axis intercept (endogenous Ca^{2+} binding ratio κ_S) we used the bootstrap method (Efron, 1979) implemented in the boot library in R (fixed-x resampling, 1000 bootstrap samples). This resulted in distributions (n=1000) for each of the parameter estimates (i.e. extrusion rate γ, endogenous decay constant τ and endogenous Ca^{2+} binding ratio κ_S). The distributions for each parameter were then log-transformed for statistical analysis. For pairwise comparisons of cell types, Student's pairwise t-tests were used to assess statistical significance. Significances were accepted at $P < 0.001$.

2.8 Analysis of odor evoked calcium signals

After establishing the whole-cell configuration neurons were voltage clamped at their resting potentials (~ -60 mV) and activation protocols (-100 mV prepulse of 500 ms duration, 50 ms voltage steps in 10 mV increments) were induced to measure the whole-cell currents. Then the mode was switched to current clamp and depolarizing currents were injected to test, if action potentials could be elicited. Neurons were then held in current clamp mode (~ -200 pA) for about 45 min to allow for dye loading. Up to six single component odors were then puffed for 500 ms onto the ipsilateral antenna to elicit Ca^{2+} influx. The induced Ca^{2+} transients were monitored by images acquired at 490 nm (50 ms exposure time) at 13.3 to 20 Hz for typically 8 s. Ca^{2+} signals were obtained from regions of interest defined on the images. To remove background from these signals, first the kinetic was fit with a biexponential function omitting the period of Ca^{2+} influx, which

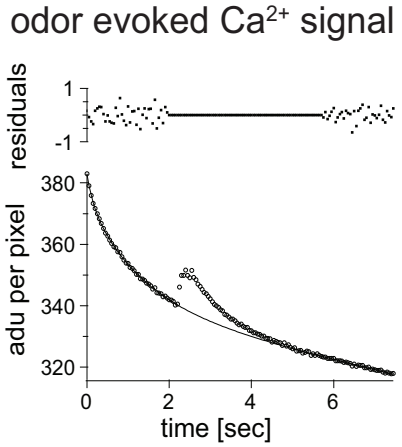

Figure 5: Raw odor evoked Ca^{2+} signal from a type I LN
Example of a raw Ca^{2+} signal after odor stimulation (in this case citronellal). The Ca^{2+} kinetic of a series of images was obtained from a region of interest. The kinetic was fitted with a biexponential function omitting the period of Ca^{2+} influx (from 2 to 6 seconds). The whole kinetic was then divided by the fit resulting in a background removed, normalized kinetic. Residuals indicate that the function fits well the background.

started 2 seconds after signal onset and had decayed back to resting level 6 seconds after signal onset. Second, the whole kinetic was divided by the fit, resulting in a relative signal, normalized to 1 ($\Delta F/F + 1$) with dynamically removed background (see Fig. 5).

2.9 Odor stimulation

To deliver odors we used a continuous air flow system in accordance with Vetter et al. (2006). Carbon-filtered, humidified air flowed continuously across the antennae at a rate of 2 l min^{-1} through a glass tube (10 mm ID) that was placed perpendicular to and within 10 mm of the antennae. To quickly remove odors a vacuum funnel (3.5 cm ID) was placed 5 cm behind the animal. 5 ml of the liquid odorants (pure or diluted in mineral oil [M8410, Sigma]) were filled in 100 ml glass vessels. During a 500 ms odor stimulus 22.5 ml of the headspace was injected into the airstream. To ensure a continuous air flow volume across the preparation the

air to deliver the odor was taken from the airstream by a solenoid system. The solenoids were controlled by the D/A-interface of the EPC9 patch-clamp amplifier that was controlled by the Pulse software. All odorants were dissolved in mineral oil with a final volume of 5 ml and adjusted to the odor with the lowest vapor pressure (eugenol). Stripes of filter paper were used to increase the surface. Concentrations were as follows: eugenol 100 % (E5504, Sigma), α-ionone 72.4 % (I-3384, Sigma), citral 14.6 % (C8,300-7, Sigma), citronellal 4.9 % (C-2513, Sigma). The headspace of mineral oil was used as control stimuli ('blank'). Odor stimuli were at least 60 s apart.

2.10 Histology

2.10.1 Single cell labelling

To label single cells, 1% biocytin (B4261, Sigma) was added to the pipette solution. After the recordings, the brains were fixed in Roti-Histofix (P0873, Carl Roth, Karlsruhe, Germany) overnight at 4 °C and rinsed in 0.1 M Tris-HCl buffered solution (TBS; pH 7.2, 3 x 10 min). To facilitate the streptavidin penetration the brains were treated with an enzyme mixture (collagenase/dispase, 1 mg ml^{-1} [269638, Roche Diagnostics, Mannheim, Germany] and 1 mg ml^{-1} hyaluronidase [H3506, Sigma-Aldrich] in TBS, 20 min, 37 °C), rinsed in TBS (3 x 10 min, 4 °C) and incubated in TBS containing 1% Triton X-100 (30 min, RT, Serva, Heidelberg, Germany). Afterwards, the brains were incubated in Alexa Fluor 633 (Alexa 633) conjugated streptavidin (1:600, 1-2 days, 4 °C, S21375, Molecular Probes, Eugene, OR) that was dissolved in TBS containing 10% Normal Goat Serum (S-1000, Vector Labs, Burlingame, CA). Brains were rinsed in TBS (3 x 10 min, 4 °C), dehydrated, cleared and mounted in methylsalicylate (M6752, Sigma-Aldrich).

2.10.2 Confocal microscopy

The fluorescence images were captured with a confocal microscope (LSM 510 Meta, Carl Zeiss, Göttingen, Germany) equipped with Plan-Neofluar 10x (0.3 NA), Plan-Apochromat 20x (0.75 NA), and Plan-Apochromat 63x (1.4 NA Oil) objectives. Streptavidin-Alexa 633 was imaged with 633 nm excitation, emission was collected through a 650 nm LP filter. For overviews stacks were acquired with the 10x or 20x objective, adjusted for contrast and brightness and overlayed in ImageJ (Version v1.35d with the WCIF plugin bundle [www.uhnresearch.ca/facilities/wcif/]).

2.11 Tools for data analysis

Electrophysiological data were analysed with the software Pulse (version 8.63, HEKA-Electronic) and Igor Pro 6 (Wavemetrics) inclucing the Patcher's Power Tools extension (http://www.mpibpc.gwdg.de/abteilungen/140/software/index.html). The MaxChelator program was used to compute the free metal concentrations (Mg^{2+} and Ca^{2+}) in EGTA buffered solutions, which were used for calibration of the Ca^{2+} indicator fura-2 (WinMaxc32 version 2.50, http://www.stanford.edu/~cpatton/maxc.html).

All functions (Eq. 13, 14 and 15) that were used to fit Ca^{2+} buffering related data with a linearized one compartment model were implemented in R using the 'R functions' 'nls', 'smooth.spline' and 'lm', respectively.

3 Results

This study comprises two independent parts. In the first part, parameters related to general Ca^{2+} handling were quantified in a) isolated oflactory interneurons from the AL of adult *P. americana* and b) in somata of identified uPNs and two types of LNs. In the second part, odor evoked Ca^{2+} signals in subcellular compartments were qualitatively and quantitatively compared between uPNs and two types of LNs. Both times neuron types had to be unequivocally identified.

The results are structured as follows. After a short description of the recorded neuron types (section 3.1) it is demonstrated how they were identified for the analysis of Ca^{2+} buffering and odor evoked Ca^{2+} signals. Then the results of the two parts about Ca^{2+} buffering (section 3.2) and odor evoked Ca^{2+} signals (section 3.3) follow.

3.1 Identification of neuron types

Experiments were performed on a) uniglomerular projection neurons, b) type I interneurons, c) type II interneurons, and d) local interneurons yet unidentified (section 3.3 only). Different neuron types were categorized as proposed by Husch (2007). The previously well described uniglomerular projection neurons (Distler and Boeckh, 1997a) served as a reference. They have been identified as a ventrolateral group of somata within the antennal lobe. This cluster served as a

landmark to find the more dorsoventrally located type I and type II interneurons. Relative location, morphology and parts of the physiology of these neuron types have been described before (Distler, 1989; Distler and Boeckh, 1997b; Distler and Boeckh, 1997a; Malun et al., 1993). Uniglomerular projection neurons have a very characteristic morphology with the somata in the mentioned cluster. They are connected to a very densely innervated single glomerulus. From a single branching point in the antennal lobe a neurite seperates to connect the deuto- and protocerebrum through the inner-antenno-cerebral tract, which then arborizes in the protocerebrum (Malun et al., 1993). They respond to odors of many different chemical classes, often with elaborate patterns of excitation and spiking that can also include periods of inhibition. Responses are usually very odor specific and extremely robust, when the same odor is presented several times (Husch, 2007). Type I and type II interneurons are morphologically confined to the antennal lobe. Type I LNs innervate many but not all glomeruli and the intraglomerular innervation is homogenous, with interglomerular differences in the innvervation density. Type II LNs innervate all glomeruli and the glomeruli are similarly dense innervated. Upon odor stimulation type I LNs react, like uPNs, with overshooting action potentials (Fig. 22C). However, their responses to different odors are not as diverse as in uPNs. The responses to repeated stimulation with the same odor are not as stereotypic as in uPNs (Husch, 2007). In contrast to these neuron types, in type II LNs odor stimulation never evokes sodium driven action potentials. Type II LNs react to odors with small depolarizations that can have small Ca^{2+} driven spikelets on top (Fig. 21C). Like in type I LNs, in type II LNs the reaction to different odors is not as diverse as in uPNs. The responses to repeated stimulation with the same odor is not as stereotypic as in uPNs. (Husch, 2007).

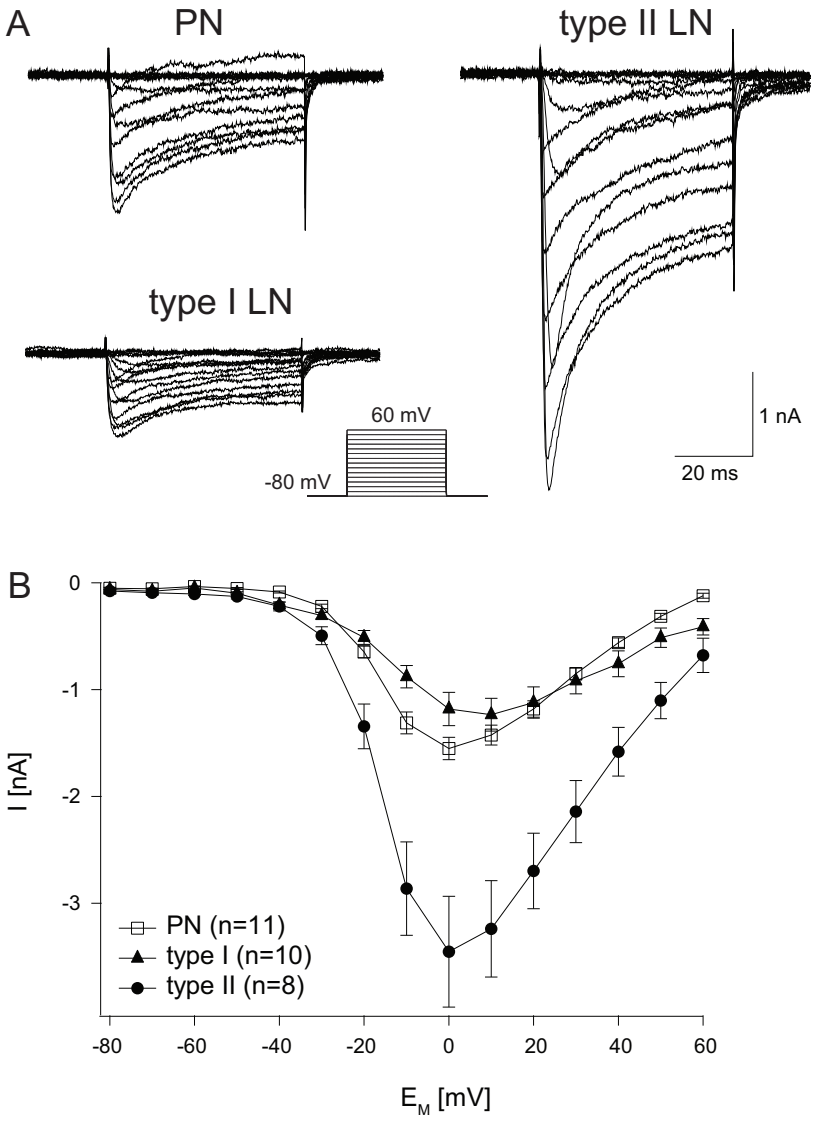

Figure 6: Calcium currents from identified neurons
*(**A**) Calcium currents from a uPN, a type I and a type II LN. The neurons were depolarized for 50 ms from a holding potential of -80 mV to 60 mV in 10 mV increments. Calcium currents were isolated by blocking voltage activated sodium and potassium currents. Note that the absolute current amplitude is much greater in type II LN than in uPN or type I LN. (**B**) I-E relation of calcium currents recorded from uPN, type I and type II LN. Results are well comparable to previous studies of Husch (2007). Data is from neurons that were later used for analysis with the single compartment model of Ca^{2+} dynamics. Neurons could be classified by their I-E relation, soma position within the antennal lobe and soma size. Values are mean ± SE.*

3.1.1 Identification of neurons for the analysis of Ca^{2+} buffering

In this part of the study I analyzed cellular parameters of insect olfactory interneurons that determine the intracellular Ca^{2+} dynamics. The experiments were

performed on somata of a) isolated olfactory interneurons from the antennal lobe of adult *P. americana* in short term cell culture (in vitro) and b) on somata of identified uniglomerular projection neurons and two types of identified local interneurons in an intact brain preparation (in situ) from adult male *P. americana*. In situ the neurons were first identified using IR-DIC by the position and size of the somata. Subsequently, the identity was confirmed by the electrophysiological (see Fig. 6) and morphological characteristics. The later were revealed by the single cell label provided by the Ca^{2+} indicator fura-2.

3.1.2 Identification of neurons for the analysis of odor evoked Ca^{2+} signals

In this part of the study other physiological and morphological characteristics than in the previous part could be assessed to identify the different neuron types.

Conditions that had to be met to categorize neurons as uPNs were: response to at least one odor with action potentials, action potentials from depolarizing current injection (see Fig. 7A, current clamp) and a typical combination of TTX sensitive sodium current and TEA/4-AP sensitive potassium current from voltage-clamp steady state activation protocols (holding potentials of -100 mV in 10 mV increasing voltage steps, see Fig. 7A, voltage clamp). Furthermore, the morphological reconstruction showed that this type of uniglomerular projection neurons projected its axon from the glomerulus through the inner antennocerebral tract to the calyces of the mushroom bodies and the lateral lobe of the protocerebrum (Fig. 23C).

Conditions that had to be met to categorize neurons as type I LNs were: response to at least one odor with action potentials, action potentials from depolarizing current injection (see Fig. 7B, current clamp), sodium carried inward currents and transient and sustained outward currents carried by potassium from voltage-clamp steady state activation protocols (holding potentials of -100 mV in 10 mV

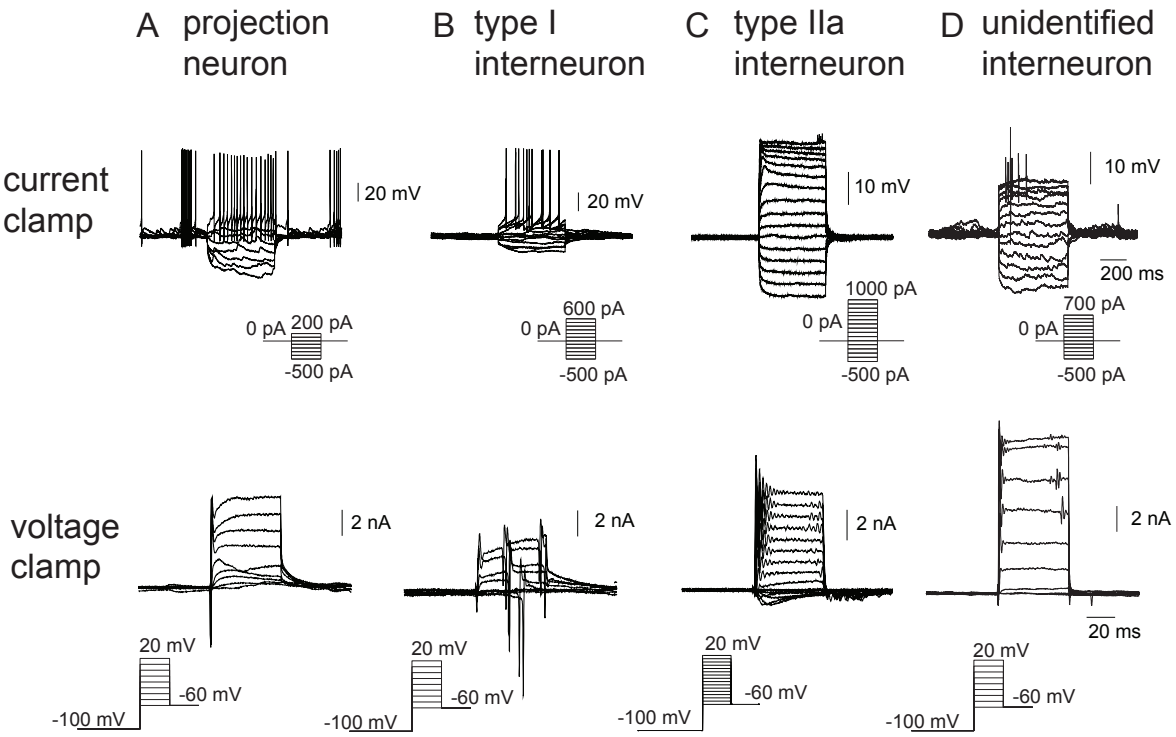

Figure 7: Electrophysiological characteristics of different neuron types
*Different neuron types were identified in this study with a combination of strategies, including current- and voltage-clamp properties. (**A**) Current-clamp (upper trace) and voltage-clamp (lower trace) protocols from projection neurons. Depolarizing current injection elicited action potentials. Current was injected for 500 ms from -500 pA to 200 pA in 100 pA increments from a holding current of 0 pA. Voltage-clamp protocols with 50 ms voltage steps from holding potentials of -100 mV to 20 mV in 10 mV increments elicited a combination of transient Na^+ driven inward, transient and sustained K^+ driven outward currents. (**B**) Current-clamp (upper trace) and voltage-clamp (lower trace) protocols from type I LNs. Depolarizing current injection elicited action potentials. Protocol as in (A) but more positive currents were injected (600 pA). Voltage-clamp protocols as in (A) elicited a combination of Na^+ driven transient inward, transient and sustained K^+ driven outward currents. Due to imperfect voltage control fast inward and outward currents were elicited at the beginning and during the voltage steps. (**C**) Current-clamp (upper trace) and voltage-clamp (lower trace) protocols from type II LNs. Depolarizing current injection did not elicit action potentials. Protocol as in (A) but more positive currents were injected (1000 pA). Voltage-clamp protocols as in (A) elicited a sustained Ca^{2+} driven inward, transient and sustained K^+ driven outward current, but no sodium currents were elicited. (**D**) Current-clamp (upper trace) and voltage-clamp (lower trace) protocols from a yet unidentified neuron. Depolarizing current injection elicited action potentials. Protocol as in (A) but more positive currents were injected (700 pA). Action potentials were smaller as in (A) and (B). Voltage-clamp protocols as in (A) elicited transient and sustained outward currents and small unidentified inward currents.*

increasing voltage steps, see Fig. 7B, voltage clamp). Last, the morphological reconstruction had to confirm that multiple glomeruli were innervated with interglomerular different densities (see Fig.s 18 and 22A). Fig.s 18 and 22 show

two neurons that both met the conditions of type I LNs, albeit their odor responses differ on the glomerular level. The neurons will subsequently be categorized according to their glomerular response profile.

Conditions that had to be met to categorize neurons as type II LNs were: response to at least one odor with small depolarizations that could have small spikelets on top (Fig. 21C), no action potentials from depolarizing current injection (Fig. 7C, current clamp), no sodium carried transient inward current, but a sustained Ca^{2+} carried inward current and transient and sustained outward currents carried by potassium from voltage-clamp steady state activation protocols (holding potentials of -100 mV in 10 mV increasing voltage steps, Fig. 7C, voltage clamp). Furthermore, the morphological reconstruction had to confirm that all glomeruli were similarly innervated (Fig. 21A).

One neuron was found in this study that did not meet the conditions of the type I or type II LN categories. The neuron responded to all odors presented, but with different sometimes elaborate patterns of depolarizations and spiking (Fig. 19). Odor stimulations evoked action potentials of different amplitudes (~25 - 35 mV) and action potential-like oscillations (spikelets), suggesting that there were several spike-generating zones. These responses rode on long lasting depolarizations. The oscillatory excitatory answer was always followed by a hyperpolarization. Depolarizing current injection did induce action potentials like in type I LNs, but more depolarizing current was needed, action potentials were much smaller (~13 mV compared to ~70 mV) and arose with a delay to the stimulus onset (Fig. 7D, current clamp). This lead to the assumption that they were generated more peripherally. In voltage-clamp steady state activation protocols (holding potentials of -100 mV in 10 mV increasing voltage steps, see Fig. 7D, voltage clamp) small unidentified inward currents were visible and transient and sustained outward currents. Assuming that perfect voltage control was only achieved in the cell body

and not in distal parts of the neuron (Bar-Yehuda and Korngreen, 2008), it seems conclusive that this neuron type cannot produce action potentials in the cell body, but they do arise in the periphery. Last, the morphology showed that this neuron innervated multiple glomeruli similarly dense, but not all. The arborizations were generally finer than in the previously described type I and type II LNs (Fig. 20A).

3.2 Calcium buffering

Using the added buffer approach in combination with electrophysiological recordings and optical imaging I aimed to quantitatively analyze the Ca^{2+} influx ($j_{in.\,Stim}$, Eq. 8), the Ca^{2+} binding ratio κ_S (Eq. 9) and the extrusion rate γ (Eq. 10), which are all cellular parameters that determine cytosolic Ca^{2+} dynamics.

3.2.1 Calcium influx and calcium resting level

The neurons were voltage clamped at their resting potential (-60mV). Ca^{2+} transients were elicited by stepping the voltage-clamped membrane potential for 50 ms to +5 mV, which is in the range where I_{Ca} is maximal (Husch, 2007). Using ion substitution and pharmacological blockers it has also been demonstrated that this current is indeed carried by Ca^{2+} (Husch, 2007). Thus, the amount of current could be used for estimating Ca^{2+} influx and the increase in total Ca^{2+} concentration. Monitored by optical Ca^{2+} imaging the Ca^{2+} influx induced a clear and reproducible Ca^{2+} signal.

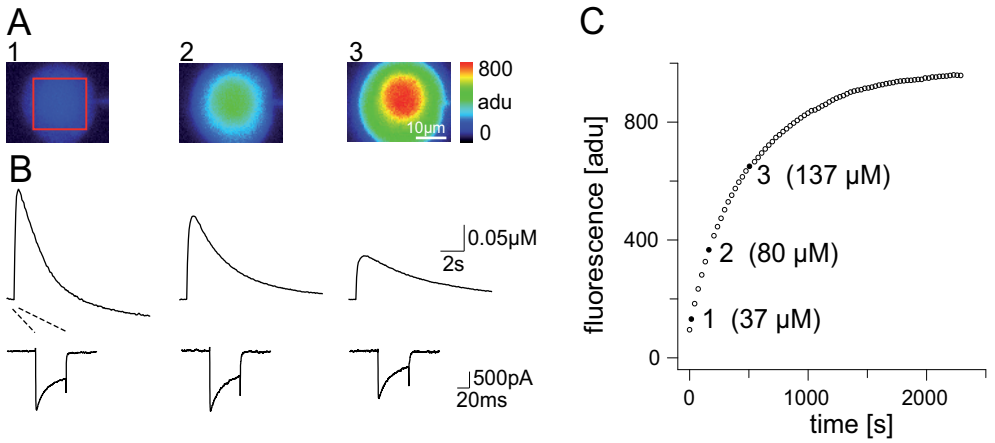

Figure 8: Acquisition of loading curve and Ca^{2+} decay kinetics
*(**A**) Fluorescence images acquired in analog-to-digital units [adu] of a cultured cell at 360 nm excitation wavelength. Images were taken during loading of fura-2 at times indicated in (C). The series of images demonstrates inceasing dye concentration (cold colors reflect low intensity, warm colors reflect high intensity). (**B**) Converted signals from ratio images into calcium kinetics taken at fura-2 concentrations indicated in (C). Corresponding Ca^{2+} currents (lower trace) from patch-clamp recordings. (**C**) Calcium independent fluorescence (at isobestic point) for different times after establishing the whole-cell patch clamp configuration as measured from a rectangular region of interest within images shown in (A).*

Absolute Ca^{2+} influx

The total charge influx during a voltage pulse is given by $\int dI/dt = Q_{ca}$. Accordingly the Ca^{2+} influx is: $nCa = Q_{Ca}/2F$. The average Ca^{2+} influx during a 50 ms voltage step from -60 mV to +5 mV was 0.22 ± 0.05 fmol (n = 20) in the cultured AL neurons, 0.30 ± 0.15 fmol (n = 11) in PNs, 0.12 ± 0.08 fmol (n = 10) in type I LNs and 0.50 ± 0.17 fmol (n = 8) in type II local interneurons (Fig. 9 A).

Cell volume

Assuming the cell bodies are homogeneous spheres, the volume was estimated from the whole cell capacitance using (all values from Hille, 2001): $C = \varepsilon\ \varepsilon_0\ A / d$. ε is the dielectric constant of the cell membrane ($\varepsilon = 2.1$), ε_0 is the polarizability of free space ($\varepsilon_0 = 8.85 \times 10\text{-}12\ CV^{-1}m^{-1}$), d its thickness (d = 2.3 nm) and A is the area of the cell membrane. The specific capacitance of the cell membrane therefore is 1 pF/100 µm^2. Accordingly the volume is $V = A^{3/2}/6\sqrt{Pi}$. The whole-cell capacitance was measured using the capacitance compensation (C-slow) of the EPC9. All

calculations were performed with the Patcher's-Power-Tools plug-in (http://www.mpibpc.gwdg.de/abteilungen/140/software/index.html) for Igor Pro. The mean volume for cell bodies in vitro was 17 ± 6 pL (n = 20). In vivo the somata volume for projection neurons was 13 ± 2 pL (n = 11), for type I 23 ± 9 pL (n = 10) and for type II local interneurons it was 57 ± 18 pL (n = 8) (Fig. 9 B).

Total Ca^{2+} concentration

The increase in total intracellular Ca^{2+} concentration ($\Delta[Ca^{2+}]_{tot}$) during the voltage pulse was determined from the Ca^{2+} influx and the cell volume. The change in total (average) calcium concentration reflects the sum of the change in free calcium $\Delta[Ca^{2+}]_i$ and the change of bound calcium Δ[SCa], which will be determined below. The total increase in cytosolic Ca^{2+} concentration was in vitro 14 ± 5 μM (n = 20), in projection neurons the total cytosolic Ca^{2+} concentration increased by 25 ± 14 μM (n = 11), in type I local interneurons by 6 ± 4 μM (n = 10) and in type II local intereneurons by 9 ± 3 μM (n = 8) (Fig. 9 C).

Resting Ca^{2+} concentration

The absolute concentrations of free Ca^{2+} were determined from the ratioed imaging signals applying the approach from Grynkiewicz (Grynkiewicz et al., 1985) (see Eq. 2). We used two methods for calibration: a) in vivo (in living cells) and b) in vitro (in solution). For in vivo calibration, the calibration solutions (R_{min}: no Ca^{2+}, R_{def}: 0.14 μM Ca^{2+}, R_{max}: 10 mM Ca^{2+}) were introduced in the cell via the patch pipette. When the fluorescence, imaged at the isobestic point of fura-2 (360 nm), had reached equilibrium, ratio images (from 340 nm and 380 nm excitation) were acquired for each solution. The acquired values were: R_{max} = 2.701 ± 0.479 (n = 10), R_{min} = 0.136 ± 0.009 (n = 6), R_{def} = 0.231 ± 0.066 (n = 13), $K_{d,Fura,eff}$ = 3.637 ± 2.573 μM, isocoefficient α = 0.205, resulting in a K_d for fura of $K_{d,Fura}$ = 0.427 μM. For

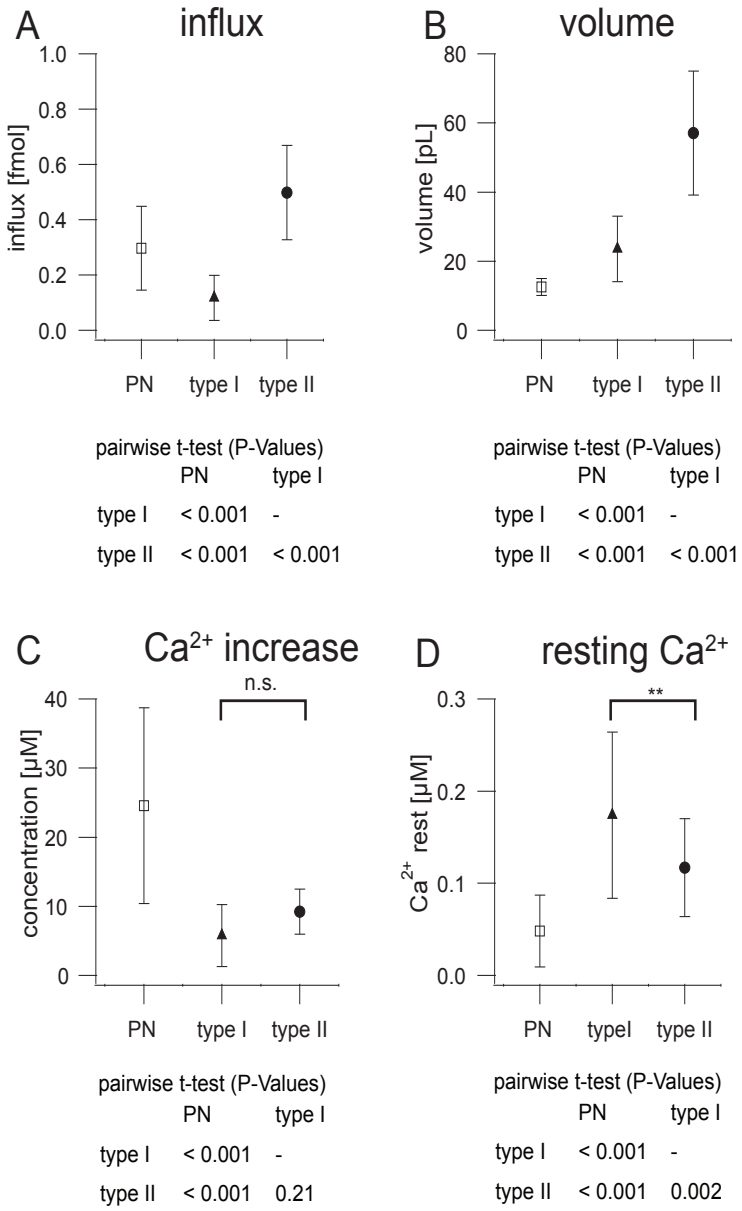

Figure 9: Parameters of Ca^{2+} influx, cell volume and resting level

*Average values related to Ca^{2+} influx and volume from the studied neuron types (uPN, type I LN, type II LN) (**A**) Average total charge influx during a 50 ms voltage pulse. Charge influx was determined from the patch-clamp recording trace with nCa = QCa/2F. Largest absolute influx was found in type II LNs, smallest in type I LNs. PNs had an intermediate absolute influx. (**B**) Average volume of the cell. Largest volume was found in type II LNs, lowest in uPNs. Type I LNs had an intermediate volume. (**C**) Average Ca^{2+} increase. Largest increase was found in uPNs, lowest in type I and type II LNs. The latter were not significantly different from each other. (**D**) Average resting Ca^{2+} concentration, determined from the baseline of the signals before stimulation. Highest resting level was found in type I LNs, lowest in uPNs. Type II LNs had intermediate resting level. For pairwise comparisons, Student's pairwise t-tests were used to assess statistical significance. Significance levels were always below $p < 0.001$, except in the marked cases. Significance levels (**) $p < 0.005$, (n.s.) not significant. Number of recordings: uPN, n = 11; type I LN, n = 10, type II LN, n = 8.*

in vitro calibration, a drop of each calibration solution (75 µl, R_{min}: no Ca^{2+}, R_{def}: 0.14 µM Ca^{2+}, R_{max}: 10 mM Ca^{2+}) was placed on a sylgard coated recording chamber. Ratio images (from 340 nm and 380 nm excitation) were acquired for each solution. The acquired values were: correction factor (Poenie, 1990) R_d = 0.77, resulting in: R_{max} = 1.130 ± 0.157 (n = 9), R_{min} = 0.132 ± 0.005 (n = 9), R_{def} = 0.290 ± 0.011 (n = 9), $K_{d,Fura,eff}$ = 0.744 ± 0.147 µM, isocoefficient α = 0.212. According to Eq. 5 the K_d for fura was $K_{d,Fura}$ = 0.191 µM.

The mean resting level of free Ca^{2+} just before the stimulation was in vitro 0.212 ± 0.216 µM (n = 20), in projection neurons 0.048 ± 0.039 µM (n = 11), in type I local interneurons 0.174 ± 0.09 µM (n = 10) and in type II local interneurons 0.117 ± 0.053 µM (Fig. 9 D).

3.2.2 Dye concentration from loading curves

The intracellular concentration of the calcium indicator at any time during the experiment was determined from the loading curves. The cells were loaded via the patch pipette with intracellular solution containing 200 µM fura-2. During dye loading the flourescence of the cell body was monitored at 360 nm excitation to determine the dye concentration and at 380 nm excitation to control the condition of the cell. After establishing the whole-cell configuration, fluorescence in the cell bodies appeared within seconds and fluorescence intensity increased until it reached a stable value. During loading fluorescence images were obtained in 30 s intervals. The time course of increasing fluorescence (loading curve) were fitted with an exponential function (Eq. 14). Such a loading curve of a cell body is shown in Fig. 10.

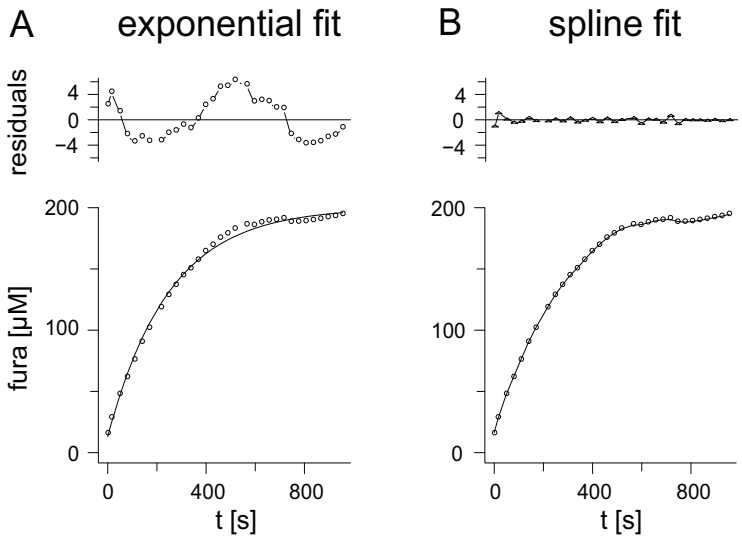

Figure 10: Analysis of loading curves
*(**A**) Calcium independent fluorescence (at isobestic point) was monitored from a rectangular region of interest centered over the cell body after establishing the whole-cell patch clamp configuration until saturation was reached. The data was fitted with a monoexponential function (eq. 14). The asymptotic value of this fit was assumed to correspond to a fully loaded cell with the dye concentration of the pipette (200 µM). The raw fluorescence obtained in adu was then rescaled to fura concentration such that the asymptotic value equals 200 µM. The rescaled data was refitted with a monoexponential model (solid line). (**B**) Loading curve in (A) was fit again with a smoothing spline. The residuals indicate that the fit was significantly improved compared to a monoexponential function.*

The average time constant for dye loading determined from the exponential fits (Eq. 14) was 907 s for the in vitro (n = 20) experiments and 1383 s (n = 29) for in situ recordings. On a shorter time scale the data sometimes fluctuated around the exponential fit, probably due to variations in access resistance (Helmchen et al., 1996). To account for these variations and to determine the instantaneous dye concentration more precisely we fitted the data a third time with a smoothing spline fit routine for which we used the parameters from the second fit as 'initial guesses'. The improvement that is achieved by using this approach is demonstrated in Fig. 10, in which the residuals of the two fitting procedures are compared.

3.2.3 Buffering

The kinetics of cytosolic Ca^{2+} signals are strongly dependent on the endogenous and exogenous (added) Ca^{2+} buffers of the cell. The amplitude and decay rate of the free intracellular Ca^{2+} is changing with increasing exogenous buffer concentration: the amplitude of free Ca^{2+} is decreasing and the time constant τ of the decay is increasing, as shown in Fig. 8.

If the buffer capacity of the added buffer is known, the time constant of decay $\tau_{transient}$ can be used to deconvolute the Ca^{2+} signal to conditions, in which only endogenous buffers are present ($-\kappa_B = 1 + \kappa_S$). The model used for this study (Neher and Augustine, 1992, Eq. 13) assumes that the decay time constants $\tau_{transient}$ is a linear function of the Ca^{2+} binding ratio κ_B. κ_S was determined from the negative x-axis intercept of this plot (Fig. 11 - 14). The point of intersection of the linear fit with the y-axis denotes the endogenous decay time constant τ_{endo}. The slope of the fit reflects the linear extrusion rate γ. The endogenous Ca^{2+} binding ratio was in vitro 317 ± 144, in projection neurons 418 ± 152, in type I local interneurons 154 ± 49 and in type II local interneurons 672 ± 280. The endogenous decay time constant was in vitro 3.7 ± 0.5 s, in projection neurons 1.8 ± 0.3 s, in type I local interneurons 1.1 ± 0.2 s and in type II local interneurons 2.2 ± 0.2 s. The extrusion rate could be determined with 84 ± 29 s-1 in vitro, in projection neurons it was 221 ± 44 s-1, in type I local interneurons 141 ± 19 s-1 and in type II local interneurons 305 ± 101 s-1.

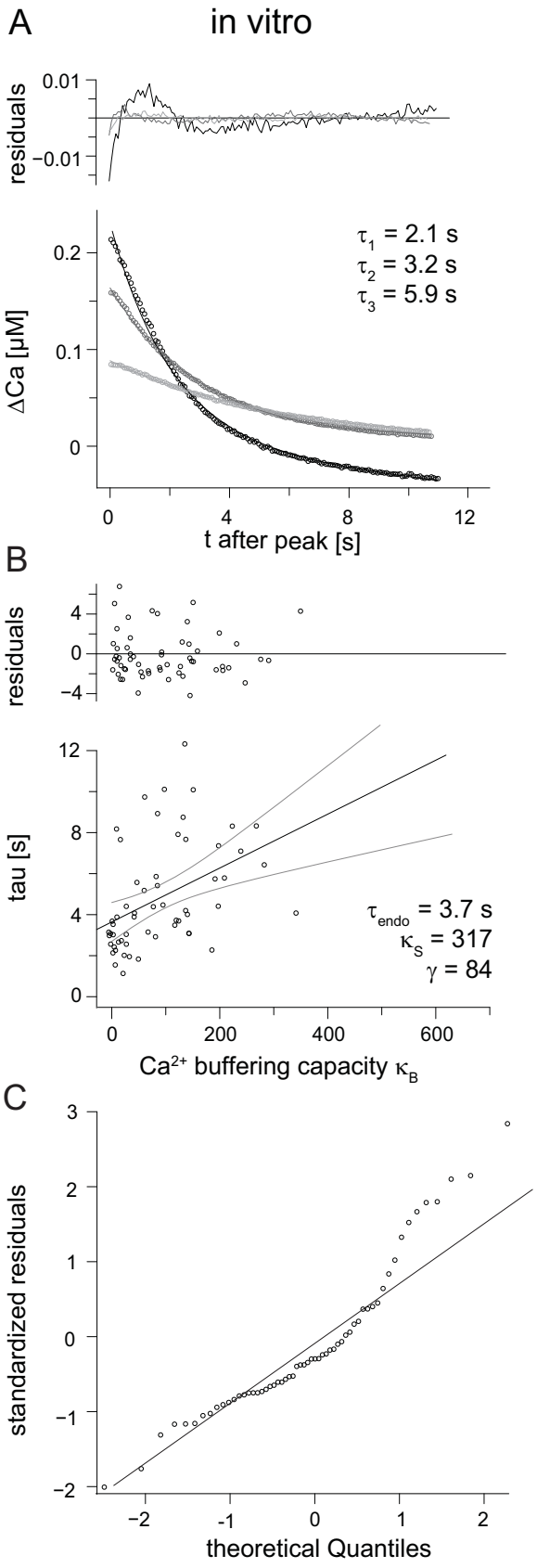

Figure 11: Analysis of Ca^{2+} buffering in cultured neurons

*(**A**) Decay of Ca^{2+} after a short (50 ms) depolarization from -60 mV to 5 mV at increasing fura-2 concentrations in the cell. Black: 26 μM, red: 69 μM, green: 128 μM. Ca^{2+} transients were baseline-subtracted, which was acquired just before each stimulation. Note that the first transient (black) undershoots below the baseline. This is probably due to an elevated resting Ca^{2+} level caused by the membrane disrupture, which is slowly compensated therefore reducing the baseline. Transients were fit from peak to the end of signal with a single exponential function (solid lines, τ_1, τ_2, τ_3 as indicated in the figure). Residuals indicate that transients can be well approximated with monoexponentials, however a trend to a deviation from a monoexponential is noticable for large transients. (**B**) Decay constants of Ca^{2+} transients as determined in (A) were plotted against Ca^{2+} buffering capacity κ_B, which is calculated from the concentration of fura-2 in the cell, the K_d of fura-2 and the baseline Ca^{2+} concentration (see Methods). The data was fit with a linear function, which is used to extrapolate the endogenous decay constant τ_{endo} = 3.7±0.5 s (y-axis intercept), the endogenous Ca^{2+} binding ratio κ_S = 317±144 (negative x-axis intercept) and the extrusion rate γ = 84±29 s^{-1} (slope). Dotted lines indicate 90% confidence bands. (**C**) Normal Q-Q plot of the linear model and the data points in (B). In this case it is critical to accept the hypothesis that the data can be described with a linear model as the distribution does not fall closely to a straight line.*

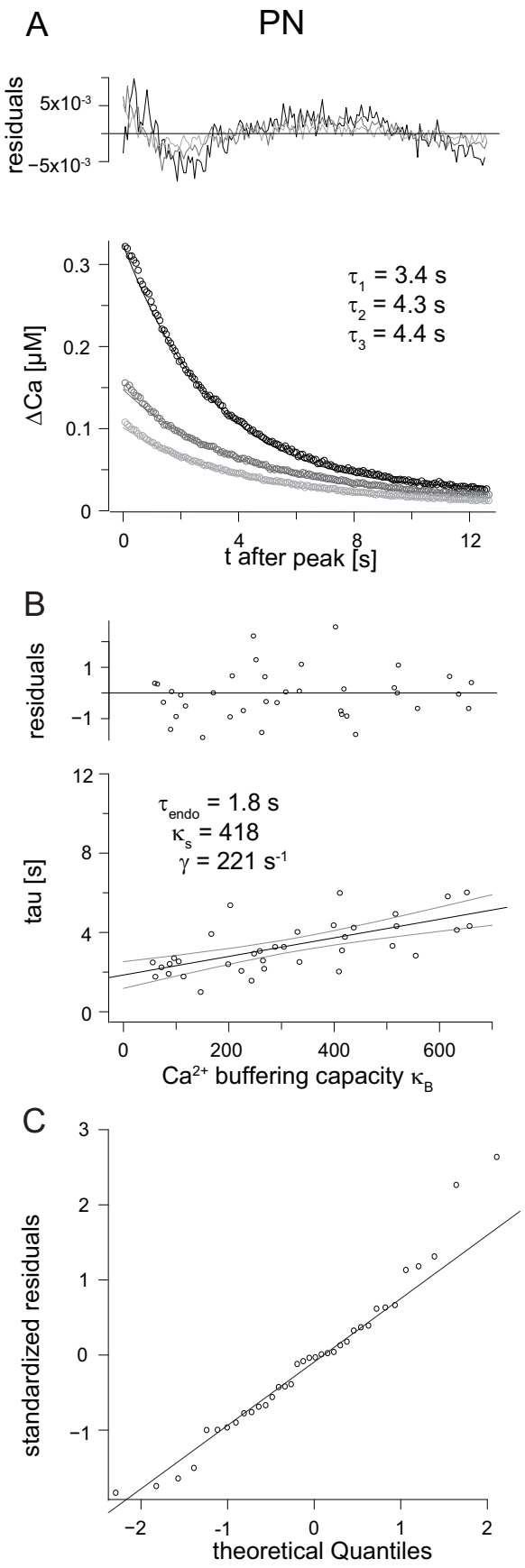

Figure 12: Analysis of Ca^{2+} buffering in projection neurons

*(**A**) Decay of Ca^{2+} after a short (50 ms) depolarization from -60 mV to 5 mV at increasing fura-2 concentrations in the cell. Black: 110 μM, red: 159 μM, green: 189 μM. Ca^{2+} transients were baseline-subtracted, which was acquired just before each stimulation. Transients were fit from peak to the end of signal with a single exponential function (solid lines, τ_1, τ_2, τ_3 as indicated in the figure). Residuals indicate that transients can be well approximated with monoexponentials, however a trend to a deviation from a monoexponential is noticable for large transients. (**B**) Decay constants of Ca^{2+} transients as determined in (A) were plotted against Ca^{2+} buffering capacity κ_B, which is calculated from the concentration of fura-2 in the cell, the K_d of fura-2 and the baseline Ca^{2+} concentration (see Methods). The data was fit with a linear function, which is used to extrapolate the endogenous decay constant τ_{endo} = 1.8±0.3 s (y-axis intercept), the endogenous Ca^{2+} binding ratio κ_S = 418±152 (negative x-axis intercept) and the extrusion rate γ = 221±44 s^{-1} (slope). Dotted lines indicate 90% confidence bands. (**C**) Normal Q-Q plot of the linear model and the data points in (B). The distribution falls close to a straight line, which shows that the data can well be discribed by a linear function.*

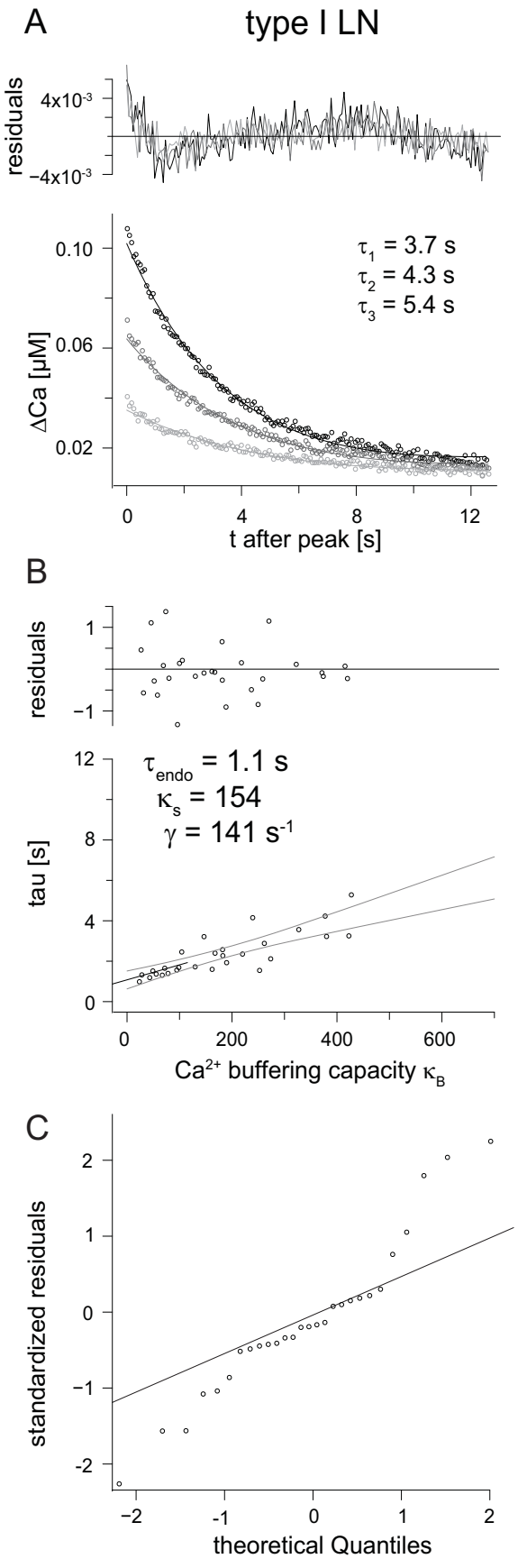

Figure 13: Analysis of Ca^{2+} buffering in type I interneurons

*(**A**) Decay of Ca^{2+} after a short (50 ms) depolarization from -60 mV to 5 mV at increasing fura-2 concentrations in the cell. Black: 107 μM, red: 144 μM, green: 195 μM. Ca^{2+} transients were baseline-subtracted, which was acquired just before each stimulation. Transients were fit from peak to the end of signal with a single exponential function (solid lines, τ_1, τ_2, τ_3 as indicated in the figure). Residuals indicate that transients can be well approximated with monoexponentials, however a trend to a deviation from a monoexponential is noticable for large transients. (**B**) Decay constants of Ca^{2+} transients as determined in (A) were plotted against Ca^{2+} buffering capacity κ_B, which is calculated from the concentration of fura-2 in the cell, the K_d of fura-2 and the baseline Ca^{2+} concentration (see Methods). The data was fit with a linear function, which is used to extrapolate the endogenous decay constant τ_{endo} = 1.1±0.2 s (y-axis intercept), the endogenous Ca^{2+} binding ratio κ_S = 154±49 (negative x-axis intercept) and the extrusion rate γ = 141±19 s^{-1} (slope). Dotted lines indicate 90% confidence bands. (**C**) Normal Q-Q plot of the linear model and the data points in (B). The distribution falls close to a straight line in the center, which is sufficient to assume that the data can well be discribed by a linear function.*

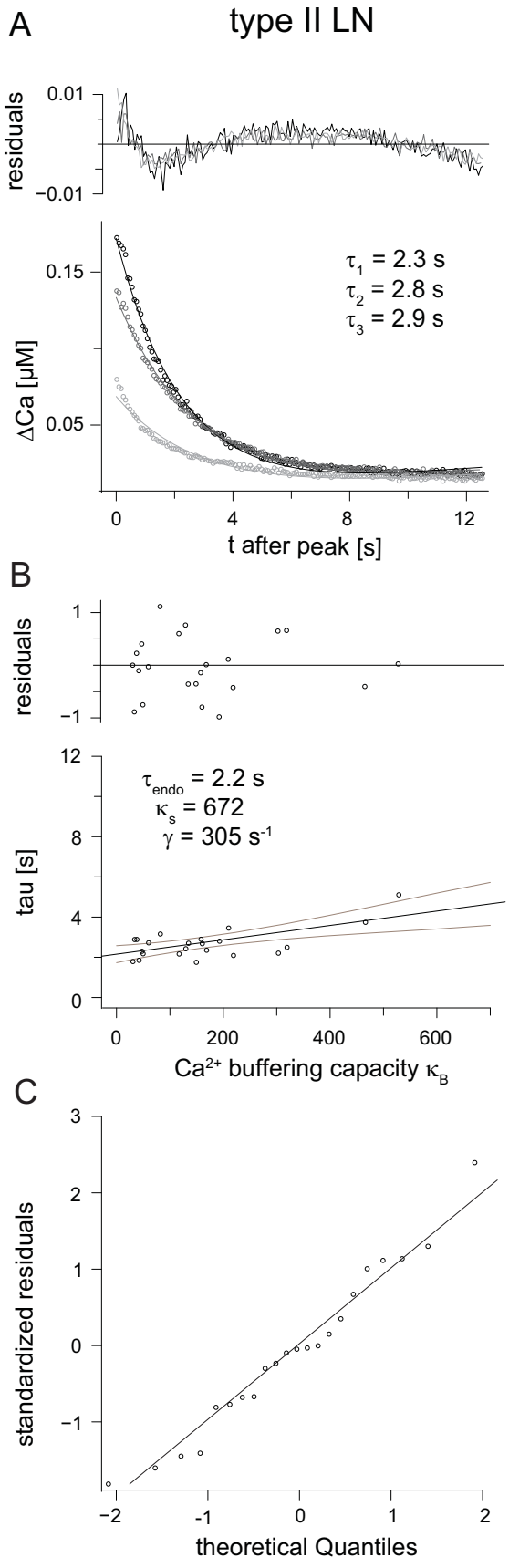

Figure 14: Analysis of Ca^{2+} buffering in type II interneurons

*(**A**) Decay of Ca^{2+} after a short (50 ms) depolarization from -60 mV to 5 mV at increasing fura-2 concentrations in the cell. Black: 46 μM, red: 64 μM, green: 89 μM. Ca^{2+} transients were baseline-subtracted, which was acquired just before each stimulation. Transients were fit from peak to the end of signal with a single exponential function (solid lines, τ_1, τ_2, τ_3 as indicated in the figure). Residuals indicate that transients can be well approximated with monoexponentials, however a trend to a deviation from a monoexponential is noticable for large transients. (**B**) Decay constants of Ca^{2+} transients as determined in (A) were plotted against Ca^{2+} buffering capacity κ_B, which is calculated from the concentration of fura-2 in the cell, the K_d of fura-2 and the baseline Ca^{2+} concentration (see Methods). The data was fit with a linear function, which is used to extrapolate the endogenous decay constant τ_{endo} = 2.2±0.2 s (y-axis intercept), the endogenous Ca^{2+} binding ratio κ_S = 672±280 (negative x-axis intercept) and the extrusion rate γ = 305±101 s^{-1} (slope). Dotted lines indicate 90% confidence bands. (**C**) Normal Q-Q plot of the linear model and the data points in (B). The distribution falls close to a straight line, which shows that the data can well be discribed by a linear function.*

3.2.4 Comparison of neuron types

In this study Ca^{2+} buffering properties from uPNs, type I and type II LNs were compared. The parameters related to Ca^{2+} buffering were obtained from each cell type with a linear regression to the data of time constants of transients over κ_B. From these regressions the y-axis intercepts (denote τ_{endo}), the slopes (denote γ) and the negative x-axis intercepts (denote κ_S) had to be extrapolated. These extrapolated values were then compared between different cell types. However, extrapolating meaningful values from linear regressions is not trivial, because the actual data points usually scatter more or less around the regression lines, thereby introducing statistical variation on the extrapolated parameters. Before comparing the parameters of uPNs, type I and type II LNs, I therefore first checked if the linear regression lines sufficiently described the data of the three cell types. This was done with normal-Q-Q plots (see Fig. 12-14 C. Second, I determined the variability of every extrapolated parameter with the bootstrap method, resulting in distributions of τ_{endo}, γ, and κ_S for the three cell types (Fig. 15). These distributions were then log-transformed so that they became gaussian and could then statistically be compared with Student's pairwise t-test. The distributions of the three parameters were significantly different from each other in all cell types by the highest significance value ($p < 0.001$).

The results of all parameters determined in this study are summarized in Fig. 15 and table 1

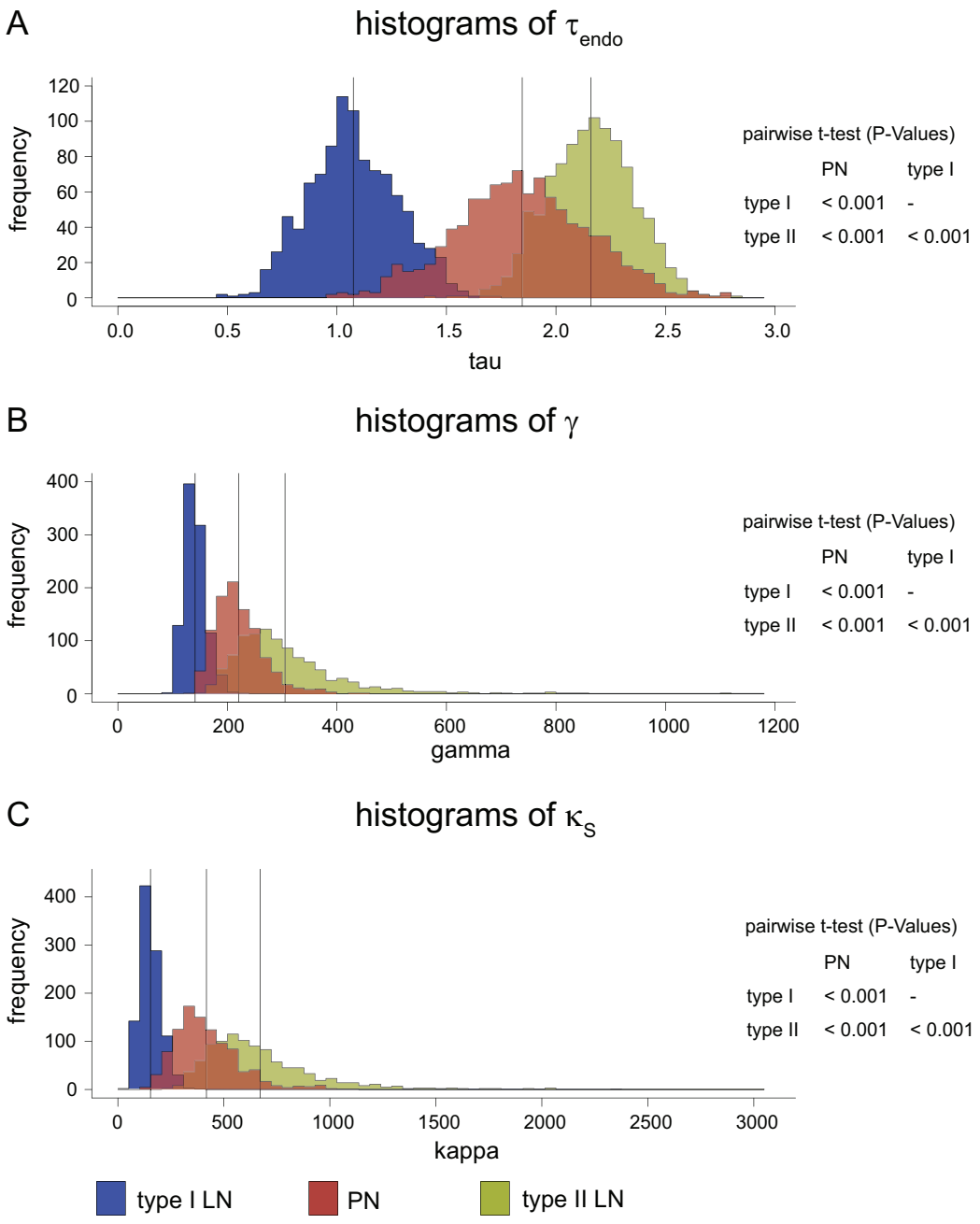

Figure 15: Bootstrap analysis of buffering related parameters

*From the linear fit of $\tau_{transient}$ against κ_B (figures 12-14) 1000 bootstrap samples were taken, which resulted in the shown distributions of the y-axis intercept (τ_{endo}), the slope (γ) and the negative x-axis intercept (κ_S) from uPNs, type I and type II LNs. The frequency with which a certain value of τ_{endo}, γ or κ_S occurs in this distribution reflects its probability to be the 'true' τ_{endo}, γ or κ_S. The vertical lines depict the mean. (**A**) Histograms of τ_{endo} for uPNs, type I and type II LNs. (**B**) Histograms of γ for uPNs, type I and type II LNs. (**C**) Histograms of κ_S for uPNs, type I and type II LNs. The distributions for each parameter were log-transformed for statistical analysis. For pairwise comparisons of cell types, Student's pairwise t-tests were used to assess statistical significance. Significances were accepted at $P < 0.001$*

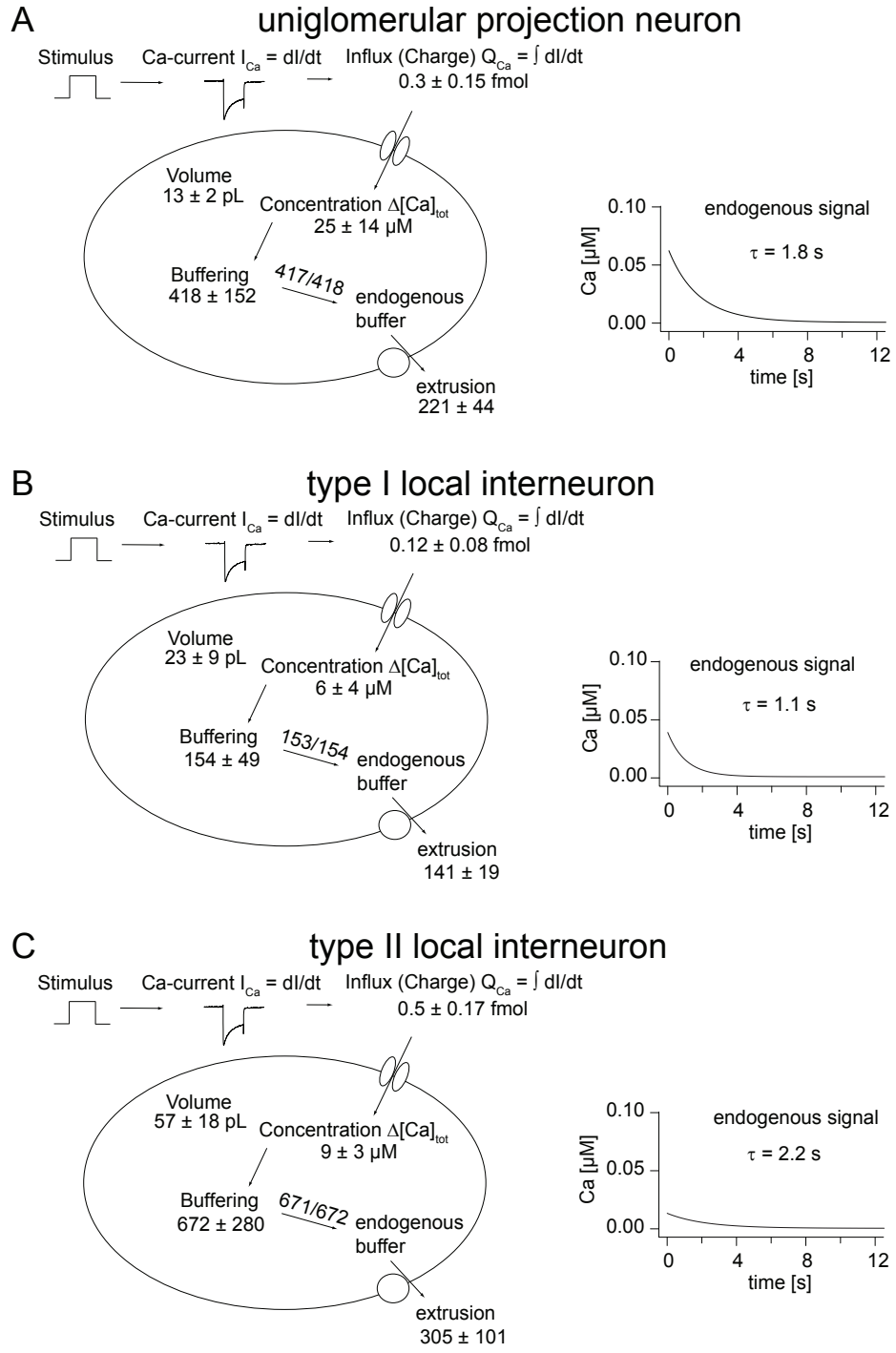

Figure 16: Scheme of Ca^{2+} dynamics in uPNs, type I and type II LNs

*Schematic drawing of the Ca^{2+} dynamics in the cell bodies of uniglomerular projection neurons (**A**), type I local interneurons (**B**) and type II local interneurons (**C**) from the antennal lobe of P. americana as obtained with the single compartment model. Ca^{2+} influx was elicited by voltage steps from -60 to 5 mV, all non Ca^{2+} currents were blocked, so that current traces could be integrated to obtain absolute values of Ca^{2+} influx.*

Table 1: Summary of buffering related parameters

	in Vitro	PN	Type I LN	Type II LN
charge nCa [fmol]	0.22±0.05	0.30±0.15	0.12±0.08	0.50±0.17
volume V [pL]	17±6	13±2	23±9	57±18
conc. $\Delta[Ca^{2+}]_{tot}$ [μM]	14±5	25±14	6±4	9±3
resting $[Ca^{2+}]_{i,\infty}$ [μM]	0.212±0.216	0.048±0.039	0.174±0.09	0.117±0.053
extrusion γ [s^{-1}]	84± 29	221±44	141±19	305±101
endo τ [s]	3.7±0.5	1.8±0.3	1.1±0.2	2.2±0.2
endo buffer κ_S	317±144	418±152	154± 49	672±280
n	20	11	10	8

values are means ± SD

3.2.5 Outlook – differential buffering in small neuronal compartments of single cells

The previous analyses of internal Ca^{2+} dynamics were based on the linearized model of Neher and Augustine (Eq. 13). Assumptions underlying this linearization were constant baselines of the recorded Ca^{2+} signals, constant exogenous buffer while the transients were recorded and small signals with respect to the K_d of the exogenous buffer (i.e. smaller than 0.5 times K_d). Under these conditions time constants of endogenous Ca^{2+} signals could be recorded at defined exogenous buffer concentrations. The best way to control the concentration of the exogenous buffer with patch-clamp recordings was by obtaining loading curves (see also chapter 3.2.2).

To quantitatively analyze Ca^{2+} influx, Ca^{2+} binding ratio and extrusion rate at the same time in individual glomeruli and cell bodies of single uPNs, I first checked if the same conditions could be fulfilled in both compartments of the same uPN. Fig. 17 illustrates the feasibility of obtaining loading curves from the cell body and the glomerulus of a uPN in the same experiment. The neuron was filled with 800 μM fura-2. Fluorescence was first monitored over time in the cell body until it reached saturation after ~25 min. A short depolarizing current injection from 0 to 700 pA for 500 ms elicited a Ca^{2+} influx that was nicely described by a monoexponential fit. The experiment was continued when fluorescence in the glomerulus was

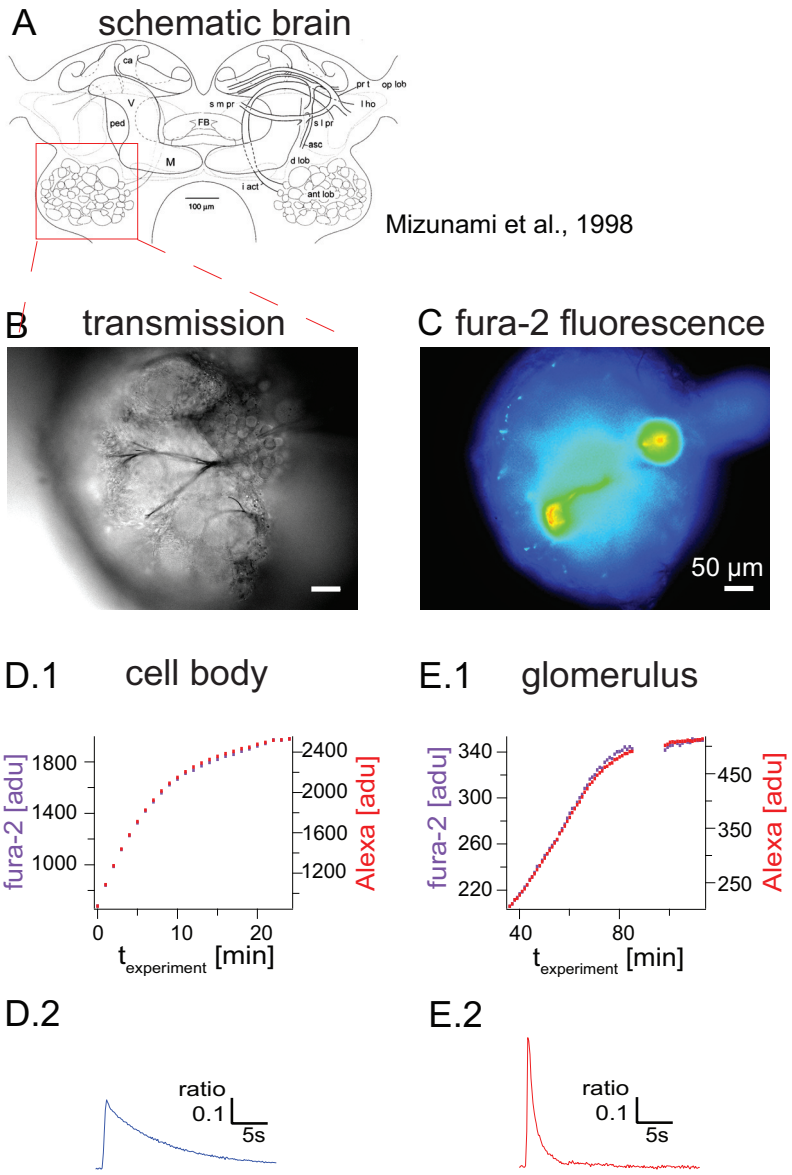

Figure 17: Loading curve and Ca^{2+} signals in small neuronal comparments of uPNs
*(**A**) Schematic brain indicates regions where recorded neurons are located (from Mizunami et al., 1998). (**B**) Bright field image of the antennal lobe taken in on-cell mode. The cell cluster around the pipette tip represents projection projection neurons. (**C**) Projection neurons were patch-clamped with 800 µM fura-2 and 0.05 % Alexa 568. Images were taken with a CCD camera (bright field and fluorescence). This technique is used to quantify calcium signals in the cell body and glomerulus simultaneously. (**D. 1**) Dye concentration was monitored in the cell body immediately after break-in. When fluorescence had reached saturation short depolarizing currents were injected to evoke a train of action potentials, which elicited a Ca^{2+} signal (**D.2**). (**E.1**) When fluorescence was detectable in the glomerulus, dye concentration was monitored until saturation. The same stimulus as in D.2 was used to elicit Ca^{2+} influx in the glomerulus (**E.2**). Different Ca^{2+} kinetics in cell body and glomerulus indicate different calcium dynamics in these two compartments.*

detectable, which was then monitored until it reached a stable value. When the plateau was reached, the same depolarizing current was shortly injected (from 0 to 700 pA for 500 ms) to elicit a Ca^{2+} influx, which was two times larger in the glomerulus than in the cell body and which could nicely be described by a biexponential fit.

The kinetics from the cell body (Fig. 17D.2) and from the glomerulus (Fig. 17E.2) were both obtained at the same fura-2 concentration (800 μM) and were elicited with the same stimulus (current injection from 0 to 700 pA for 500 ms). However they differed in amplitude and time course, which indicates that the Ca^{2+} handling properties are fundamentally different in the two compartments.

3.3 Imaging of odor evoked calcium signals

The main question in this study was, if there are glomerulus specific odor responses in local interneurons. The answer is yes and no. I have examined glomerular odor responses in different types of LNs with arborizations in many or all glomeruli. In the following I first present LNs that do have glomerulus specific odor responses and then the ones with uniform unspecific responses.

Using Ca^{2+} imaging in combination with electrophysiological recordings, odor stimulation and subsequent morphological analysis, relative odor responses were analyzed in physiologically and morphologically different neuron types in the antennal lobe of *Periplaneta americana*. Odor responses were recorded from individual glomeruli of single neurons. To quantify differences of glomerular responses tuning curves for each glomerulus were obtained (Fig. 18, 20, 21 and 22D). This was done by measuring the relative fluorescence changes from baseline to peak in each glomerulus for each odor. These were then normalized to the maximum response elicited in that glomerulus across the number of tested odors.

Following the method of Loehle and Rittenhouse (1982), a response was supposed to not be significantly different from the maximum, when its amplitude was 50 % or more of the maximum. Responses of less than 50 % of the maximum were supposed to be significantly different from the maximum Tuning curves of individual glomeruli were obtained to compare odor specific responses in different glomeruli of the same neuron. Odor evoked activity in six glomeruli in response to a maximum of 6 odors plus a blank control were recorded. Stimuli were always plotted in the same order for each glomerulus (Fig. 18, 20, 21 and 22D).

Neurons were held in whole-cell current clamp configuration at slightly negative holding currents (~-200 pA) for about 45 min. to allow for diffusion of the Ca^{2+} indicator into glomeruli. During this loading procedure depolarizing current injection and voltage-clamp steady state activation protocols were applied to identify the neurons. When fluorescence of the Ca^{2+} indicator was well detectable in the glomeruli (usually after 45 - 60 min.), up to 6 single component odors were puffed onto the ipsilateral antenna for 500 ms each (α-ionone, +/- citral, citronellal, geraniol, hexanol, eugenol). Fluorescence of the Ca^{2+} indicator in the glomeruli was measured with a CCD imaging system. The odor induced change of Ca^{2+} was then evaluated over time from regions of interest as depicted in Fig. 18, 20, 21 and 22D.

Two categories of glomerular response profiles have been identified: gomerulus specific odor responses and uniform unspecific odor responses. These categories were provided by qualitatively different glomerulus specific tuning curves of individual LNs. The two categories are covered subsequently. After that a typical response of a uPN is shown as a reference.

3.3.1 LNs with glomerulus specific odor responses

In the following I show three examples of LNs that display glomerulus specific odor responses. The first example is from a type I LN, the second from a yet unidentified and the third from a type II LN.

Fig. 18 shows a type I LN that responded to the presented odors glomerulus specifically. The neuron responded to all odors tested. All odors elicited a single action potential and one peak in the glomerular reaction. However, not all glomeruli responded to all odors in the same way. Fig. 18C shows that α-ionone and citral elicited strong reactions in glomeruli 14 and 15 ($\Delta F/F$ was1.4 % and 1.5 % in glomerulus 15 for α-ionone and citral; $\Delta F/F$ was 1.6 % and 1.6 % in glomerulus 14 for α-ionone and citral), whereas glomeruli 22 and 23 remained almost silent (between 0.3 and 0.5 %). In contrast, geraniol and hexanol elicited strong absolute fluorescence changes in all glomeruli ($\Delta F/F$ was 2.5 % and 2.1 % in glomerulus 15 for geraniol and hexanol; $\Delta F/F$ was 2.3 % and 2.6 % in glomerulus 14 for geraniol and hexanol; $\Delta F/F$ between 1.6 % and 2.1 % in glomeruli 22 and 23). The relative amplitudes to different odors varied among glomeruli as obvious from the tuning curves. This analysis demonstrated that some glomeruli were activated particularly strong by some odors and weak by others (e.g. glomerulus 22, Fig. 18D). Other glomeruli were activated more uniformly (eg. glomerulus 3, 14 and 15). The odors producing the highest Ca^{2+} influx were either geraniol or hexanol. The tuning curves were equivalent for glomeruli 3 and 14, for 15 and 18 and for 22 and 23. The localized activity suggests that the neuron differentially integrates odor information.

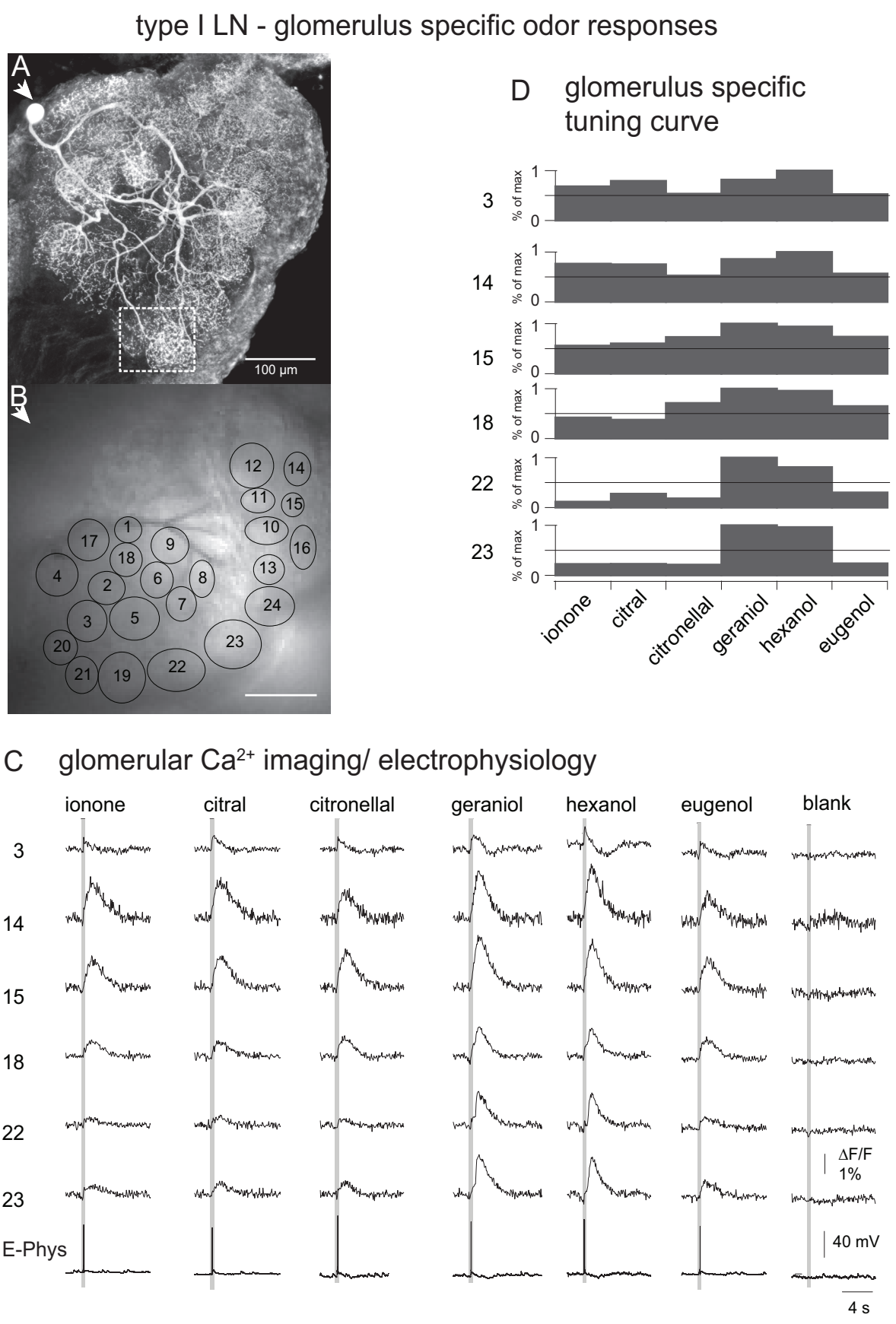
type I LN - glomerulus specific odor responses
A
100 µm
B
12
14
11
15
10
16
1
17
9
18
13
4
2
6
8
7
24
3
5
23
20
21
19
22
D
glomerulus specific
tuning curve
3
14
15
18
22
23
% of max
1
0
ionone
citral
citronellal
geraniol
hexanol
eugenol
C
glomerular Ca2+ imaging/ electrophysiology
ionone
citral
citronellal
geraniol
hexanol
eugenol
blank
3
14
15
18
22
23
E-Phys
ΔF/F
1%
40 mV
4 s

*(**A**) Morphology of a type I LN stained with streptavidin-Alexa 633 from a wholemount preparation. Standard deviation Z-projection of a confocal LSM image stack. White arrohead depicts cell body. Multiple, but not all glomeruli were innervated with interglomerular different densities (see dashed box). A thick dendritic tree spreads from the cell body to the center of the antennal lobe, then dividing into small branches innervating glomeruli. (**B**) Transmission image of the same LN while the neuron was recorded. Orientation as in (A). White arrowhead depicts position of the cell body and patch-pipette. In the transmission image glomeruli could be spotted and marked as regions of interest (solid circles, numbers correspond to glomerular responses shown in (C)). Glomeruli could not be unequivocally identified from one recording to the next. (**C**) Odor evoked Ca^{2+} influx in representative regions shown in (B) and corresponding electrophysiological responses. All odors elicited a similar electrophysiological response, but different glomerular responses. Note that glomeruli 14 and 15 responded to all odors with high amplitudes, whereas glomeruli 22 and 23 differentially respond to geraniol and hexanol, but not to the other odors. Odors were puffed onto the ipsilateral antenna for 500 ms. (**D**) Tuning curves of glomerular responses. Relative fluorescence changes from baseline to peak were measured in each glomerulus for each odor. These were then normalized to the maximum response elicited in that glomerulus across the six tested odors. Activities were significantly different from the maximum when they were below 50 % of the maximum (horizontal black line). Glomeruli 3, 14 and 15 responded uniformly to all odors. Glomeruli 18, 22 and 23 specifically responded to few odors.*

The second example of a LN with glomerulus specific odor responses is shown in Fig. 20. The neuron reacted to all odors tested, but with elaborate electrophysiological responses specific for each odor (Fig. 19). All excitatory responses were followed by a hyperpolarization. The glomerular responses all had a single peak. However, not all glomeruli reacted in the same way. Fig. 20C shows that glomerulus 13 responded strongly to all odors ($\Delta F/F$ from 0.4 % (α-ionone) to 1.3 % (citronellal). In contrast glomerulus 15 responded weakly to all odors ($\Delta F/F$ from 0 % (eugenol) to 0.6 % (hexanol). In addition to heterogeneous absolute amplitudes, also the relative amplitudes varied. The tuning curves (Fig. 20D) demonstrated, that some glomeruli were activated uniformly (e.g. 4 and 7), where the activity was always above 50 % of the maximum response. Others were strongly activated by some odors and weakly by others (e.g. 13, 14 and 16). In these glomeruli two of the six presented odors elicited responses that were significantly less than the maximum response. Glomerulus 15 was of an intermediate type with an activity well above 50 % of the maximum for all odors

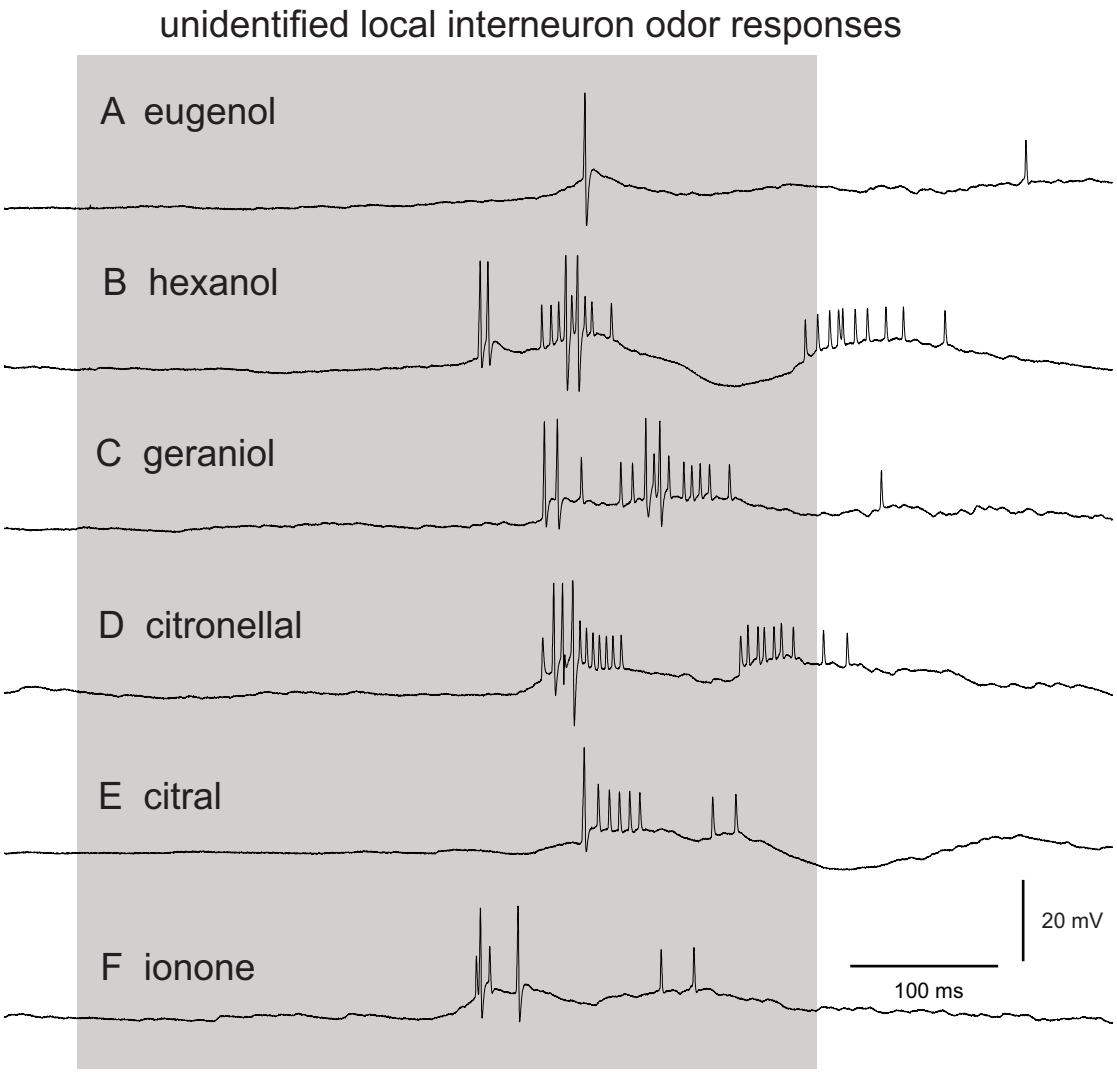

Figure 19: Electrophysiological responses to different odors of a yet unidentified LN
Detailed electrophysiological odor responses of the neuron shown in figure 20 from whole cell patch-clamp recordings. 6 odors were puffed onto the ipsilateral antenna for 500 ms (grey box). For blank control see figure 20. Odor responses were heterogenous for the 6 applied odors (A-F). There was always at least one long lasting depolarization with spikes of different amplitudes riding on top. Different spike amplitudes indicate multiple spike-generating zones.

except eugenol. The heterogeneous electrophysiological responses thus correlated with the glomerulus specific Ca^{2+} influxes. The results suggest that this neuron is generally active upon odor stimulation, with several spike generation zones and subdivisions of high and low activity for certain odors.

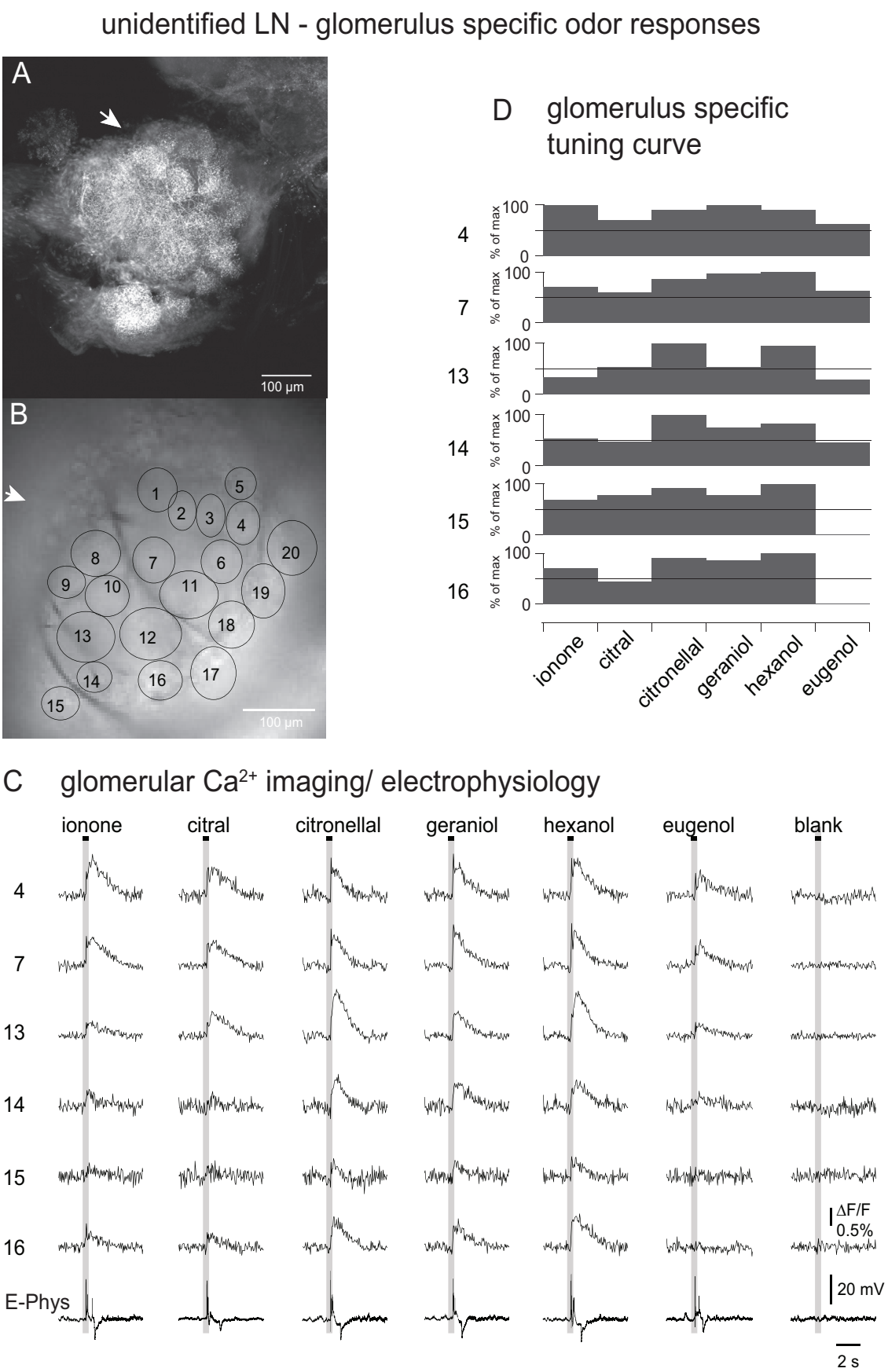
unidentified LN - glomerulus specific odor responses
A
100 µm
B
1
2
3
4
5
6
7
8
9
10
11
12
13
14
15
16
17
18
19
20
100 µm
D glomerulus specific tuning curve
4
7
13
14
15
16
% of max
100
0
ionone
citral
citronellal
geraniol
hexanol
eugenol
C glomerular Ca2+ imaging/ electrophysiology
ionone
citral
citronellal
geraniol
hexanol
eugenol
blank
4
7
13
14
15
16
E-Phys
ΔF/F
0.5%
20 mV
2 s

Figure 20: Ca^{2+} imaging in an unidentified LN with glomerulus specific odor responses
*(**A**) Morphology of an unidentified LN. The cell body was lost during processing (white arrowhead). Multiple glomeruli were similarly dense innervated, but not all. Arborizations were finer than in type I or type II LNs. (**B**) Transmission image from the same LN during recording. Orientation as in (A). White arrow depicts position of the cell body and patch-pipette. Solid circles depict glomeruli. (**C**) Odor evoked Ca^{2+} influx in representative regions shown in (B) and corresponding electrophysiological responses. All odors elicited electrophysiological responses, but fluorescence changes were only elicited in some glomeruli. Note that glomeruli 4, 7 and 13 responded to all odors, whereas glomeruli 15 and 16 responded to all odors except eugenol. Odors were puffed onto the ipsilateral antenna for 500 ms. (**D**) Tuning curves of glomerular responses. Glomeruli 4 and 7 responded always with more than 50 % of the maximum. Glomeruli 13, 14 and 16 responded with more than 50 % of the maximum to four odors and with less to two odors. Glomerulus 15 was uniformly activated with 5 odors and not activated with one. For details see legend of figure 18.*

The previous two examples were form LNs with glomerulus specific odor responses. The third example is from a LN, which responds to one odor glomerulus specifically, but uniformly to all the other odors (Fig. 21). All odors elicited a small depolarization with a spikelet between 15 mV (α-ionone) and 21 mV (citral). The electrophysiological responses were almost identical for the different odors and well correlated with the glomerular activities, which all had one peak. Yet, the absolute amplitudes of glomerular activities differed considerably (glomerulus 1: $\Delta F/F = 2.6$ % for citral and $\Delta F/F = 1.5$ % for hexanol; glomerulus 7: $\Delta F/F = 1.1$ % for citral and $\Delta F/F = 0.6$ % for hexanol; glomerulus 15: $\Delta F/F = 2.7$ % for citral and $\Delta F/F = 1.2$ % for hexanol). Relative amplitudes however were not significantly different from each other except for three cases (hexanol stimulation in glomeruli 7, 13 and 15). The tuning curves demonstrated that all glomeruli were activated strongly for all odors except hexanol in the case of glomeruli 7, 13 and 15. Except for hexanol in the three mentioned cases, the activity was always well above 50% of the maximum. This means that glomeruli 1, 3 and 10 were equivalently broadly tuned and glomeruli 7, 13 and 15 were also broadly tuned with a specific reaction to hexanol. Compared to the previous two examples of LNs with glomerulus specific odor responses, this type II LN was less specifically tuned.

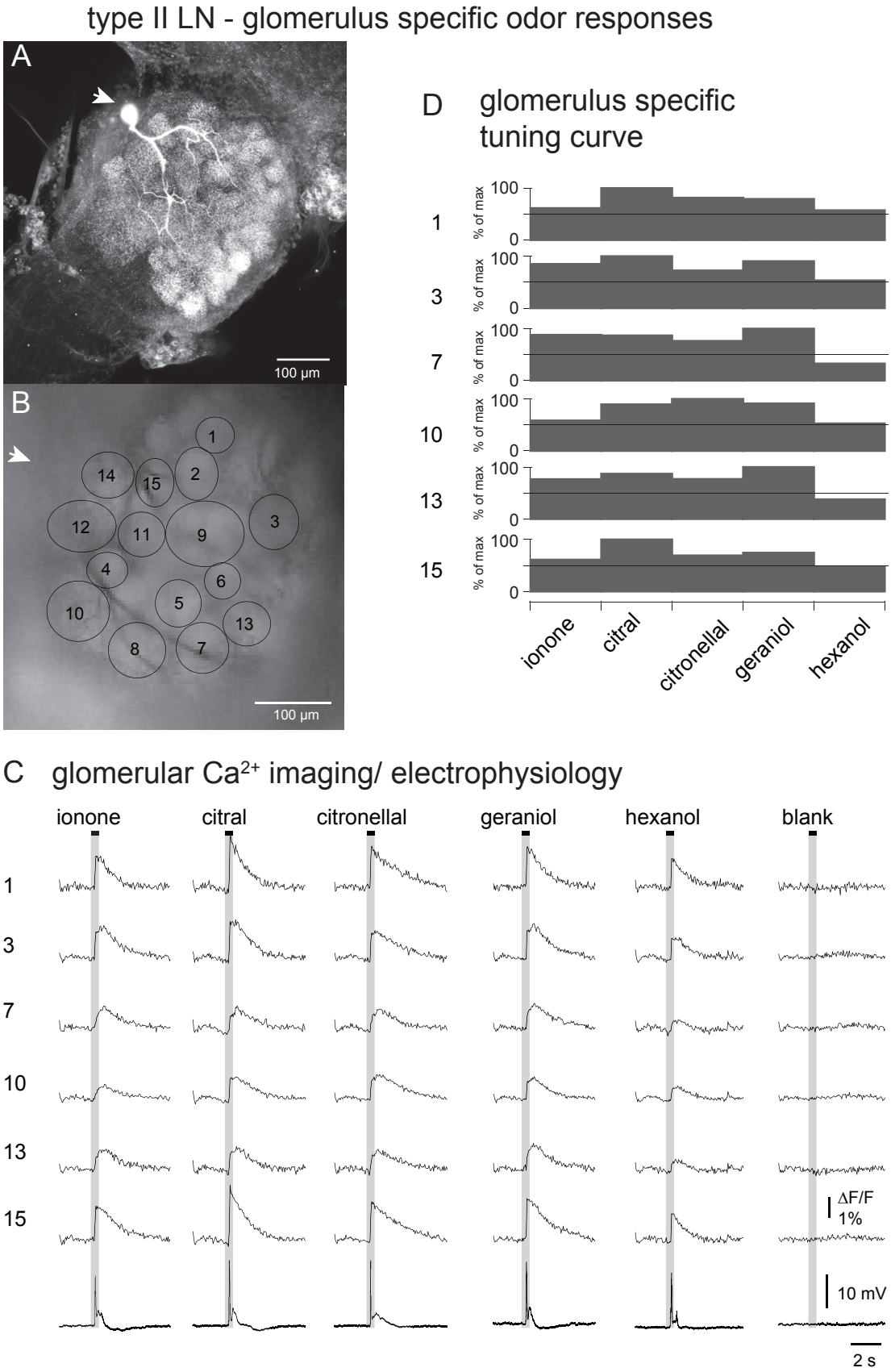
type II LN - glomerulus specific odor responses
A
100 µm
B
1
2
3
4
5
6
7
8
9
10
11
12
13
14
15
100 µm
D
glomerulus specific
tuning curve
1
3
7
10
13
15
% of max
100
0
ionone
citral
citronellal
geraniol
hexanol
C
glomerular Ca2+ imaging/ electrophysiology
ionone
citral
citronellal
geraniol
hexanol
blank
1
3
7
10
13
15
ΔF/F
1%
10 mV
2 s

*(**A**) Morphology of a type II LN. White arrohead depicts cell body. All glomeruli were similarly innervated. (**B**) Transmission image of the same LN during recording. Orientation as in (A). White arrowhead depicts position of the cell body and patch-pipette. Solid circles depict glomeruli. (**C**) Odor evoked Ca^{2+} influx in representative regions shown in (B) and corresponding electrophysiological responses. All odors elicited similar electrophysiological and similar but not identical glomerular responses. Absolute amplitudes of glomerular responses differed considerably (e.g. $\Delta F/F = 0.6$ % for hexanol in glomerulus 7 and 2.7 % for citral in glomerulus 15). (**D**) Tuning curves of glomerular responses. Relative amplitudes were similar for all glomeruli and always above the 50 % significance level except in three cases (hexanol in glomeruli 7,13 and 15). For details see legend of figure 18.*

3.3.2 LNs with uniform glomerular odor responses

In the following I show an example of a type I LN that displays uniform glomerular odor responses (Fig. 22). Two neurons have been recorded, both reacting like the one shown in Fig. 22. Unlike uPNs, this neuron reacted to all odors tested (α-ionone, citronellal, geraniol, hexanol). The patterns were similar for the different odors, but not identical. All odors elicited one (hexanol) to few (citronellal and geraniol) action potentials, which were well correlated with the glomerular responses. Action potentials shortly following one after the other were represented by a summation of the answer in the glomeruli, lower frequencies were represented by autonomous peaks.

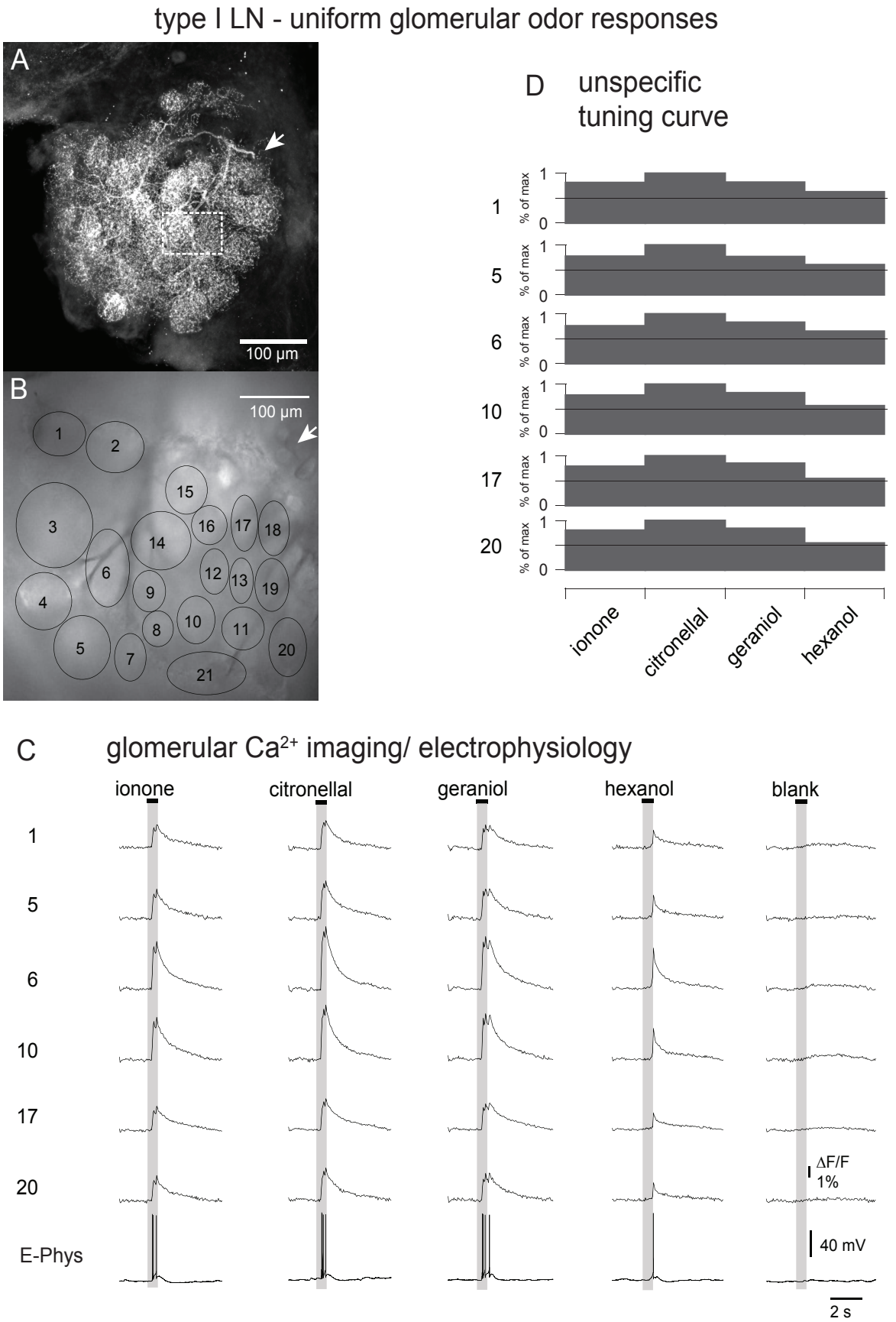
type I LN - uniform glomerular odor responses
A
100 µm
B
100 µm
1
2
3
4
5
6
7
8
9
10
11
12
13
14
15
16
17
18
19
20
21
D
unspecific
tuning curve
% of max
1
0
1
5
6
10
17
20
ionone
citronellal
geraniol
hexanol
C
glomerular Ca2+ imaging/ electrophysiology
ionone
citronellal
geraniol
hexanol
blank
1
5
6
10
17
20
E-Phys
ΔF/F
1%
40 mV
2 s

Figure 22: Ca^{2+} imaging in a type I LN with uniform glomerular odor responses
*(**A**) Morphology of a typ I LN. The cell body was lost during processing (white arrowhead). Multiple, but not all glomeruli were innervated with interglomerular different densities (see dashed box). (**B**) Transmission image of the same LN. Orientation as in (A). White arrowhead depicts position of the cell body and patch-pipette. Solid circles depict glomeruli. (**C**) Odor evoked Ca^{2+} influx in representative regions shown in (B) and corresponding electrophysiological responses. All odors elicited reactions in all glomeruli. Note that all glomeruli responded to the same odor with similar amplitudes and kinetics. There were little qualitative differences between the odors. Odors were puffed onto the ipsilateral antenna for 500 ms. (**D**) Tuning curves of glomerular responses. Highest response was always from citronellal, lowest from hexanol. All responses were well above the 50 % significance level, there were no specific responses to any odor. For details see legend of figure 18.*

The relative changes in fluorescence in the glomeruli were between ~1.5 % (glomerulus 17, hexanol) and ~5.5 % (glomerulus 6, citronellal). All glomeruli responded to the same odor with comparable relative fluorescence changes and with comparable kinetics (e.g. decay constants for citronellal ranged between 0.8 and 1.2 s).

Accordingly, tuning curves were equivalent for all glomeruli. All glomeruli were activated uniformly for identical odors. The odor producing the highest Ca^{2+} influx was always citronellal. The lowest influx was always elicited with hexanol. There was no compartmentalization detectable, the whole neuron reacted upon odor stimulation with one collective answer. There were little qualitative differences between the different odors. This neuron reacted to the odors presented with different levels of excitation, but always uniformly across the whole antennal lobe. However, all activities were above 50 % of the maximum and therefore not significantly different from each other.

3.3.3 Uniglomerular projection neurons

Fig. 23 shows an odor evoked Ca^{2+} signal in the glomerulus of a uPN. The projection neuron reacted to geraniol with a train of 11 action potentials and a large, transient Ca^{2+} influx ($\Delta F/F = 100\%$) in the glomerulus. Citronellal elicited only three action potentials followed by a small hyperpolarization. In the

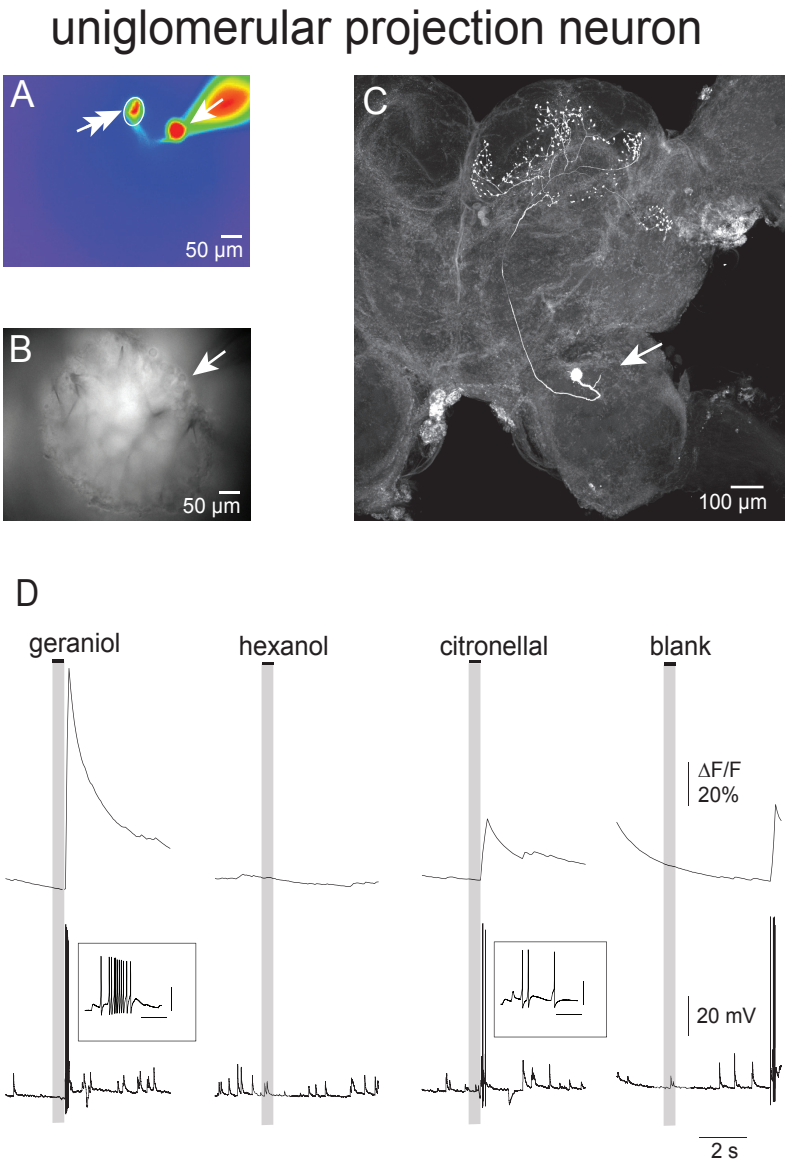

Figure 23: Odor evoked Ca^{2+} signals in subcellular compartments of a PN
*(**A**) Fluorescence image of a PN filled with 600 µM OGB-1. Arrow depicts cell body and position of the patch-pipette. Double arrow points to glomerulus, which was well resolved and marked with a region of interest (ROI) to evaluate Ca^{2+} kinetics during odor stimulation. (**B**) Transmission image of the recorded antennal lobe. Same view as in (A). Arrow depicts cell body and position of the patch-pipette. (**C**) Morphology of the same PN stained with streptavidin-Alexa 633 from a wholemount preparation. Standard deviation Z-projection of a confocal LSM image stack. Orientation as in (A). Arrow depicts position of cell body, which was lost during processing. (**D**) Odor evoked Ca^{2+} responses from a ROI centered over the glomerulus as shown in (A) and the corresponding electrophysiological responses from the patch-pipette. Fluorescence changes are represented as relative changes in percent. Odors were puffed onto the ipsilateral antenna for 500 ms. Insets show details of the electrophysiological responses. Scale bars insets: 40 mV, 100 ms.*

glomerulus a smaller transient Ca^{2+} influx ($\Delta F/F \approx 30\%$) was detected. Hexanol and pure mineral oil did not elicit any responses. In general the activities in the glomerulus and the cell body were correlated such that the number of action potentials in the cell body were mirrored in the glomerular Ca^{2+} influx.

This recording illustrates that the odors in the used concentrations stimulated olfactory receptors specifically and that they did not elicit global unspecific responses.

4 Discussion

In the first part of this study I used patch-clamp recordings and fast optical imaging in combination with the 'added buffer approach' to analyze cellular parameters that determine the dynamics of internal calcium signals. Recordings were performed in adult *Periplaneta americana* from two unequivocally identified types of local interneurons and from uniglomerular projection neurons. In the second part of this study I used patch-clamp recordings, fast optical imaging and physiological odor stimulation to measure odor evoked activity in subcellular compartments of the same identified neuron types.

4.1 Identification of neuron types

Neurons were categorized as previously proposed by Husch (2007) by a combination of physiological and morphological properties, including intrinsic firing characteristics, innervation pattern of glomeruli and calcium currents.
In the first part of this study all currents were blocked that were not carried by calcium. The physiological differences regarding spike generation could thus not be used for identification. Neuronal tracers were not used, because it was not clear whether they would affect the calcium buffering. Therefore neurons could not be identified by their morphological properties. Instead they were unequivocally distinguished by their calcium current properties and their specific current-voltage

relations (Husch, 2007). Fig. 6 illustrates that this procedure was very reliable, because IV relations from this study perfectly matched those of Husch (2007).
In the second part of this study, odor evoked glomerular fluorescence signals were analyzed. All recordings were performed in unblocked conditions so that differences in spiking behavior could be assessed. Furthermore, potential effects of neuronal tracers on Ca^{2+} buffering were neglected, so that neurons could be morphologically analyzed. Thus, the well known uniglomerular projection neurons could easily be identified by their projections to the protocerebrum (Malun, 1991a; Malun, 1991b; Malun et al., 1993). Type I interneurons were classified as such, when they produced action potentials and innervated multiple but not all glomeruli with interglomerular differences (Husch, 2007). Type II interneurons had to lack action potentials and all glomeruli had to be innervated (Husch, 2007). A new type of local interneurons was found that produced action potentials, however not in the cell body and innervated multiple glomeruli without interglomerular differences (Fig. 20).
In both parts of the study, neuron types could reliably be identified, either by specific properties of their calcium currents or by a combination of physiological and morphological properties. The two parts of this study about calcium buffering properties and odor responses are subsequently discussed independently.

4.2 Calcium Buffering

Patch-clamp recordings and fast optical imaging in combination with the 'added buffer approach' were used to analyze cellular parameters that determine the dynamics of internal calcium signaling in central olfactory neurons of *Periplaneta americana*. Two physiologically different local interneuron types were compared and the well known projection neurons served as a reference. Type I LNs generate

Na^+ driven action potentials, whereas type II LNs do not possess voltage activated Na^+ channels and Ca^{2+} is the only cation that enters the cell to contribute to membrane depolarizations. These electrophysiological characteristics correlate with significantly different Ca^{2+} handling parameters.

The absolute Ca^{2+} influx, the Ca^{2+} binding ratio and the extrusion rate are highest in type II LNs. Because of the high Ca^{2+} binding ratio in type II LNs, the high amount of absolute Ca^{2+} is quickly buffered. This leads to the question of the physiological function of such high buffering? One possibility is that it provides a protective function preventing Ca^{2+} peaks to spread over the entire cell (von Lewinski and Keller, 2005) so that they remain locally restricted to the sources of the influx, which is necessary for signaling in functional compartments. This would support the view that these neurons are strongly dependent of Ca^{2+}. A second possibility is that prolonged dynamics have a physiological function to produce global signals of low amplitude and long duration. This would support the view that in these neurons, long lasting Ca^{2+} signals trigger specialized functions. To discriminate between these two possibilities further analyses of the Ca^{2+} binding ratio in smaller compartments of the neuropil close to Ca^{2+} sources are necessary. Type I LNs do not buffer as high amounts of Ca^{2+} as type II LNs, again suggesting two possible physiological functions. On the one hand this would implicate that they generate high amounts of free Ca^{2+} that do spread over the entire cell suggesting that these neurons are not dependent on localized signals like the type II LNs. On the other hand this could mean that fastened Ca^{2+} dynamics have a physiological function to produce cell wide Ca^{2+} signals of high amplitude and short duration.

Proposing a physiological function of Ca^{2+} buffering is relatively straight forward. Understanding the effects of Ca^{2+} influx and extrusion on the internal Ca^{2+} dynamics is not as trivial. To illustrate what the effects of the three individual

parameters are on Ca^{2+} dynamics, signals have been simulated (Fig. 24). Fig. 24A shows simulated endogenous Ca^{2+} signals of the studied neuron types (type I LN, type II LN and PNs as a reference). Reference values were always those of the PNs (black traces in Fig. 24). They have an intermediate Ca^{2+} binding ratio, extrusion rate and absolute Ca^{2+} influx compared to type I and type II LNs. But because of their small volume the increase of Ca^{2+} is significantly higher. From the calcium buffering related parameters these neurons represent an intermediate type, which is consistent with previous findings of Husch et al. (2008).

The highest absolute values for the endogenous Ca^{2+} binding ratio κ_S and the extrusion rate γ were found in type II LNs. In contrast, type I LNs had the lowest absolute values for κ_S, and γ. Ca^{2+} increase $\Delta[Ca^{2+}]_i$ was not significantly different. Fig. 24B illustrates the relevance of the individual parameters for the internal Ca^{2+} signal. In Fig. 24B.1 Ca^{2+} signals were simulated with identical parameters as in A, but with the same Ca^{2+} increase for all cell types. The effect of an identical Ca^{2+} increase in both type I and type II LNs becomes most evident from the different amplitudes of the peak endogenous free Ca^{2+} concentration, which is about 5 times higher in type I LNs than in type II LNs. Thus, in this situation, type I LNs would have to tolerate much higher free Ca^{2+} concentrations than type II LNs. This finding is supported by simulations with $\Delta[Ca^{2+}]_i$ and γ identical to PNs, but with variable Ca^{2+} binding ratio (Fig. 24C.2).

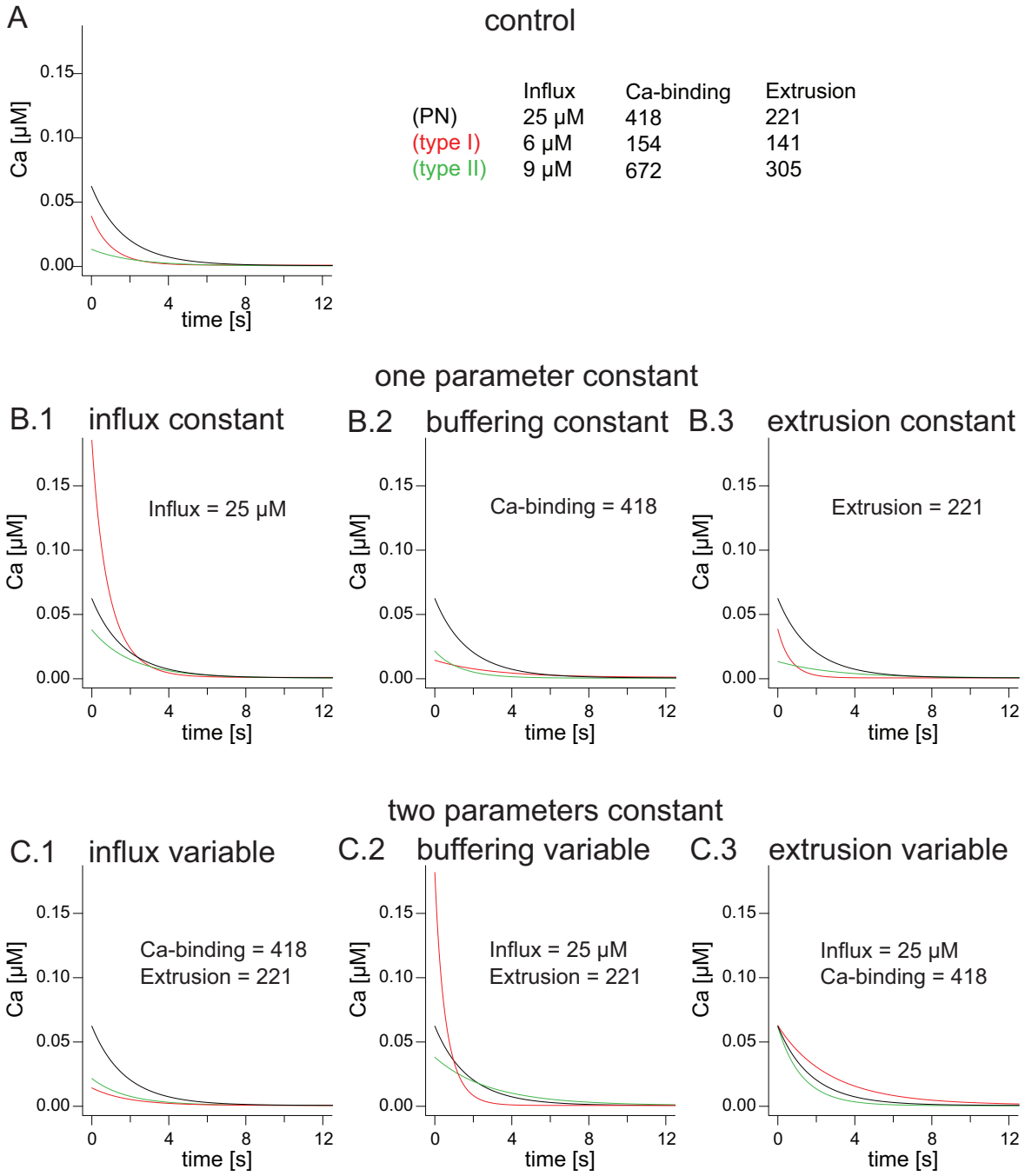

Figure 24: Computer simulations of the decay of $[Ca^{2+}]_i$ in PNs, type I and type II LNs
*Transients were numerically computed by integration of the differential equation 12. Initial values for the simulations were chosen so that the resulting kinetics represent typical PN, type I and type II LN: $[B_T]$ = 0 µM, $[BCa_p]$ = 200 µM, $\tau_{loading}$ = 1000 s, $K_{d,Fura}$ = 0.191 µM, $[Ca^{2+}]_{i,\infty}$ = 0 µM, influx, Ca^{2+} binding ratio and extrusion as indicated in the figure. (**A**) Control showing kinetics of Ca^{2+} signals as determined in this study. (**B**) To illustrate the interplay of influx, Ca^{2+} binding ratio and extrusion, the kinetics were simulated again, but one of the three parameters was set to the value of the PNs in each simulation. (**C**) Kinetics were simulated as in (A), but two parameters were set to the values of PNs (for details see text and legend of figure 1).*

In Fig. 24B.2 Ca^{2+} signals were simulated with identical parameters as in A, but with the same Ca^{2+} binding ratio for all cell types. The effect of an identical κ_S results in almost identical signals for type I and type II LNs. This indicates, that κ_S has the largest impact on the differences between type I and type II LNs. Fig. 24C.1 supports this view with simulated signals where κ_S and γ were identical to PNs and the influx was varied.

In Fig. 24B.3 Ca^{2+} signals were simulated with identical parameters as in A, but with the same extrusion rate for all cell types. The effect of an identical γ would result in higher absolute free Ca^{2+} concentrations in type I LNs than in type II LNs, but with faster time constants in type I LNs. This emphasizes that, because of the lower Ca^{2+} binding ratio in type I LNs, higher concentrations of free Ca^{2+} are generated. In Fig. 24C.3 $\Delta[Ca^{2+}]_i$ and κ_S were kept to the values of PNs, but the extrusion rate was varied. The resulting simulations varied only in their decay constants supporting the view that the extrusion rate has no effect on the peak Ca^{2+} concentration.

4.2.1 Individual parameters

With the 'added buffer approach' the essential parameters related to Ca^{2+} dynamics could be quantified. These were: Ca^{2+} increase $\Delta[Ca^{2+}]_i$, resting Ca^{2+} level $[Ca^{2+}]_{i,\infty}$, endogenous Ca^{2+} binding ratio κ_S, endogenous decay constant τ and extrusion rate γ. An essential requirement of the used method was that physiologically meaningful parameters could be reproducibly determined. To evaluate if this condition was met, values from this study are subsequently compared to previous findings. After that a general methodical discussion follows.

Ca^{2+} Influx and Resting Ca^{2+} level

Calcium influx was induced by voltage steps in voltage clamp mode while all non Ca^{2+} channels were blocked (Husch et al., 2008). Compared to inducing Ca^{2+} influx by action potentials (Helmchen et al., 1997), this appears somehow unphysiological. However, the big advantage of this approach is that the Ca^{2+} influx can be controlled and quantified more precisely. Due to the simple geometry of the investigated cell bodies sufficient voltage control was not a problem.

Resting Ca^{2+} level was between 0.048 μM (PNs) and 0.174 μM (type I LNs). This is well in the range observed in other vertebrate and invertebrate preparations (0.145-0.26 μM in rat neurohypophysial nerve endings (Stuenkel, 1994), 0.157 μM in motoneurones of the nucleus hypoglossus from mouse (Lips and Keller, 1998), 0.02-0.12 in snail neurons of H. pomatia (Schwiening and Thomas, 1996) and 0.046 μM in the calyx of Held (Helmchen et al., 1997)).

Buffering, decay and extrusion

The endogenous buffering capacity, determined with the linearized Neher-Augustine method (see Eq. 13), was between 154 (type I LNs) and 672 (type II LNs), which is well in the range found in previous studies. Previous estimates for κ_S range from 40 in the calyx of Held (Helmchen et al., 1997) or adrenal chromaffin cells (Zhou and Neher, 1993) to 900 in cerebellar Purkinje cells of 6-day-old rats (Fierro and Llano, 1996) (for review see Neher, 1995). The decay constants of the calcium signals were determined with single exponential fits. From the plot of τ over κ_B the decay constant with no exogenous buffer could be extrapolated to 1.1 s (type I LNs), 1.8 s (PNs) and 2.2 s (type II LNs), respectively. Previous estimates for decay constants ranged from 1-5 seconds in dissociated neurons from the rat nucleus basalis (Tatsumi and Katayama, 1993), 0.7 seconds in the soma of

hypoglossal motoneurons form mouse (Lips and Keller, 1998), 90 ms in the calyx of Held (Helmchen et al., 1997) to 70 ms in dendritic regions of cortical layer V neurons (Helmchen et al., 1996). Decay constants in somata (of dissociated or intact neurons) seem to be much slower than in dendritic or synaptic regions. This is physiologically sound, because in dendritic or synaptic regions signals with a higher spatio-temporal resolution are necessary for information processing. The relatively slow decay constants in somata are, at least in part, caused by the small ratio of surface/volume. Correspondingly to the long decay time constants, AL neurons have a relatively low Ca^{2+} extrusion rate between 141 s^{-1} (type I LNs) and 305 s^{-1} (type II LNs). Other authors have determined extrusion rates ranging from 60 s^{-1} in hypoglossal motoneurons from mouse (Lips and Keller, 1998), 900 s^{-1} in the calyx of Held (Helmchen et al., 1997) to 2000 s^{-1} in dendritic regions of cortical layer V neurons (Helmchen et al., 1996).

4.2.2 Methodical Implications

Absolute values related to Ca^{2+} handling have been determined in three functionally different neuron types. We could, for the first time, statistically confirm differences of these values by applying the bootstrap method. With this approach, statistical meaningful distributions of the individual parameters resulting from the Neher-Augustine model (Neher and Augustine, 1992) could be obtained (i.e. τ_{endo}, κ_S, γ). These distributions represented the probability with which the values for the individual parameters (τ_{endo}, κ_S, γ) would be found, if the same method was applied again to a different set of PNs, type I or type II LNs. Thus the values reported in this study only represent one possible result. A different experimenter would most likely find other mean values, but they should fall within the distributions shown in Fig. 15. Thus, when comparing values between different studies, the distributions of the reported values should always

be presented. For example, the distribution of the endogenous Ca^{2+} binding ratio of PNs (Fig. 15 C) covers a range from ~130 to ~1140, which spans the range of κ_S reported in previous studies. Without a statistic significance value from the other studies, it is impossible to state if the values from these studies fall within the same distributions or if they significantly differ from each other. I therefore suggest, that the bootstrap or an equivalent method should always be applied to the Neher-Augustine model, so that statistic tests can be assessed.

As stated above, some of the parameters had large distributions. Subsequently I suggest methodical improvements that could make them smaller.
Intracellular Ca^{2+} dynamics and absolute Ca^{2+} concentrations have been measured with the ratiometric Ca^{2+} indicator fura-2, which was first calibrated in vivo as favored by other authors (Helmchen F, 2005; Neher, 1989). The relationship between absolute Ca^{2+} concentration and fluorescence ratios was adopted from Grynkiewicz and Neher (Grynkiewicz et al., 1985; Neher, 1989). The K_d of fura-2, which is crucial for the added buffer approach, was determined with the isocoefficient method (Zhou and Neher, 1993). This is a standard method, however it does not take into account several findings: 1) Sources of error persist due to signal noise (from detection, amplification and digitization of the fluorescence signal) (Moore et al., 1990). 2) For in vivo calibration several measurements are necessary for each calibration solution, which is time consuming. We observed that, once in solution, fura-2 calibration parameters are unstable (the R_{max} value changed by 67% within three weeks). Pooling a set of experiments from the same fura-2 aliquot thus leads to a significant variance of the calibration parameters. 3) The behavior of fura-2 (its K_d) is altered by binding to proteins (Konishi et al., 1988) or the viscous cytosolic environment (Moore et al., 1990; Poenie, 1990). The same could be true for the Ca^{2+} chelator used to control the free Ca^{2+} concentration

in the calibration solutions. All this introduces uncertainties to the results of the calibration. We therefore suggest to calibrate fura-2 in vitro, because of a better control of the experimental conditions. Furthermore, the composition of the calibration solutions can be better controlled by actually measuring the free Ca^{2+} concentration with a metal electrode (McGuigan et al., 1991; McGuigan et al., 2006; McGuigan et al., 2007)

The linearized Neher-Augustine model is being used widely to quantify Ca^{2+} dynamics (Helmchen et al., 1996; Helmchen et al., 1997; Helmchen and Tank, 2005; Neher and Augustine, 1992; Tank et al., 1995; Vanselow and Keller, 2000). One of its underlying assumptions is that Ca^{2+} signals need to be small so that they can be described by a monoexponential function. According to (Tank et al., 1995) this means that the free Ca^{2+} concentration of a recorded signal should be smaller than 0.5 times the K_d of the used indicator. The signals presented in Fig. 12 to 14 sufficiently fulfill this criterion and could be well approximated by monoexponentials. However, the residuals were never purely randomly scattered, indicating that a biexponential function would potentially better describe these transients. Thus, it seems to be critical to assume that Ca^{2+} transients can be described by a monoexponential model. It might therefore be appropriate to work without the linearization leading to the monoexponential Eq. 13, but to estimate Ca^{2+} related parameters from the full differential equation of Ca^{2+} dynamics (Eq. 12). However, future studies have to show if such a procedure actually leads to improved estimates of buffering related parameters.

4.2.3 Calcium buffering in small neuronal compartments

Fig. 17 proves the experimental possibility of obtaining loading curves and Ca^{2+} signals with a high signal to noise ratio in individual glomeruli of PNs. In

principle this enables the application of the Neher-Augustine method to small neuronal compartments. However, the Ca^{2+} influx in glomeruli is so large that the signals become biphasic. Because the criterion of a small signal is no longer fulfilled, they cannot be fitted with monoexponential functions. The signals in glomeruli can therefore not be analyzed with the linearized model used in this study. To quantify buffering related parameters in the glomeruli of PNs a method needs to be developed to analyze signals with multiple exponentials.

4.3 Imaging of odor evoked calcium signals

Odor responses of single LNs have been measured on the glomerular level using Ca^{2+} imaging methods combined with electrophysiological recordings.

4.3.1 Implications for olfactory coding

LNs are postulated to be part of two local networks in the AL, one is glomerulus specific, acting on preferential glomeruli and the other is global, acting on all glomeruli (Silbering and Galizia, 2007). In this study LNs are presented that could shape both types of networks. Different qualitative response profiles have been found. One group of LNs reacted to a set of odors with specific glomerular activities. In these LNs individual glomeruli were broadly tuned with high activity for many or all odors, whereas in the same neurons other glomeruli were narrowly tuned responding only to a subset of odors. A second group of LNs reacted uniformly to a set of odors. In these LNs all glomeruli were broadly tuned with high activity for all presented odors. These results provide the first direct evidence about the character of glomerular interactions in single LNs.

LNs are important components of the olfactory network in the AL of insects involved in olfactory information processing (Hildebrand and Shepherd, 1997;

Wilson and Mainen, 2006). Many authors denote them a decisive role for modulating PN output (Olsen et al., 2007; Olsen and Wilson, 2008; Root et al., 2007; Shang et al., 2007; Silbering and Galizia, 2007; Wilson and Laurent, 2005). One mechanism of this modulation could be based on the interglomerular connections of single LNs that form a glomerulus dependent inhibitory network (Root et al., 2007; Sachse and Galizia, 2002; Wilson and Laurent, 2005). This mechanism could be understood as a contrast-enhancement device. Previous studies propose that neighboring glomeruli inhibit each other, such that a principal neuron with strong activity to a specific odor would suppress glomeruli that are weakly activated by the same odor (Uchida et al., 2000; Yokoi et al., 1995). Neighboring glomeruli in this sense need not be spatial neighbors, but preferentially connected glomeruli (Sachse and Galizia, 2002). This view therefore proposes the existence of inhibitory LNs that preferentially connect certain glomeruli. However, the existence of such neurons has never been proven by direct physiological experiments before. This study proves for the fist time, by measuring glomerulus specific odor responses, the existence of such neurons. Fig. 18 gives an example of a LN that seems to preferentially connect glomeruli 3, 14 and 15, which are broadly tuned to all odors tested. Glomeruli 22 and 23, in contrast, seem to be preferentially activated for geraniol and hexanol, but not for other odors. Preliminary antibody stainings suggest that this type releases the inhibitory transmitter GABA (Fusca, 2007). Thus, this neuron could form an odor specific glomerulus-dependent inhibitory network by its own intrinsic properties.

Another postulated mechanism of PN output modulation is based on a global inhibitory network. According to this view, neurons innervating most or all glomeruli would inhibit the whole antennal lobe serving as a global gain control (Sachse and Galizia, 2002). Accordingly, the existence of a neuron type is proposed that connects many glomeruli without preference. This study provides the

evidence for the existence of such neurons. Fig. 22 gives an example of a LN that is uniformly active in all glomeruli to all presented odors. Preliminary antibody stainings suggest that this neuron type also releases GABA. Thus this neuron could be part of a global inhibitory network.

A third postulated mechanism of PN output modulation is based on lateral excitatory inputs that give rise to a distributed representation of olfactory information in PNs (Olsen et al., 2007; Shang et al., 2007; Wilson et al., 2004). A complex network of lateral interactions could redistribute oder-evoked activity over a larger ensemble of PNs, thereby enhancing the coding space. Excitatory circuits could also be important to rise background activity therefore boosting small signals so that they are discovered by coincidence detectors such as the Kennyon cells (Shang et al., 2007). Some authors suggest that this network specifically activates exclusive glomeruli (Silbering and Galizia, 2007). Accordingly, a type of LN is predicted that preferentially connects certain gomeruli and releases an excitatory transmitter. In this study a neuron type was found that most likely does not release the inhibitory transmitter GABA (Fig. 21; Fusca, 2007), which is therefore a candidate for an excitatory LN. This neuron preferentially activates glomeruli 1, 3, and 10 for hexanol and could therefore be part of the excitatory network, which exclusively activates specific glomeruli. However, unless the transmitter is revealed, nothing can be speculated about the excitatory or inhibitory nature of this neuron.

The experiments have been performed in a physiological preparation with a combination of electrophysiological recordings, calcium imaging and odor stimulation. With this method odor evoked activity could be measured in single neurons on the glomerular level, revealing glomerulus-specific and glomerulus-unspecific activities in different LNs. This method allows to further investigate

how local interneurons form locally restricted interconnections. Future studies need to reveal, if the measured calcium activity comes from voltage activated channels representing neuron output or from postsynaptic calcium increases, which would arise from neuron input.

4.3.2 Significance of calcium buffering

In neurons, calcium regulates a multitude of cellular functions. It can act as a charge carrier that contributes to the membrane potential, or it serves as a second messenger with diverse effects such as activation of enzymes or regulation of calcium dependent ion channels (Augustine et al., 2003; Berridge, 1998). A prominent effect of calcium is to provide the trigger for synaptic release. Consequently, calcium serves as an excellent monitor of general neuronal activity (Carlsson et al., 2005; Galizia and Kimmerle, 2004; Sachse and Galizia, 2002). However, it has to be kept in mind that indicators used to observe Ca^{2+} activity act as buffers, which distort the endogenous signal (Helmchen et al., 1996; Neher and Augustine, 1992; Tank et al., 1995). The higher the indicator's concentration and affinity, the stronger amplitudes are lowered and time constants are prolonged. Throughout this study, relatively high concentrations (600 μM) of the high-affinity Ca^{2+} indicator Oregon-Green-Bapta-1 were used and its concentrations in the neurons was not precisely determined. The effects of the indicator on amplitudes and time constants of the endogenous signals could therefore not be quantified. Thus, absolute amplitudes and time constants were not compared between experiments. However, relative calcium amplitudes in the glomeruli could be compared within one experiment. The resulting tuning curves already gave important implications for olfactory information processing in LNs (see above). Nevertheless, in the future, absolute amplitudes and kinetics of calcium signals should be analyzed in the different cell types with a better control of the indicator

concentration. From such a study further conclusions about the source of calcium can be made.

4.3.3 Measuring calcium activity with CCD cameras

Calcium imaging experiments in PNs, where only one glomerulus is present, have proven the feasibility of resolving single glomeruli with a CCD camera. In LNs, activities were measured from regions of interest that had been recognized as glomerular structures from transmission images using IR-DIC optics. However, individual glomeruli could not be identified and compared between different cell types like in *Drosophila* preparations (Olsen et al., 2007; Root et al., 2007; Shang et al., 2007; Silbering and Galizia, 2007; Wilson and Laurent, 2005) or the honeybee (Galizia and Kimmerle, 2004; Sachse and Galizia, 2002; Sachse and Galizia, 2003). Nevertheless, general glomerulus specific activities could be determined proving preferential activation of certain glomeruli in some neurons and uniform activation in other neurons. High amounts of the high affinity indicator Oregon-Green-Bapta-1 were necessary to obtain signals with a CCD camera from glomeruli. CCD cameras are not as sensitive on the subcellular level like for instance laser-scanning-microscopes (LSMs). However, it is more difficult to detect glomerular differences with a LSM, because only one focal plane can be analyzed at the same time potentially masking differences from other levels. Glomerular differences could thus be detected more easily with a CCD camera. On the other hand a CCD camera does not have a good resolution in deep tissue. It is more difficult to discriminate from which level the recorded signal actually comes. Signals from overlapping glomeruli could misshape each other. That is why future experiments with a LSM or a multiphoton microscope should be assigned to better discriminate between individual glomeruli. A general overview of the activity in the antennal lobe has been presented in this work. The next steps will be to take

closer looks at individual neighboring and distant glomeruli to better understand their interaction.

4.3.4 Outlook and experimental plan

The work from this part provided compelling evidence for glomerular interactions. Subsequently I want to outline some future experiments that should be conducted to provide further explanations about the character of glomerular interactivity in LNs.

- The experiments should be reproduced with the same number of odors for all experiments to see if the same neuron types always react either glomerulus specifically to an odor or uniformly. The same odor should be applied several times to evaluate the reproducibility of the tuning curves.
- It appears from morphological analyses that the innervations of some glomeruli are spatially clustered. Detailed 3D reconstructions with a systematic analysis of the neurons' anatomy could support this finding.
- Experiments with high time resolution (line scans) are necessary to resolve where the calcium actually comes from. The actual sites of influx and diffusional effects could so be discriminated.
- The type of transmitter released by the different neuron types could give further clues about the LN network and their function in olfactory coding in general.
- A mid term project would be to establish a glomerular map of the antennal lobe. Imaging experiments with PNs and LNs in identified glomeruli would give further clues about where the inputs come from and where the outputs go to. To answer this question double patch-clamp experiments with PNs and LNs were very useful.

List of Figures

Figure 1: Single compartment model of calcium buffering.....15

Figure 2: Olfactory pathways in the insect olfactory system.....17

Figure 3: Determination of isocoefficient.....27

Figure 4: Behavior of EGTA when temperature or pH are changed.....30

Figure 5: Raw odor evoked Ca^{2+} signal from a type I LN.....38

Figure 6: Calcium currents from identified neurons.....43

Figure 7: Electrophysiological characteristics of different neuron types.....45

Figure 8: Acquisition of loading curve and Ca^{2+} decay kinetics.....48

Figure 9: Parameters of Ca^{2+} influx, cell volume and resting level.....50

Figure 10: Analysis of loading curves.....52

Figure 11: Analysis of Ca^{2+} buffering in cultured neurons.....54

Figure 12: Analysis of Ca^{2+} buffering in projection neurons.....55

Figure 13: Analysis of Ca^{2+} buffering in type I interneurons.....56

Figure 14: Analysis of Ca^{2+} buffering in type II interneurons.....57

Figure 15: Bootstrap analysis of buffering related parameters.....59

Figure 16: Scheme of Ca^{2+} dynamics in uPNs, type I and type II LNs.....60

Figure 17: Loading curve and Ca^{2+} signals in small neuronal comparments of uPNs.....62

Figure 18: Ca^{2+} Imaging in a type I LN with glomerulus specific odor responses.....67

Figure 19: Electrophysiological responses to different odors of a yet unidentified LN.....68

Figure 20: Ca^{2+} imaging in an unidentified LN with glomerulus specific odor responses . 70

Figure 21: Ca^{2+} imaging in a type II LN with glomerulus specific odor responses.....72

Figure 22: Ca^{2+} imaging in a type I LN with uniform glomerular odor responses.....74

Figure 23: Odor evoked Ca^{2+} signals in subcellular compartments of a PN.....75

Figure 24: Computer simulations of the decay of $[Ca^{2+}]_i$ in PNs, type I and type II LNs.....81

References

Armstrong, C.M. Bezanilla, F (1974) Charge movement associated with the opening and closing of the activation gates of the Na channels. J Gen Physiol 63: 533-552.

Augustine, G.J., Santamaria, F Tanaka, K (2003) Local calcium signaling in neurons. Neuron 40: 331-346.

Bar-Yehuda, D. Korngreen, A (2008) Space-clamp problems when voltage clamping neurons expressing voltage-gated conductances. J Neurophysiol 99: 1127-1136.

Benquet, P., Le Guen, J, Dayanithi, G, Pichon, Y Tiaho, F (1999) omega-AgaIVA-sensitive (P/Q-type) and -resistant (R-type) high-voltage-activated Ba2+ currents in embryonic cockroach brain neurons. Journal of Neurophysiology 82: 2284-2293.

Berridge, M.J. (1998) Neuronal calcium signaling. Neuron 21: 13-26.

Bers, D.M., Patton, C.W Nuccitelli, R (1994) A practical guide to the preparation of Ca^{2+} buffers. Methods Cell Biol 40: 3-29.

Bhandawat, V., Olsen, S.R, Gouwens, N.W, Schlief, M.L Wilson, R.I (2007) Sensory processing in the Drosophila antennal lobe increases reliability and separability of ensemble odor representations. Nat Neurosci 10: 1474-1482.

Boeckh, J. (1974) Reactions of Olfactory Neurons in Insect Deutocerebrum as Compared to Response Patterns of Olfactory Receptor Cells. Journal of Comparative Physiology 90: 183-205.

Boeckh, J. Ernst, K.D (1987) Contribution of Single Unit Analysis in Insects to an Understanding of Olfactory Function. Journal of Comparative Physiology a-Sensory Neural and Behavioral Physiology 161: 549-565.

Boeckh, J. Tolbert, L.P (1993) Synaptic organization and development of the antennal lobe in insects. Microsc Res Tech 24: 260-280.

Brooks, S.P. Storey, K.B (1992) Bound and determined: a computer program for making buffers of defined ion concentrations. Anal Biochem 201: 119-126.

Buck, L. Axel, R (1991) A novel multigene family may encode odorant receptors: a molecular basis for odor recognition. Cell 65: 175-187.

Carlsson, M.A., Knusel, P, Verschure, P.F Hansson, B.S (2005) Spatio-temporal Ca^{2+} dynamics of moth olfactory projection neurones. Eur J Neurosci 22: 647-657.

Christensen, T.A., Waldrop, B.R, Harrow, I.D Hildebrand, J.G (1993) Local interneurons and information processing in the olfactory glomeruli of the moth Manduca sexta. J Comp Physiol [A] 173: 385-399.

Collin, T., Chat, M, Lucas, M.G, Moreno, H, Racay, P, Schwaller, B, Marty, A Llano, I (2005) Developmental changes in parvalbumin regulate presynaptic Ca^{2+} signaling. J Neurosci 25: 96-107.

Davis, R.L. (2004) Olfactory learning. Neuron 44: 31-48.

Distler, P. (1989) Histochemical demonstration of GABA-like immunoreactivity in cobalt labeled neuron individuals in the insect olfactory pathway. Histochemistry 91: 245-249.

Distler, P.G. Boeckh, J (1997a) Synaptic connections between identified neuron types in the antennal lobe glomeruli of the cockroach, Periplaneta americana: I. Uniglomerular projection neurons. J Comp Neurol 378: 307-319.

Distler, P.G. Boeckh, J (1997b) Synaptic connections between identified neuron types in the antennal lobe glomeruli of the cockroach, Periplaneta americana: II. Local multiglomerular interneurons. J Comp Neurol 383: 529-540.

Distler, P.G. Boeckh, J (1998) An improved model of the synaptic organization of insect olfactory glomeruli. Ann N Y Acad Sci 855: 508-510.

Distler, P.G., Gruber, C Boeckh, J (1998) Synaptic connections between GABA-immunoreactive neurons and uniglomerular projection neurons within the antennal lobe of the cockroach, Periplaneta americana. Synapse 29: 1-13.

Dodt, H.U. Zieglgansberger, W (1994) Infrared videomicroscopy: a new look at neuronal structure and function. Trends Neurosci 17: 453-458.

Edmonds, B., Reyes, R, Schwaller, B Roberts, W.M (2000) Calretinin modifies presynaptic calcium signaling in frog saccular hair cells. Nat Neurosci 3: 786-790.

Efron, B. (1979) 1977 Rietz Lecture - Bootstrap Methods - Another Look at the Jackknife. Annals of Statistics 7: 1-26.

Fiala, A. (2007) Olfaction and olfactory learning in Drosophila: recent progress. Curr Opin Neurobiol 17: 720-726.

Fierro, L. Llano, I (1996) High endogenous calcium buffering in Purkinje cells from rat cerebellar slices. J Physiol 496 (Pt 3): 617-625.

Fusca, D. (2007) GABA-like Immunoreactivity in the Antennal Lobe of Periplaneta americana A Study on Identified Local Interneurons. Universität zu Köln, Zoologisches Institut: Diplomarbeit.

Galizia, C.G. Kimmerle, B (2004) Physiological and morphological characterization of honeybee olfactory neurons combining electrophysiology, calcium imaging and confocal microscopy. J Comp Physiol A Neuroethol Sens Neural Behav Physiol 190: 21-38.

Galizia, C.G., Sachse, S, Rappert, A Menzel, R (1999) The glomerular code for odor representation is species specific in the honeybee Apis mellifera. Nat Neurosci 2: 473-478.

Gao, Q., Yuan, B Chess, A (2000) Convergent projections of Drosophila olfactory neurons to specific glomeruli in the antennal lobe. Nat Neurosci 3: 780-785.

Grolleau, F. Lapied, B (1996) Two distinct low-voltage-activated Ca^{2+} currents contribute to the pacemaker mechanism in cockroach dorsal unpaired median neurons. J Neurophysiol 76: 963-976.

Grynkiewicz, G., Poenie, M Tsien, R.Y (1985) A new generation of Ca^{2+} indicators with greatly improved fluorescence properties. J Biol Chem 260: 3440-3450.

Hackney, C.M., Mahendrasingam, S, Penn, A Fettiplace, R (2005) The concentrations of calcium buffering proteins in mammalian cochlear hair cells. J Neurosci 25: 7867-7875.

Hamill, O.P., Marty, A, Neher, E, Sakmann, B Sigworth, F.J (1981) Improved Patch-Clamp Techniques for High-Resolution Current Recording from Cells and Cell-Free Membrane Patches. Pflugers Archiv-European Journal of Physiology 391: 85-100.

Harrison, S.M. Bers, D.M (1987) The effect of temperature and ionic strength on the apparent Ca-affinity of EGTA and the analogous Ca-chelators BAPTA and dibromo-BAPTA. Biochim Biophys Acta 925: 133-143.

Harrison, S.M. Bers, D.M (1989) Correction of proton and Ca association constants of EGTA for temperature and ionic strength. Am J Physiol 256: C1250-6.

Hayashi, J.H. Hildebrand, J.G (1990) Insect olfactory neurons in vitro: morphological and physiological characterization of cells from the developing antennal lobes of Manduca sexta. J Neurosci 10: 848-859.

Heidel, E. Pfluger, H.J (2006) Ion currents and spiking properties of identified subtypes of locust octopaminergic dorsal unpaired median neurons. Eur J Neurosci 23: 1189-1206.

Helmchen F (2005) Calibration of fluorescent calcium indicators. in Imaging in neuroscience and development, Edition (edited by Yuste R & Konnerth A ed.), p. 253-263. Cold Spring Harbor Laboratory Press.

Helmchen, F. Tank, D.W (2005) A Single-Compartment Model of Calcium Dynamics in Nerve Terminals and Dendrites. in Imaging in Neuroscience and Development, Edition (R. Yuste and A. Konnerth ed.), p. 265-275. Cold Spring Harbor Laboratory Press, Cold Spring Harbor, New York.

Helmchen, F., Borst, J.G Sakmann, B (1997) Calcium dynamics associated with a single action potential in a CNS presynaptic terminal. Biophys J 72: 1458-1471.

Helmchen, F., Imoto, K Sakmann, B (1996) Ca^{2+} buffering and action potential-evoked Ca^{2+} signaling in dendrites of pyramidal neurons. Biophys J 70: 1069-1081.

Hildebrand, J.G. Shepherd, G.M (1997) Mechanisms of olfactory discrimination: converging evidence for common principles across phyla. Annu Rev Neurosci 20: 595-631.

Hille, B. (2001) Ion Channels of Excitable Membranes, Edition: Sinauer Associates, Inc, Sunderland, Massachusetts USA.

Husch, A. (2007) Diversity of Voltage Activated Calcium Currents in Identified Olfactory Interneurons. Universität zu Köln: Inaugural-Dissertation.

Husch, A., Hess, S Kloppenburg, P (2008) Functional parameters of voltage-activated Ca^{2+} currents from olfactory interneurons in the antennal lobe of Periplaneta americana. J Neurophysiol 99: 320-332.

Jackson, M.B. Redman, S.J (2003) Calcium dynamics, buffering, and buffer saturation in the boutons of dentate granule-cell axons in the hilus. J Neurosci 23: 1612-1621.

Kirchhof, B.S. Mercer, A.R (1997) Antennal lobe neurons of the honey bee, Apis mellifera, express a D2-like dopamine receptor in vitro. J Comp Neurol 383: 189-198.

Kloppenburg, P. Hörner, M (1998) Voltage-activated currents in identified giant interneurons isolated from adult crickets gryllus bimaculatus. J Exp Biol 201 (Pt 17): 2529-2541.

Kloppenburg, P., Ferns, D Mercer, A.R (1999a) Serotonin enhances central olfactory neuron responses to female sex pheromone in the male sphinx moth manduca sexta. J Neurosci 19: 8172-8181.

Kloppenburg, P., Kirchhof, B.S Mercer, A.R (1999b) Voltage-activated currents from adult honeybee (Apis mellifera) antennal motor neurons recorded in vitro and in situ. J Neurophysiol 81: 39-48.

Konishi, M., Olson, A, Hollingworth, S Baylor, S.M (1988) Myoplasmic binding of fura-2 investigated by steady-state fluorescence and absorbance measurements. Biophys J 54: 1089-1104.

Laurent, G. Davidowitz, H (1994) Encoding of Olfactory Information with Oscillating Neural Assemblies. Science 265: 1872-1875.

Laurent, G. (1999) A systems perspective on early olfactory coding. Science 286: 723-728.

Lee, S.H., Rosenmund, C, Schwaller, B Neher, E (2000) Differences in Ca^{2+} buffering properties between excitatory and inhibitory hippocampal neurons from the rat. J Physiol 525 Pt 2: 405-418.

Lee, S.H., Schwaller, B Neher, E (2000) Kinetics of Ca^{2+} binding to parvalbumin in bovine chromaffin cells: implications for [Ca^{2+}] transients of neuronal dendrites. J Physiol 525 Pt 2: 419-432.

Lips, M.B. Keller, B.U (1998) Endogenous calcium buffering in motoneurones of the nucleus hypoglossus from mouse. J Physiol 511 (Pt 1): 105-117.

Loehle, C. Rittenhouse, L.R (1982) An Analysis of Forage Preference Indexes. Journal of Range Management 35: 316-319.

Malun, D. (1991a) Inventory and distribution of synapses of identified uniglomerular projection neurons in the antennal lobe of Periplaneta americana. J Comp Neurol 305: 348-360.

Malun, D. (1991b) Synaptic relationships between GABA-immunoreactive neurons and an identified uniglomerular projection neuron in the antennal lobe of Periplaneta americana: a double-labeling electron microscopic study. Histochemistry 96: 197-207.

Malun, D., Waldow, U, Kraus, D Boeckh, J (1993) Connections between the deutocerebrum and the protocerebrum, and neuroanatomy of several classes of deutocerebral projection neurons in the brain of male Periplaneta americana. J Comp Neurol 329: 143-162.

McGuigan, J.A., Kay, J.W Elder, H.Y (2006) Critical review of the methods used to measure the apparent dissociation constant and ligand purity in Ca^{2+} and Mg^{2+} buffer solutions. Prog Biophys Mol Biol 92: 333-370.

McGuigan, J.A., Kay, J.W, Elder, H.Y Luthi, D (2007) Comparison between measured and calculated ionised concentrations in Mg^{2+} /ATP, Mg^{2+} /EDTA and Ca^{2+} /EGTA buffers; influence of changes in temperature, pH and pipetting errors on the ionised concentrations. Magnes Res 20: 72-81.

McGuigan, J.A., Luthi, D Buri, A (1991) Calcium buffer solutions and how to make them: a do it yourself guide. Can J Physiol Pharmacol 69: 1733-1749.

Mills, J.D. Pitman, R.M (1997) Electrical properties of a cockroach motor neuron soma depend on different characteristics of individual Ca components. Journal of Neurophysiology 78: 2455-2466.

Mizunami, M., Weibrecht, J.M Strausfeld, N.J (1998) Mushroom bodies of the cockroach: their participation in place memory. J Comp Neurol 402: 520-537.

Moore, E.D., Becker, P.L, Fogarty, K.E, Williams, D.A Fay, F.S (1990) Ca^{2+} imaging in single living cells: theoretical and practical issues. Cell Calcium 11: 157-179.

Muller, M., Felmy, F, Schwaller, B Schneggenburger, R (2007) Parvalbumin is a mobile presynaptic Ca^{2+} buffer in the calyx of held that accelerates the decay of Ca^{2+} and short-term facilitation. J Neurosci 27: 2261-2271.

Neher, E. (1989) Combined fura-2 and patch clamp measurements in rat peritoneal mast cells. in Neuromuscular Junction, Edition (L.C. Sellin, R. Libelius and S. Thesleff ed.), p. 65-76. Elsevier Science Publishers, Amsterdam.

Neher, E. (1992) Correction for liquid junction potentials in patch clamp experiments. Methods Enzymol 207: 123-131.

Neher, E. (1995) The use of fura-2 for estimating Ca buffers and Ca fluxes. Neuropharmacology 34: 1423-1442.

Neher, E. Augustine, G.J (1992) Calcium gradients and buffers in bovine chromaffin cells. J Physiol 450: 273-301.

Ng, M., Roorda, R.D, Lima, S.Q, Zemelman, B.V, Morcillo, P Miesenbock, G (2002) Transmission of olfactory information between three populations of neurons in the antennal lobe of the fly. Neuron 36: 463-474.

Olsen, S.R. Wilson, R.I (2008) Lateral presynaptic inhibition mediates gain control in an olfactory circuit. Nature : .

Olsen, S.R., Bhandawat, V Wilson, R.I (2007) Excitatory interactions between olfactory processing channels in the Drosophila antennal lobe. Neuron 54: 89-103.

Patton, C., Thompson, S Epel, D (2004) Some precautions in using chelators to buffer metals in biological solutions. Cell Calcium 35: 427-431.

Poenie, M. (1990) Alteration of intracellular Fura-2 fluorescence by viscosity: a simple correction. Cell Calcium 11: 85-91.

Ressler, K.J., Sullivan, S.L Buck, L.B (1994) Information coding in the olfactory system: evidence for a stereotyped and highly organized epitope map in the olfactory bulb. Cell 79: 1245-1255.

Root, C.M., Semmelhack, J.L, Wong, A.M, Flores, J Wang, J.W (2007) Propagation of olfactory information in Drosophila. Proc Natl Acad Sci U S A 104: 11826-11831.

Sachse, S. Galizia, C.G (2002) Role of inhibition for temporal and spatial odor representation in olfactory output neurons: a calcium imaging study. J Neurophysiol 87: 1106-1117.

Sachse, S. Galizia, C.G (2003) The coding of odour-intensity in the honeybee antennal lobe: local computation optimizes odour representation. Eur J Neurosci 18: 2119-2132.

Sakura, M., Okada, R Mizunami, M (2002) Olfactory discrimination of structurally similar alcohols by cockroaches. J Comp Physiol A Neuroethol Sens Neural Behav Physiol 188: 787-797.

Schafer, S., Rosenboom, H Menzel, R (1994) Ionic currents of Kenyon cells from the mushroom body of the honeybee. J Neurosci 14: 4600-4612.

Schoenmakers, T.J., Visser, G.J, Flik, G Theuvenet, A.P (1992) CHELATOR: an improved method for computing metal ion concentrations in physiological solutions. Biotechniques 12: 870-4, 876-9.

Schwiening, C.J. Thomas, R.C (1996) Relationship between intracellular calcium and its muffling measured by calcium iontophoresis in snail neurones. J Physiol 491 (Pt 3): 621-633.

Shang, Y.H., Claridge-Chang, A, Sjulson, L, Pypaert, M Miesenbock, G (2007) Excitatory local circuits and their implications for olfactory processing in the fly antennal lobe. Cell 128: 601-612.

Silbering, A.F. Galizia, C.G (2007) Processing of odor mixtures in the Drosophila antennal lobe reveals both global inhibition and glomerulus-specific interactions. J Neurosci 27: 11966-11977.

Strausfeld, N.J. Hildebrand, J.G (1999) Olfactory systems: common design, uncommon origins?. Curr Opin Neurobiol 9: 634-639.

Stuenkel, E.L. (1994) Regulation of intracellular calcium and calcium buffering properties of rat isolated neurohypophysial nerve endings. J Physiol 481 (Pt 2): 251-271.

Tank, D.W., Regehr, W.G Delaney, K.R (1995) A quantitative analysis of presynaptic calcium dynamics that contribute to short-term enhancement. J Neurosci 15: 7940-7952.

Tatsumi, H. Katayama, Y (1993) Regulation of the intracellular free calcium concentration in acutely dissociated neurones from rat nucleus basalis. J Physiol 464: 165-181.

Uchida, N., Takahashi, Y.K, Tanifuji, M Mori, K (2000) Odor maps in the mammalian olfactory bulb: domain organization and odorant structural features. Nat Neurosci 3: 1035-1043.

Vanselow, B.K. Keller, B.U (2000) Calcium dynamics and buffering in oculomotor neurones from mouse that are particularly resistant during amyotrophic lateral sclerosis (ALS)-related motoneurone disease. J Physiol 525 Pt 2: 433-445.

Vetter, R.S., Sage, A.E, Justus, K.A, Carde, R.T Galizia, C.G (2006) Temporal integrity of an airborne odor stimulus is greatly affected by physical aspects of the odor delivery system. Chem Senses 31: 359-369.

von Lewinski, F. Keller, B.U (2005) Ca^{2+}, mitochondria and selective motoneuron vulnerability: implications for ALS. Trends in Neurosciences 28: 494-500.

Wang, J.W., Wong, A.M, Flores, J, Vosshall, L.B Axel, R (2003) Two-photon calcium imaging reveals an odor-evoked map of activity in the fly brain. Cell 112: 271-282.

Watanabe, H., Kobayashi, Y, Sakura, M, Matsumoto, Y Mizunami, M (2003) Classical olfactory conditioning in the cockroach Periplaneta americana. Zoolog Sci 20: 1447-1454.

Wicher, D. Penzlin, H (1997) Ca^{2+} currents in central insect neurons: Electrophysiological and pharmacological properties. Journal of Neurophysiology 77: 186-199.

Wilson, R.I. Laurent, G (2005) Role of GABAergic inhibition in shaping odor-evoked spatiotemporal patterns in the Drosophila antennal lobe. J Neurosci 25: 9069-9079.

Wilson, R.I. Mainen, Z.F (2006) Early events in olfactory processing. Annu Rev Neurosci 29: 163-201.

Wilson, R.I., Turner, G.C Laurent, G (2004) Transformation of olfactory representations in the Drosophila antennal lobe. Science 303: 366-370.

Wong, A.M., Wang, J.W Axel, R (2002) Spatial representation of the glomerular map in the Drosophila protocerebrum. Cell 109: 229-241.

Yokoi, M., Mori, K Nakanishi, S (1995) Refinement of odor molecule tuning by dendrodendritic synaptic inhibition in the olfactory bulb. Proc Natl Acad Sci U S A 92: 3371-3375.

Zhou, Z. Neher, E (1993) Mobile and immobile calcium buffers in bovine adrenal chromaffin cells. J Physiol 469: 245-273.

Danksagung

Diese Arbeit wäre ohne Hilfe so nicht zustande gekommen. Daher danke ich allen, die mir zu diesem Werk verholfen haben:

- Prof. Dr. Peter Kloppenburg für eine außerordentliche Betreuung und viele fruchtbare Diskussionen, durch die sich immer wieder neue Richtungen ergeben haben und durch die meine Arbeit schließlich nicht ganz auf die geplante, aber doch zum Ziel führende Gerade gebracht wurde. Besonderen Dank auch für die exzellente Einrichtung des Labors und Materialversorgung.

- Prof. Dr. Arnd Baumann für sein Zweitgutachten und die uneingeschränkte Unterstützung während meiner ganzen Arbeit.

Ganz besonderer Dank gilt der Konrad-Adenauer-Stiftung, ohne deren finanzielle Unterstützung ich diese Arbeit nicht hätte durchführen können. Danke auch für die zahlreichen Ablenkungen in Form von interessanten Seminaren und Treffen.

Dr. Christophe Pouzat danke ich dafür, dass er die Lehre des Meisters nicht als selbstverständlich angenommen hat.

Meinen Eltern danke ich für den festen Glauben an mich und meinen Lebensweg und die zahlreichen finanziellen Spritzen ohne die ich es sehr viel schwerer gehabt hätte.

Prof. Dr. Wolfgang Walkowiak danke ich für die Fortbildungen auf dem Gebiet der Önologie, die nicht nur rein wissenschaftlicher Natur waren.

Meinen Kollegen danke ich unter anderem für die Ko-teilnahme an den önologischen Kursen, wodurch diese immer lang, aber auch kurzweilig wurden. Kollege Andreas Husch danke ich für die Zellkulturexperimente und das Mitkämpfen an der Pufferungs-Front, Moritz Paehler für die Einführung in die Stimulationstechnik mit Düften. Simon Hess danke ich für die Begleitung zu den Neurodegenerativen Krankheiten und bei der Erforschung von einem Thema, das irgendwie mit Vergessen zu tun hat. Debora Fusca für die Antikörperfärbungen. Heike Demmer, Moritz Paehler, Andreas Husch und Nicole Lindemann für die Korrektur meines Manuskripts, Helmut Wratil für die beste technische Assistenz, die sich ein Doktorand wünschen kann und Lars Paeger für die Einführung in die Nasenrolltechnik. Euch allen danke ich für eine gute Zeit.

Der Debeka danke ich, dass sie nach angeregten Briefwechseln meine Doktorarbeit doch noch als Teil meiner Ausbildung angesehen hat.

Meinen Freunden, insbesondere Pia, Fox, Tina, Ralf, Kiki und Dirk danke ich für die mentale Unterstützung und die vielen Gespräche, die vor allem eins gemeinsam hatten: eher selten wurde über Kalziumpuffer oder Duftantworten gesprochen.

Eine Doktorarbeit. Als ob es eine Stück Kuchen wäre, das man aus Eiern, Mehl und Zucker zusammenrührt. Eine geistige Schöpfung ist es, das Einzelne wie das Ganze aus einem Geiste und Guss und von dem Hauche eines Lebens durchdrungen. Für diesen Hauch danke ich meiner Alex, die mit ihrer Liebe, Zuwendung und den kleinen Ablenkungen immer dann da war, wenn es am nötigsten war. You're the one I like best, you retain my interest (The sweetest perfection).

Erklärung

Ich versichere, dass ich die von mir vorgelegte Dissertation selbständig angefertigt, die benutzten Quellen und Hilfsmittel vollständig angegeben und die Stellen der Arbeit − einschließlich Tabellen, Karten und Abbildungen −, die anderen Werken im Wortlaut oder dem Sinn nach entnommen sind, in jedem Einzelfall als Entlehnung kenntlich gemacht habe; dass diese Dissertation noch keiner anderen Fakultät oder Universität zur Prüfung vorgelegen hat; dass sie − abgesehen von unten angegebenen Teilpublikationen − noch nicht veröffentlicht worden ist sowie, dass ich eine solche Veröffentlichung vor Abschluss des Promotionsverfahrens nicht vornehmen werde. Die Bestimmungen der Promotionsordnung sind mir bekannt. Die von mir vorgelegte Dissertation ist von Prof. Dr. Peter Kloppenburg betreut worden.

Köln, den 22.4.2008

Teilpuplikationen

Poster and Abstracts

Pippow A, Husch A, Pouzat C and Kloppenburg P (2007), Calcium dynamics in olfactory interneurons, Program No. T20-8B, *Abstract*, 7th Meeting of the German Neuroscience Society, Goettingen, Germany.

Pippow A, Husch A, Paehler M and Kloppenburg P (2006), Calcium dynamics in olfactory interneurons in situ, Program No. A074.15, *Abstract*, 5th Forum of European Neuroscience, Vienna, Austria.

Pippow A, Husch A and Kloppenburg P (2005), In Vivo Analysis of Intracellular Calcium Dynamics in Olfactory Interneurons, in Neuro-Visionen 3, Nordrhein-Westfälische Akademie der Wissenschaften, Düsseldorf, Germany, pp. 30-31.

Pippow A, Husch A, Wratil H and Kloppenburg P, (2005), Calcium Buffering in Insect Olfactory Interneurons, Program No. 139A, *Abstract*, German Neuroscience Society, Göttingen, Germany.

Husch A, **Pippow** A and Kloppenburg P, (2004), Parameters that Determine Calcium Dynamics in Insect Olfactory Interneurons, *Program and abstracts*, page 108, PO112, International Congress for Neuroethology, Nyborg, Denmark

Pippow A, Husch A and Kloppenburg P (2004), Calcium Handling in Olfactory Interneurons, in Neuro-Visionen 2, Nordrhein- Westfälische Akademie der Wissenschaften, Düsseldorf, Germany, pp. 29-30.

Husch A., **Pippow** A., Wratil H. and Kloppenburg P. (2004); Calcium Handling in Insect Olfactory Interneurons. Program No. 414.17. *Abstract*, Society for Neuroscience, Washington, DC, USA.

CURRICULUM VITAE

Dipl. Biol. Andreas Pippow
Universität zu Köln
Zoologisches Institut
Weyertal 119
50923 Köln
Tel.: 0221-470-5828
Email: andreas.pippow@uni-koeln.de

Geburtsdatum/ -ort: 14.03.1978 in Essen
Staatsangehörigkeit: deutsch

Ausbildung

2004 – 2008	**Universität zu Köln, Zoologisches Institut** Doktorarbeit im Labor von Prof. Peter Kloppenburg. Thema: "Differences of Ca^{2+} Handling Properties and Differential Processing of Olfactory Information in Identified Central Olfactory Neurons". **Stipendium der Konrad-Adenauer-Stiftung** (2005-2008)
1998 – 2004	**Universität zu Köln** Studium der Biologie, Fächer: Zoologie, Genetik, Biochemie Diplom in Biologie (Juli 2004), Note: sehr gut, Thema: "Calcium Handling in Isolated Olfactory Interneurons" Vordiplom (2000) in Biologie
2001	**Universität Florenz, Italien** Erasmus-Stipendium, Fach: Biologie
1994 – 1995	**Capity College, Wellington, New Zealand** Stipendium vom 'Youth for Understanding' Komitee
1988 – 1997	**Helmoltz-Gymnasium Essen (Abitur)**

Berufliche Tätigkeiten

2003 – 2005	**Universität zu Köln** WHK (2004-2005): Laborkurs in Zoomorphologie für Erstsemester SHK (2003-2004): Einführung in die Biologie
2002 – 2004	**Universität zu Köln, Biochemisches Institut** Molekülzeichner für die Enzymdatenbank BRENDA. Prof. Schomburg
2002 - 2003	**Universität Zürich, Pflanzenphysiologisches Institut** Forschungsassistent in den Semesterferien. Prof. Weißenböck, Köln und Dr. Klein, Zürich. Metabolisierung des Aryloxyphenoxypropanoat-Herbizids CGA 184927 in Primärblättern von Roggen.

Köln, den 22.04.2008 _____

CURRICULUM VITAE

Dipl. Biol. Andreas Pippow
Universität zu Köln
Zoologisches Institut
Weyertal 119
50923 Köln
Tel.: 0221-470-5828
Email: andreas.pippow@uni-koeln.de

Date and place of birth: 14.03.1978, Essen
Citizenship: German

Education

2004 – 2008	**University of Cologne, Institute for Zoology** PhD thesis in the Lab of Prof. Peter Kloppenburg: "Differences of Ca^{2+} Handling Properties and Differential Processing of Olfactory Information in Identified Central Olfactory Neurons". **Fellowship of the Konrad-Adenauer-Stiftung** (2005-2008)
1998 – 2004	**University of Cologne** study of biology: zoology, genetics, biochemistry Diploma in Biology (July 2004), grade: "sehr gut", topic: "Calcium Handling in Isolated Olfactory Interneurons" Vordiplom (2000) in Biology (equivalent to Bachelor)
2001	**University of Florence, Italy** Erasmus-fellowship, subject: Biology
1994 – 1995	**Capity College, Wellington, New Zealand** 'Youth for Understanding'-fellow
1988 – 1997	**Helmoltz-Gymnasium Essen (Abitur; university entrance diploma)**

Professional Qualifications

2003 – 2005	**University of Cologne** (2004-2005) Teaching assistant: laboratory course in zoomorphology (2003-2004) Teaching assistant:introductory biology
2002 – 2004	**University of Cologne, Institute for Biochemistry** Computer modeling for the enzyme database BRENDA. Prof. Schomburg
2002 - 2003	**University of Zürich, Institute for Plant Physiology** Research assistant during the semester breaks. Prof. Weißenböck, Köln und Dr. Klein, Zürich. Metabolizing of the Aryloxyphenoxypropanoat-Herbicide CGA 184927 in rye primary leafs.

Cologne, 22.04.2008 _____